ALMA Survey of Orion Planck Galactic Cold Clumps (ALMASOP): molecular jets and episodic accretion in protostars

Dutta, Somnath; Lee, Chin-Fei; Johnstone, Doug; Lee, Jeong-Eun; Hirano, Naomi; Di Francesco, James; Moraghan, Anthony; Liu, Tie; Sahu, Dipen; Liu, Sheng-Yuan; Tatematsu, Ken'ichi; Goldsmith, Paul F.; Lee, Chang Won; Li, Shanghuo; Eden, David; Juvela, Mika; Bronfman, Leonardo; Hsu, Shih-Ying; Kim, Kee-Tae; Kwon, Woojin; Sanhueza, Patricio; Liu, Xunchuan; López-Vázquez, Jesús Alejandro; Luo, Qiuyi; Yi, Hee-Weon

Publisher's version / Version de l'éditeur:
https://doi.org/10.3847/1538-3881/ad152b
The Astronomical Journal, 167, 2, 2024-01-23

The Astronomical Journal, 167:72 (68pp), 2024 February https://doi.org/10.3847/1538-3881/ad152b

ALMA Survey of Orion Planck Galactic Cold Clumps (ALMASOP): Molecular Jets and Episodic Accretion in Protostars

Somnath Dutta[1], Chin-Fei Lee[1], Doug Johnstone[2,3], Jeong-Eun Lee[4], Naomi Hirano[1], James Di Francesco[2,3], Anthony Moraghan[1], Tie Liu[5], Dipen Sahu[6,1], Sheng-Yuan Liu[1], Ken'ichi Tatematsu[7,8], Paul F. Goldsmith[9], Chang Won Lee[10,11], Shanghuo Li[10], David Eden[12], Mika Juvela[13], Leonardo Bronfman[14], Shih-Ying Hsu[1], Kee-Tae Kim[10,11], Woojin Kwon[15,16], Patricio Sanhueza[8,17], Xunchuan Liu[18], Jesús Alejandro López-Vázquez[1], Qiuyi Luo[5], and Hee-Weon Yi[10]

[1] Academia Sinica Institute of Astronomy and Astrophysics, No. 1, Sec. 4, Roosevelt Road, Taipei 10617, Taiwan, R.O.C.; sdutta@asiaa.sinica.edu.tw
[2] National Research Council of Canada, Herzberg, Astronomy and Astrophysics Research Centre, 5071 West Saanich Road, Victoria, BC V9E 2E7, Canada
[3] Department of Physics and Astronomy, University of Victoria, Victoria, BC V8P 5C2, Canada
[4] Department of Physics and Astronomy, SNU Astronomy Research Center, Seoul National University, 1 Gwanak-ro, Gwanak-gu, Seoul 08826, Republic of Korea
[5] Shanghai Astronomical Observatory, Chinese Academy of Sciences, 80 Nandan Road, Shanghai 200030, People's Republic of China
[6] Physical Research laboratory, Navrangpura, Ahmedabad, Gujarat 380009, India
[7] Nobeyama Radio Observatory, National Astronomical Observatory of Japan, National Institutes of Natural Sciences, 462-2 Nobeyama, Minamimaki, Minamisaku, Nagano 384-1305, Japan
[8] Astronomical Science Program, Graduate Institute for Advanced Studies, SOKENDAI, 2-21-1 Osawa, Mitaka, Tokyo 181-8588, Japan
[9] Jet Propulsion Laboratory, California Institute of Technology, Pasadena, CA 91109, USA
[10] Korea Astronomy and Space Science Institute (KASI), 776 Daedeokdae-ro, Yuseong-gu, Daejeon 34055, Republic of Korea
[11] University of Science and Technology, Korea (UST), 217 Gajeong-ro, Yuseong-gu, Daejeon 34113, Republic of Korea
[12] Armagh Observatory and Planetarium, College Hill, Armagh, BT61 9DB, UK
[13] Department of Physics, P.O. Box 64, FI-00014, University of Helsinki, Finland
[14] Departamento de Astronomía, Universidad de Chile, Casilla 36-D, Santiago, Chile
[15] Department of Earth Science Education, Seoul National University, 1 Gwanak-ro, Gwanak-gu, Seoul 08826, Republic of Korea
[16] SNU Astronomy Research Center, Seoul National University, 1 Gwanak-ro, Gwanak-gu, Seoul 08826, Republic of Korea
[17] National Astronomical Observatory of Japan, National Institutes of Natural Sciences, 2-21-1 Osawa, Mitaka, Tokyo 181-8588, Japan
[18] Shanghai Astronomical Observatory, Chinese Academy of Sciences, Shanghai 200030, People's Republic of China
Received 2023 June 22; revised 2023 November 25; accepted 2023 December 11; published 2024 January 23

Abstract

Protostellar outflows and jets are almost ubiquitous characteristics during the mass accretion phase and encode the history of stellar accretion, complex organic molecule (COM) formation, and planet formation. Episodic jets are likely connected to episodic accretion through the disk. Despite the importance, studies on episodic accretion and ejection links have not been done yet in a systematic fashion using high-sensitivity and high-resolution observations. To explore episodic accretion mechanisms and the chronologies of episodic events, we investigated 39 fields containing protostars with Atacama Large Millimeter/submillimeter Array observations of CO, SiO, and 1.3 mm continuum emission. We detected SiO emission in 19 fields, where 17 sources are driving molecular jets. Jet velocities, mass-loss rates, mass accretion rates, and periods of accretion events appear to have some dependence on the driving forces of the jet (e.g., bolometric luminosity, envelope mass). Next, velocities and mass-loss rates appear to be somewhat correlated with the surrounding envelope mass, suggesting that the presence of high mass around protostars increases the ejection–accretion activity. We determine mean periods of ejection events of 20–175 yr for our sample, which could be associated with perturbation zones of ∼2−25 au extent around the protostars. In addition, mean ejection periods show an apparent anticorrelation with the envelope mass, where high accretion rates may trigger more frequent ejection events. The observed periods of outburst/ejection are much shorter than the freezeout timescale of the simplest COMs like CH_3OH, suggesting that episodic events could affect the ice–gas balance inside and around the snowline.

Unified Astronomy Thesaurus concepts: Star formation (1569); Protostars (1302); Stellar jets (1607); Stellar winds (1636); Stellar accretion (1578); Submillimeter astronomy (1647)

1. Introduction

Together, jets and outflows are very intriguing phenomena that appear during the star formation process. They encode the history of accretion onto the protostar through the disk (e.g., Arce et al. 2007; Audard et al. 2014; Frank et al. 2014; Lee 2020; Fischer et al. 2023) and the formation of complex organic molecules (COMs; e.g., Jørgensen et al. 2015; Taquet et al. 2016; Jørgensen et al. 2022). Low-density mass ejections are usually referred to as "outflows," typically exhibiting low velocities (∼1 to a few tens of kilometers per second) and wide angles, and are commonly traced by the ^{12}CO (2−1) emission line. In contrast, high-density ejections along the flow axis are referred to as "jets." Jets typically exhibit high velocities (∼30 to a few hundred kilometers per second) and narrow-angle collimation, mostly concentrated around the flow axis, and are commonly traced by high-density tracers like higher transitions of SiO (e.g., $J = 5-4$, 8−7), ^{12}CO (e.g., $J = 2-1$, 3−2), or SO (e.g., $J = 8-7$).

Protostellar jets driven by accreting protostars are often observed as episodic (see reviews by Arce et al. 2007; Audard et al. 2014;

Frank et al. 2014; Fischer et al. 2023). Since mass ejection originates from the disk surface and/or inner envelope during accretion, any changes in the accretion will arguably lead to corresponding variability in the ejection phenomena. Indeed, dense knots or extended bow shocks in the observed jets are often discrete and clumpy, likely due to a discontinuous accretion process. In this picture, the typical duration between consecutive knots is interpreted as being due to periods between short episodes of the ejection, possibly driven by protostellar accretion with episodic bursts (Dunham et al. 2014b; Vorobyov et al. 2018; Fischer et al. 2023). Observed periods of ejection events range from one to a few hundred years (e.g., Plunkett et al. 2015; Jhan et al. 2022). A recent study of outflows by Nony et al. (2020) with Atacama Large Millimeter/submillimeter Array (ALMA) observations at 2600 au resolution in the CO (2–1) and SiO (5–4) transitions of a high-mass proto-cluster W43-MM1 found mean periods between ejection episodes of $\sim 500^{+300}_{-100}$ yr, corrected for a uniform inclination angle of 57.°6. Sometimes one object exhibits more than one episode, potentially originating from distinct perturbation distances in the disk (e.g., Lee 2020 and references therein). Investigating ejection events can therefore help probe the corresponding perturbation or accretion shock zones in the disk and the associated increase in the central luminosity. Such research is especially timely given the ongoing long-term monitoring of protostar continuum variability at both submillimeter and mid-infrared wavelengths (e.g., Lee et al. 2021; Park et al. 2021).

Episodic accretion could significantly impact the star formation process by modulating radiative feedback. In the case of a continuous accretion process, for example, radiative feedback could suppress fragmentation by maintaining a warm environment in the surrounding disk or cloud core (Offner et al. 2009; Krumholz et al. 2014; Yıldız et al. 2015). On the other hand, episodic accretion can weaken this effect by allowing this disk to sufficiently cool during the quiescent phase and engendering its fragmentation (Stamatellos et al. 2012). Thus, episodic accretion may affect the formation of binary/multiple systems, planets, and initial mass function of protostars (Stamatellos et al. 2011; Mercer & Stamatellos 2017; Riaz et al. 2018). Furthermore, variations in stellar luminosity and the corresponding changes in the surrounding temperature of the disk and envelope can affect the chemical composition and gas–ice balance (Jørgensen et al. 2015; Cieza et al. 2016; Hsieh et al. 2019; Wiebe et al. 2019; Jørgensen et al. 2022). Taquet et al. (2016) suggested that during the accretion phase higher-order COMs could be formed via gas-phase reactions around snowlines of the simpler COMs (e.g., CH_3OH). Therefore, accretion intervals may reveal the effects of radiative feedback on the COMs and the planet formation process.

After the first discovery of the protostellar outflow by Snell et al. (1980), several observational studies have been performed to characterize outflows (Cabrit & Bertout 1992; Bontemps et al. 1996; Lee et al. 2013; Dunham et al. 2014a; Yıldız et al. 2015; Kim et al. 2019). Due to the limitation of the observations, most of the previous studies were with single-dish telescopes with low resolution, large scale, and poor sensitivity. Recently, Podio et al. (2021) have investigated a sample of 30 sources (classified as 25 Class 0, 4 Class I, and 1 continuum) with IRAM-PdBI as a part of the CALYPSO survey. Their study reveals that most of the jets are possibly dust-free, launched from inside the dust sublimation radius, and that the ejection rate decreases as the source evolves and accretion fades. It is time to enlarge the statistics with higher-sensitivity and unbiased samples with similar environmental effects (e.g., all sources in a single molecular cloud).

Despite being important, studies linking episodic ejection and accretion have not been performed in a systematic fashion at high resolution and high sensitivity. There are, however, many recent studies of protostars that have the required observational criteria to begin such an investigation, e.g., the Perseus ALMA Chemistry Survey (PEACHES) searching for COMs in Perseus-embedded protostars (Yang et al. 2021) and the Early Planet Formation in Embedded Disks (eDisk; Ohashi et al. 2023). Here, for the first time, we have performed a systematic study of episodic jets in a large sample of protostars from a relatively high sensitivity and high resolution ALMA Survey of Orion PGCCs (ALMASOP; Dutta et al. 2020).

In this paper, we describe ALMA observations of a statically significant sample of protostars in the Orion molecular cloud. Their location in common puts them at a similar distance (∼400 pc) and in a similar environment, minimizing the effects of environmental differences on the observed parameters. First, we probe the morphology of the jet using the most efficient tracers of molecular jets to investigate driving mechanisms (e.g., whether the outflowing material is jet driven or wind driven), shock structure, and chemistry. Second, we seek to understand the origin of gas-phase SiO in the jet, following the increasing evidence of SiO in the jet. Third, we probe accretion mechanisms based on the distribution of ejected material, especially the episodic knots. In a subsequent investigation these same outflow data will be analyzed using channel maps and position–velocity (PV) diagrams and compared with the theoretical unified jet wind model developed by Shang et al. (2023).

We describe the sample selection in Section 2.1 and the ensuing observations in Section 2.2. Section 3 describes the results of continuum and line data analyses. In Section 4, we discuss the jet morphology and its connection to the accretion process. Section 5 summarizes the work. In the appendices, we discuss the properties of individual objects, including maps and spectra of each.

2. Sample Selection and Observations

2.1. Sample

During ALMA cycle 6, we initiated a survey-type project (ALMASOP) to investigate systematically the fragmentation of dense cores into protostars (Dutta et al. 2020). We selected 72 extremely cold, young, dense cores from the Planck Galactic Cold Cores (PGCC) catalog, including both candidate starless and protostellar core candidates, therefore unbiased to any spectral "Class" of the protostar. These PGCCs are, however, biased to sources with cold dense material around them, suggesting that they are potentially very young objects. From these observations, we detected 70 substructures within 48 detected dense cores, which include five candidate prestellar cores with centrally dense structures of roughly 2000 au scale where the core shows substructure within the dense portion (Sahu et al. 2021) and several hot corinos (Hsu et al. 2020, 2022). Furthermore, some sources were revealed to be multiple systems (Luo et al. 2022). The observations also revealed one of the oldest (G205.46-14.56S3; Dutta et al. 2022b) and one of the youngest protostars (G208.89-20.04Walma; Dutta et al. 2022a) with a bipolar molecular jet

in SiO emission. Interestingly, a few protostars were also found to exhibit monopolar SiO jets (Jhan et al. 2022).

After removing the candidate prestellar cores from the sample, we selected from Dutta et al. (2020) 66 substructures in 42 observing fields containing one or more protostars to investigate outflow and jet characteristics. We identified 42 outflows detected in CO emission. The rest were likely not detected owing to insufficient sensitivity, or their outflows could not be separated from the ambient cloud emission. Out of 42 outflows, SiO emission was detected in 22. Such SiO emission could trace various shocked regions, e.g., knots or bow shocks, collision zones of adjacent outflows, or collision zones of outflows on surrounding molecular clouds. We investigate 39 outflows with CO emission in this paper, of which 19 fields are also associated with SiO emission. The results for the remaining three ALMASOP protostellar objects are adopted from previously published literature, i.e., Dutta et al. (2022b; G205.46-14.56S3 and G206.93-16.61W2) and Dutta et al. (2022a; G208.89-20.04Walma). The 39 outflow objects presented in this paper have bolometric luminosities $L_{\rm bol} \sim$ 0.4–180 $L_{\odot}$ and bolometric temperatures of $T_{\rm bol} \sim$ 15–180 K, though some have undetermined $L_{\rm bol}$ and $T_{\rm bol}$ owing to a lack of infrared data. Based on the object selection criteria, this sample is one of the youngest and coldest unbiased protostellar samples within the Orion molecular cloud, all located at a similar distance. These features make this sample one of the most suitable samples for investigating variations of the outflow/jet morphology in a consistent manner.

2.2. Observations

In this paper we make use of the ALMASOP data observed in Band 6. Details of the observations and data reduction were presented by Dutta et al. (2020). In brief, we generated 1.3 mm continuum images using low-resolution ACA observations of typical beam size $7\farcs6 \times 4\farcs1$ to probe large-scale envelope emission. The data cubes of CO (2−1), SiO (5−4), and $C^{18}O$ (2−1) line emission are generated using high-resolution observations of typical beam size $\sim 0\farcs38 \times 0\farcs35$ to explore the jet/outflow structures. Here we combined data from three configurations (TM1, TM2, and ACA) to improve the sensitivity of the line cubes. The final maps have a primary beam (PB) size of $\sim 40''$, smaller than the ACA PB size of $\sim 60''$. Some of the outflows/jets extend beyond the TM1 PB area, whereas the ACA data are more suitable for sampling more extended outflow/jet emission. We present, however, the high-sensitivity, combined TM1+TM2+ACA cubes to characterize outflow cavity walls and shock/knot structure within the jet more precisely. We also compare our results with those from ACA-only observations. The observed resolution is $\sim$1.4 km s^{-1}. To achieve good signal-to-noise ratios, we binned these data to $\sim$2 km s^{-1}. We also compared these data with the data cubes of $\sim$1.4 km s^{-1}. There are many sources with faint SiO knots and $C^{18}O$ (2−1) emission within individual channels, which stand out better at 2 km s^{-1} owing to the improved sensitivity. While for bright SiO and $C^{18}O$ (2−1) emission we could utilize the $\sim$1.4 km s^{-1} velocity resolution, we binned to the same velocity resolution of $\sim$2 km s^{-1} to be consistent for all the sources.

3. Results

We utilized 1.3 mm continuum and $C^{18}O$ to investigate the dense core properties and SiO (5–4) and CO (2–1) to investigate the jets and outflows. While CO (2–1) traces both the low-density outflow shell and high-density axial knots, SiO (5–4) more efficiently traces the shocked gas, especially the high-density knots along the jet axis. The $C^{18}O$ lines can more efficiently trace the dense cores. For context, the critical density for CO ($J = 2-1$) is $n_{\rm cr,CO} \sim$ (1.0–1.2) $\times$ 10^4 cm^{-3} for temperature $T = 150$ K (assuming temperature of jet gas; e.g., Dutta et al. 2022b) to 50 K (assuming temperature of outflow gas; e.g., Yıldız et al. 2015; Dutta et al. 2022b; see Table 1). The critical density of SiO ($J = 5-4$) at a temperature of 150 K in the jet is $n_{\rm cr,\ SiO} \sim 1.7 \times 10^6$ cm^{-3}, 100 times higher than for CO. For completeness, the critical density of $C^{18}O$ (2−1) is $n_{\rm cr,C^{18}O} \sim 1.9\times10^4$ cm^{-3} for $T = 20$ K (assuming envelope temperature; e.g., Lee et al. 2006; Dutta et al. 2022a).

Table 1
Line Properties Targeted in This Study

Transition	Frequency[a] (GHz)	$E_{\rm up}$[a] (K)	$\log_{10}(A_{ij})$[a] (s^{-1})	Temp[b] (K)	$n_{\rm cr}$ (cm^{-3})
SiO (5−4)	217.104919	31.26	−3.28	150	1.7E+6
CO (2−1)	230.538000	16.60	−6.16	150	1.1E+4
CO (2−1)	230.538000	16.60	−6.16	50	1.2E+4
$C^{18}O$ (2−1)	219.560354	15.81	−6.22	20	1.9E+4

Notes.
[a] Molecular transition parameters are adopted from CDMS database (Müller et al. 2001).
[b] The critical densities are calculated for these temperatures using the collisional rate coefficients from Balança et al. (2018; SiO) and Yang et al. (2010; CO, $C^{18}O$). In the case of CO, a change in temperature from 50 to 150 K reduces $n_{\rm cr}$ by only ∼8.5%.

3.1. 1.3 mm Continuum

The low-resolution ACA 1.3 mm continuum image of the source G203.21-11.20W2 is shown in Figure 1. The remaining images are presented in Appendices B (objects with confirmed molecular jet), C (objects with complex SiO emission morphology and not considered for jet parameter estimation in this text), D (objects with no SiO emission but well-defined CO outflow), and E (objects with no SiO emission and no well-defined CO outflow). To determine the properties of the continuum sources, we fit the emission above the 3σ contour using the CASA *imfit* task with one or more 2D Gaussians for one or more, respectively, visually identified peaks. Integrated fluxes were obtained from the "flux" component in the output file of the *imfit* task. All deconvolved Gaussian parameters for each source are listed in Table 2.

For an extremely young protostar, the 1.3 mm emission could be optically thick, especially in the central core region. Hence, this emission may represent a lower limit to the total dust column density from the inner envelope around the protostars. For simplicity, however, we assume that the emission is optically thin to infer the lower limit of inner envelope mass ($M_{\rm Env}$) following the equation

$$M_{\rm Env} \sim \frac{D^2 F_\nu(\nu)}{B_\nu(T_{\rm dust})\kappa_\nu}. \quad (1)$$

The assumed dust mass opacity is $\kappa_\nu \sim 0.00899(\nu/231\ {\rm GHz})^\beta$ cm^2 g^{-1}, with a gas-to-dust mass ratio of 100 (Ossenkopf & Henning 1994; Lee et al. 2018). We also assume a dust opacity spectral index $\beta \sim 1.5$ (Lee et al. 2018). It is worth noting that

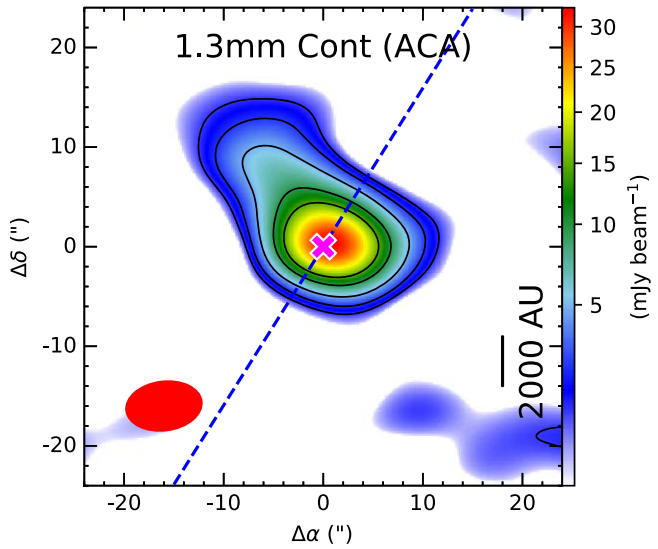

Figure 1. Example image of ALMA 1.3 mm continuum emission detected toward protostar G203.21-11.20W2. The typical beam size of $\sim 7\overset{''}{.}52 \times 5\overset{''}{.}52$ ($80\overset{\circ}{.}7$) is shown in red in the lower left corner. The contours are at $3 \times (1, 2, 4, 8, 12)\sigma$, where the sensitivity $\sigma = 0.4$ mJy beam^{-1}. The cross indicates the continuum center at high resolution, adopted from Dutta et al. (2020). The blue dashed line indicates the outflow/jet axis, determined from the SiO emission. A scale bar is also shown for context.

β could be higher than this value at early protostellar stages, due to smaller dust grains, and could be <1.0 for more evolved Class 0 or Class I objects where dust grains have grown (e.g., Draine 2006). Following Dutta et al. (2020), we adopt slightly different distances D for the sources in Orion A ($\sim 389 \pm 3$ pc), Orion B (404 ± 5 pc), and λ Ori (404 ± 4 pc). $F_\nu(\nu)$ is the measured flux density. $B_\nu(T_{\rm dust})$ represents the Planck blackbody function at a dust temperature of $T_{\rm dust}$.

We assume an optimal $T_{\rm dust} \sim 15$ K for all the inner envelopes, as estimated by Dutta et al. (2022a) from the spectral energy distribution of multiwavelength observations for one ALMASOP source. The resulting masses are also listed in Table 2. Errors are estimated based only on uncertainties in the flux. The value of $T_{\rm dust}$ could vary from as small as 10 K in the younger protostars to 30 K in the evolved protostars. For an increase of +15 K in temperature, the derived mass will decrease by 60%, and a decrease of −5 K will increase the derived mass by 85%. The histogram of all derived masses is shown in Figure 2, including Class 0, Class I, and some unclassified cores detected with ACA emission. The masses peak at $\sim 0.1\ M_\odot$, where most protostars in this sample have 1.3 mm masses <1.2 $M_\odot$. The mean masses of Class 0 and Class I sources are 1.4 and 0.65 $M_\odot$, respectively. The masses >1 $M_\odot$ are mostly associated with multiple systems (see the appendices for comments on the individual objects).

3.2. Systemic Velocity from $C^{18}O$

The systemic velocities ($V_{\rm sys}$) of the sources were estimated from the $C^{18}O$ emission observed at the continuum peak in high-resolution maps, where $C^{18}O$ is most likely tracing the disk/envelope emission around the protostars. It could, however, also trace envelope material entrained by outflow along the boundary wall. The left panel of Figure 3 shows an example of such a $C^{18}O$ map at high resolution, and the extracted spectra around the central protostar are shown in the right panel. The $C^{18}O$ spectra of other objects are shown in panel (b) of the figures in Appendices B, C, D, and E. In most cases, $C^{18}O$ spread only over two to three channels (one channel corresponding to velocity resolution ~ 2.0 km s^{-1}), making it challenging to get a reasonable Gaussian fit. Therefore, we chose the velocity of the peak emission as the $V_{\rm sys}$ (Figure 3), or we average the velocities of the brightest and second-brightest velocity channels from the spectra in cases where the peak emission spanned over more than one channel (as in case G208.89-20.04E in Figure B7). All these determined $V_{\rm sys}$ values were checked by eye against the spectra. The respective $V_{\rm sys}$ values are listed in Table 2.

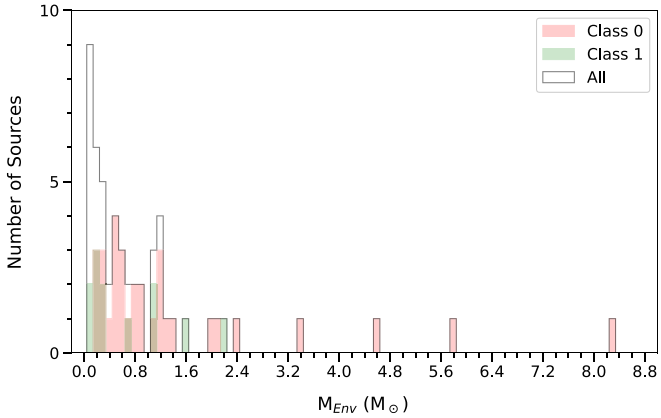

Figure 2. Histogram of envelope masses estimated using 1.3 mm emission at a resolution of $\sim 7\overset{''}{.}6 \times 4\overset{''}{.}1$.

3.3. Physical Structure of Outflow

To assess outflow morphologies, we analyzed the CO (2−1) emission. We first investigated each velocity channel and spectra along the putative flow axis to identify bipolar emission. We found three kinds of such emission, likely due to outflow inclination angle: (i) the blueshifted and redshifted emissions are well separated on the sky on both sides of the systemic velocity, (ii) there are instances where blueshifted emission and redshifted emission partially overlap, and (iii) blueshifted emission and redshifted emission almost entirely overlap. To explore such different kinds of outflow features, we estimated inclination angles i_a using the low-velocity CO emission above 3σ.

Figure 4(a) presents the integrated CO (2−1) line emission map of the source G203.21-11.20W2. A schematic diagram describing the possible structure of the outflow is shown in Appendix A (Figure A1(a)). The outermost shell of the outflow is observed to have a parabolic structure. We assume that the molecular CO outflow shell is a radially expanding parabolic shell of the underlying wide-angle wind and then accordingly fit a parabolic shape to the moment 0 map of CO emission using Equation (14) to obtain the curvature (c) at the launching point. Using the same c values, we fit another parabola in the PV diagram. Since CO emission may trace the outflow shell along with jet and ambient cloud emission, the fitting depends on the correct assumption of the outflow shell from other components. The likely ambient material near the systemic velocity is distinguished after visually inspecting individual velocity channels in the data cube. Similarly, high-density axial emission and high-velocity emission are considered as likely jet emission. If the objects exhibit high-velocity jets blended with

Table 2
Details of Targeted Dense Cores in the Orion Complex

Object	HOPS ID	R.A. (h:m:s)	Decl. (d:m:s)	Maj (arcsec)	Min (arcsec)	PA (deg)	Peak (mJy beam^{-1})	Flux (mJy)	Mass ($M_\odot$)	V_{sys} (km s^{-1})
(1)	(2)	(3)	(4)	(5)	(6)	(7)	(8)	(9)	(10)	(11)
					λ Orionis					
G191.90-11.21S	⋯	05:31:31.58	+12:56:14.35	5.04 ± 1.7	2.71 ± 1.51	36.9 ± 37.3	66.64 ± 4.83	92.58 ± 10.56	0.51 ± 0.1	7 ± 2
G192.12-11.10	⋯	05:32:19.38	+12:49:40.98	4.17 ± 0.4	2.9 ± 0.33	94.7 ± 15.0	168.12 ± 2.87	217.77 ± 5.99	1.21 ± 0.18	10 ± 2
G192.32-11.88N	⋯	05:29:54.14	+12:16:53.08	1.71 ± 0.28	1.42 ± 0.23	81.3 ± 60.8	202.97 ± 1.38	215.08 ± 2.52	1.2 ± 0.18	12 ± 2
G192.32-11.88S	⋯	05:29:54.41	+12:16:30.37	9.07 ± 0.41	4.98 ± 0.29	58.7 ± 3.6	26.38 ± 0.58	56.5 ± 1.74	0.31 ± 0.05	12 ± 2
G192.32-11.88S_02	⋯	05:29:54.14	+12:16:53.52	1.67 ± 0.4	1.27 ± 0.44	96.5 ± 83.4	197.46 ± 1.58	207.76 ± 2.88	1.15 ± 0.17	12 ± 2
G196.92-10.37_A	⋯	05:44:29.30	+09:08:51.48	7.32 ± 0.93	4.57 ± 0.89	131.6 ± 15.7	68.18 ± 3.15	128.49 ± 8.6	0.71 ± 0.12	11 ± 2
G196.92-10.37_BC	⋯	05:44:29.98	+09:08:56.36	5.55 ± 1.24	2.59 ± 1.74	0.6 ± 42.8	18.93 ± 1.33	29.17 ± 3.11	0.16 ± 0.03	11 ± 2
G200.34-10.97N	⋯	05:49:03.34	+05:57:57.72	5.97 ± 0.49	4.26 ± 0.32	87.0 ± 12.1	55.11 ± 1.38	91.87 ± 3.45	0.51 ± 0.08	14 ± 2
					Orion B					
G201.52-11.08	⋯	05:50:59.15	+04:53:49.66	2.23 ± 0.21	0.82 ± 0.34	118.2 ± 7.3	23.79 ± 0.12	25.25 ± 0.23	0.14 ± 0.02	9 ± 2
G203.21-11.20W1	⋯	05:53:42.65	+03:22:35.04	9.46 ± 1.85	5.52 ± 1.12	88.0 ± 20.8	40.62 ± 3.92	97.38 ± 12.86	0.54 ± 0.11	10 ± 2
G203.21-11.20W2	⋯	05:53:39.48	+03:22:24.59	7.77 ± 1.31	3.16 ± 2.09	42.0 ± 14.6	30.06 ± 2.19	57.94 ± 6.07	0.32 ± 0.06	10 ± 2
G205.46-14.56M1_A	317	…	…	…	…	…	…	…	…	…
G205.46-14.56M1_B	⋯	05:46:08.39	−00:10:43.32	2.5 ± 0.56	1.3 ± 0.57	62.6 ± 26.7	940.15 ± 14.27	1039.1 ± 27.44	5.77 ± 0.88	10 ± 2
G205.46-14.56M2_ABCD	387,386	05:46:08.12	−00:10:00.61	12.55 ± 1.8	2.56 ± 0.65	101.7 ± 2.4	91.07 ± 6.26	186.45 ± 19.1	1.04 ± 0.19	10 ± 2
G205.46-14.56N1	402	05:46:10.04	−00:12:16.79	2.04 ± 0.28	1.09 ± 0.67	170.6 ± 24.5	189.98 ± 1.87	207.13 ± 3.56	1.15 ± 0.17	10 ± 2
G205.46-14.56N2	401	05:46:07.72	−00:12:21.14	2.33 ± 0.34	2.27 ± 0.46	5.9 ± 81.6	132.48 ± 1.25	152.62 ± 2.46	0.85 ± 0.13	10 ± 2
G205.46-14.56S1_A	358	05:46:07.24	−00:13:30.95	4.41 ± 0.62	2.72 ± 1.87	36.2 ± 25.1	112.92 ± 3.59	158.63 ± 7.95	0.88 ± 0.14	11 ± 2
G205.46-14.56S1_B	⋯	05:46:07.33	−00:13:43.47	2.35 ± 0.35	0.98 ± 0.86	165.6 ± 20.8	210.13 ± 2.67	232.9 ± 5.12	1.29 ± 0.2	11 ± 2
G205.46-14.56S2	⋯	05:46:04.77	−00:14:16.79	4.52 ± 0.21	2.68 ± 0.09	106.1 ± 2.9	37.98 ± 0.31	49.49 ± 0.66	0.28 ± 0.04	10 ± 2
G205.46-14.56S3	315	05:46:03.63	−00:14:49.73	3.1 ± 0.46	2.53 ± 0.59	141.6 ± 37.6	102.65 ± 1.53	125.49 ± 3.12	0.7 ± 0.11	10 ± 2
G206.12-15.76	400	05:42:45.27	−01:16:13.72	0.0 ± 0.0	0.0 ± 0.0	0.0 ± 0.0	480.34 ± 7.9	438.55 ± 13.69	2.44 ± 0.37	8 ± 2
G206.93-16.61E2_ABCD	298	05:41:37.14	−02:17:17.16	4.71 ± 0.51	2.52 ± 0.77	61.1 ± 10.8	281.57 ± 5.97	386.93 ± 13.14	2.15 ± 0.33	12 ± 4
G206.93-16.61W2	399	05:41:24.93	−02:18:06.78	4.1 ± 0.46	2.51 ± 0.77	145.7 ± 14.7	621.15 ± 11.68	820.16 ± 24.97	4.56 ± 0.7	9 ± 2
					Orion A					
G207.36-19.82N1_AB	⋯	05:30:51.25	−04:10:35.46	4.31 ± 0.51	2.14 ± 0.41	82.5 ± 9.7	55.13 ± 0.94	69.06 ± 1.97	0.38 ± 0.06	11 ± 2
G208.68-19.20N1	87	05:35:23.43	−05:01:30.39	0.0 ± 0.0	0.0 ± 0.0	0.0 ± 0.0	1389.02 ± 30.21	1487.11 ± 56.35	8.26 ± 1.28	11 ± 2
G208.68-19.20N3_A	⋯	05:35:18.07	−05:00:18.44	10.06 ± 0.93	4.75 ± 0.52	119.2 ± 5.6	164.65 ± 6.98	374.3 ± 22.15	2.08 ± 0.34	12 ± 2
G208.68-19.20N3_BC	92	05:35:18.33	−05:00:34.24	4.78 ± 0.99	1.84 ± 2.02	167.2 ± 27.2	134.33 ± 7.05	191.71 ± 15.76	1.07 ± 0.18	12 ± 2
G208.68-19.20S_AB	84	05:35:26.50	−05:03:55.61	5.63 ± 1.53	3.15 ± 2.17	39.4 ± 44.0	171.99 ± 13.82	279.37 ± 33.79	1.55 ± 0.3	10 ± 2
G208.89-20.04E	⋯	05:32:48.23	−05:34:41.66	8.89 ± 2.48	3.04 ± 1.07	98.5 ± 11.3	28.76 ± 2.88	49.69 ± 7.64	0.28 ± 0.06	8 ± 2
G208.89-20.04Walma	⋯	05:32:28.25	−05:34:19.51	8.77 ± 0.77	4.45 ± 0.34	94.4 ± 4.7	34.47 ± 1.23	68.92 ± 3.55	0.38 ± 0.06	7 ± 2
G209.55-19.68N1_ABC	12	05:35:08.71	−05:55:54.50	9.58 ± 0.43	4.37 ± 0.16	97.2 ± 1.7	171.49 ± 3.38	357.13 ± 10.11	1.98 ± 0.3	6 ± 2
G209.55-19.68S1	11	05:35:13.40	−05:57:57.71	4.64 ± 0.65	3.11 ± 0.57	126.1 ± 18.0	140.2 ± 3.4	196.98 ± 7.63	1.09 ± 0.17	8 ± 2
G209.55-19.68S2	10	05:35:08.96	−05:58:28.37	8.06 ± 1.85	5.61 ± 2.07	140.1 ± 39.1	49.36 ± 4.04	110.21 ± 12.5	0.61 ± 0.12	8 ± 2
G210.37-19.53S	164	05:37:00.44	−06:37:10.92	3.14 ± 0.24	1.89 ± 1.21	19.1 ± 20.8	78.45 ± 1.27	97.1 ± 2.61	0.54 ± 0.08	6 ± 2
G210.49-19.79W	168	05:36:18.91	−06:45:24.47	8.86 ± 2.82	3.41 ± 2.94	46.9 ± 27.4	117.21 ± 16.54	252.45 ± 49.88	1.4 ± 0.35	12 ± 2
G210.82-19.47S	⋯	05:38:03.48	−06:58:16.61	6.02 ± 1.11	4.15 ± 0.56	102.8 ± 32.6	7.44 ± 0.38	12.32 ± 0.95	0.07 ± 0.01	6 ± 2
G210.82-19.47S_02	⋯	05:38:03.67	−06:58:23.80	10.02 ± 1.37	6.86 ± 1.22	66.5 ± 20.1	8.15 ± 0.52	23.54 ± 1.97	0.13 ± 0.02	6 ± 2
G210.97-19.33S2_AB	⋯	05:38:45.40	−07:01:02.38	11.75 ± 1.46	2.71 ± 0.88	80.8 ± 4.0	15.45 ± 0.93	32.8 ± 2.86	0.18 ± 0.03	3 ± 2
G210.97-19.33S2_02	⋯	05:38:46.21	−07:00:48.22	6.75 ± 1.01	2.38 ± 1.28	53.3 ± 12.1	9.74 ± 0.49	16.25 ± 1.23	0.09 ± 0.02	3 ± 2
G210.97-19.33S2_03	⋯	05:38:43.78	−07:01:13.24	0.0 ± 0.0	0.0 ± 0.0	0.0 ± 0.0	10.1 ± 0.46	7.58 ± 0.76	0.04 ± 0.01	3 ± 2
G211.01-19.54N	⋯	05:37:57.22	−07:06:57.50	12.73 ± 2.36	3.84 ± 1.05	115.4 ± 6.4	60.94 ± 5.71	146.58 ± 19.22	0.81 ± 0.16	6 ± 2
G211.01-19.54S	⋯	05:37:58.77	−07:07:27.71	7.85 ± 2.19	6.43 ± 3.46	36.9 ± 82.8	15.06 ± 1.63	36.91 ± 5.41	0.21 ± 0.04	7 ± 2
G211.16-19.33N2	133	05:39:05.83	−07:10:40.87	7.53 ± 1.45	4.32 ± 2.13	34.9 ± 30.8	12.72 ± 1.0	26.71 ± 2.93	0.15 ± 0.03	4 ± 2

Table 2
(Continued)

Object	HOPS ID	R.A. (h:m:s)	Decl. (d:m:s)	Maj (arcsec)	Min (arcsec)	PA (deg)	Peak (mJy beam^{-1})	Flux (mJy)	Mass ($M_{\odot}$)	V_{sys} (km s^{-1})
(1)	(2)	(3)	(4)	(5)	(6)	(7)	(8)	(9)	(10)	(11)
G211.47-19.27N_AB	290	05:39:57.29	−07:29:33.01	5.51 ± 1.38	3.61 ± 2.41	154.6 ± 35.1	53.35 ± 3.11	84.1 ± 7.53	0.47 ± 0.08	4 ± 2
G211.47-19.27N_02	⋯	05:39:56.99	−07:29:46.65	4.62 ± 0.45	2.66 ± 1.23	165.8 ± 13.8	4.76 ± 0.1	6.76 ± 0.22	0.04 ± 0.01	4 ± 2
G211.47-19.27S_01	288	05:39:56.01	−07:30:27.75	5.22 ± 0.81	2.24 ± 0.79	83.6 ± 11.8	464.69 ± 11.33	606.19 ± 24.8	3.37 ± 0.52	4 ± 2
G212.10-19.15N2_AB	263,262	05:41:23.72	−07:53:47.02	8.56 ± 1.17	4.35 ± 1.76	23.0 ± 23.7	17.77 ± 1.07	40.39 ± 3.34	0.22 ± 0.04	4 ± 2
G212.10-19.15N2_02	⋯	05:41:24.04	−07:53:35.62	0.0 ± 0.0	0.0 ± 0.0	0.0 ± 0.0	7.87 ± 0.3	18.45 ± 0.98	0.1 ± 0.02	4 ± 2
G212.10-19.15N2_03	⋯	05:41:24.80	−07:54:09.09	0.0 ± 0.0	0.0 ± 0.0	0.0 ± 0.0	19.55 ± 0.38	19.94 ± 0.72	0.11 ± 0.02	4 ± 2
G212.10-19.15S	247	05:41:26.21	−07:56:51.94	3.84 ± 0.95	2.81 ± 2.19	152.2 ± 37.5	110.81 ± 3.48	144.9 ± 7.5	0.81 ± 0.13	4 ± 2
G212.84-19.45N	224	05:41:32.04	−08:40:08.90	0.0 ± 0.0	0.0 ± 0.0	0.0 ± 0.0	159.37 ± 5.93	93.74 ± 8.1	0.52 ± 0.09	4 ± 2
G215.87-17.62M	⋯	05:53:32.53	−10:25:07.83	6.73 ± 2.37	2.58 ± 3.34	46.8 ± 38.4	31.52 ± 3.69	53.54 ± 9.35	0.3 ± 0.07	10 ± 2
G215.87-17.62N	⋯	05:53:42.33	−10:23:59.22	6.56 ± 1.65	4.66 ± 3.12	55.8 ± 38.7	8.46 ± 0.63	15.62 ± 1.69	0.09 ± 0.02	10 ± 2
G215.87-17.62N_02	⋯	05:53:41.85	−10:24:04.77	15.1 ± 1.46	8.28 ± 1.13	65.7 ± 8.7	5.16 ± 0.31	21.45 ± 1.59	0.12 ± 0.02	10 ± 2

Note.
[a] The objects with zero values in Columns (5), (6), and (7) are likely point sources and are not resolved in deconvolved 2D Gaussian fitting in the ACA beams. Further investigation is required to confirm their candidacy.

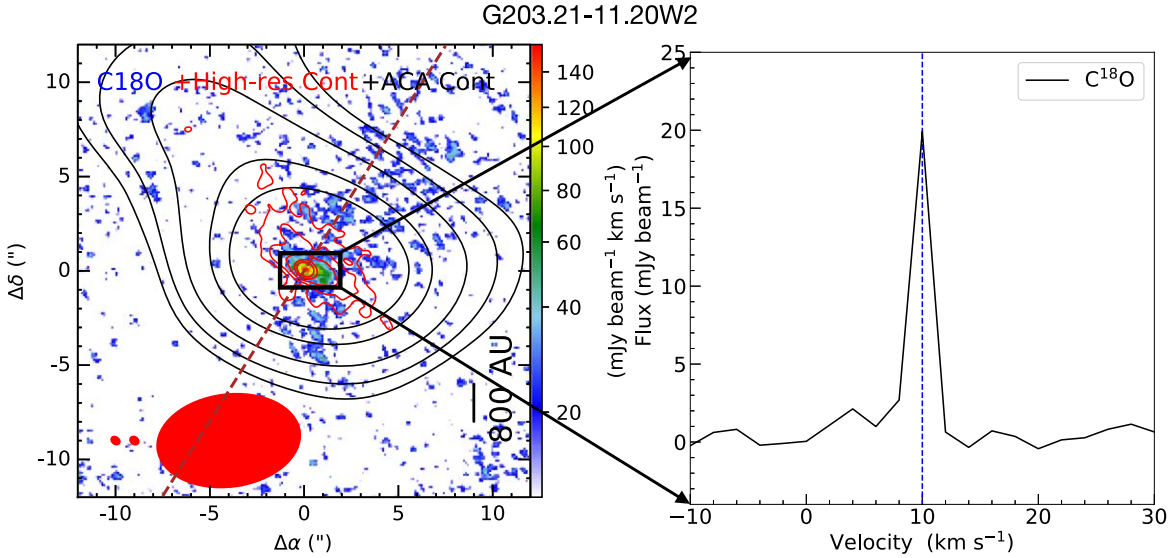

Figure 3. Left: high-resolution $C^{18}O$ map of G203.21-11.20W2 integrated over $+8-12$ km s^{-1}. The sensitivity is 15 mJy beam^{-1} km s^{-1}. The red contours are high-resolution continuum contours at (3, 6, 12, 24, 36) $\times$ σ, where the sensitivity $\sigma = 0.04$ mJy beam^{-1}, adopted from Dutta et al. (2020). The black contours are the same as in Figure 1. The beam sizes are shown in order of $C^{18}O$, high-resolution continuum, and ACA resolution continuum. The jet axis is also shown (brown dashed line). Right: the $C^{18}O$ spectrum of G203.21-11.20W2 extracted from high-resolution maps from the box region in the left panel. The vertical line indicates the systemic velocity of the object determined from the spectrum at $V_{sys} = 10$ km s^{-1}.

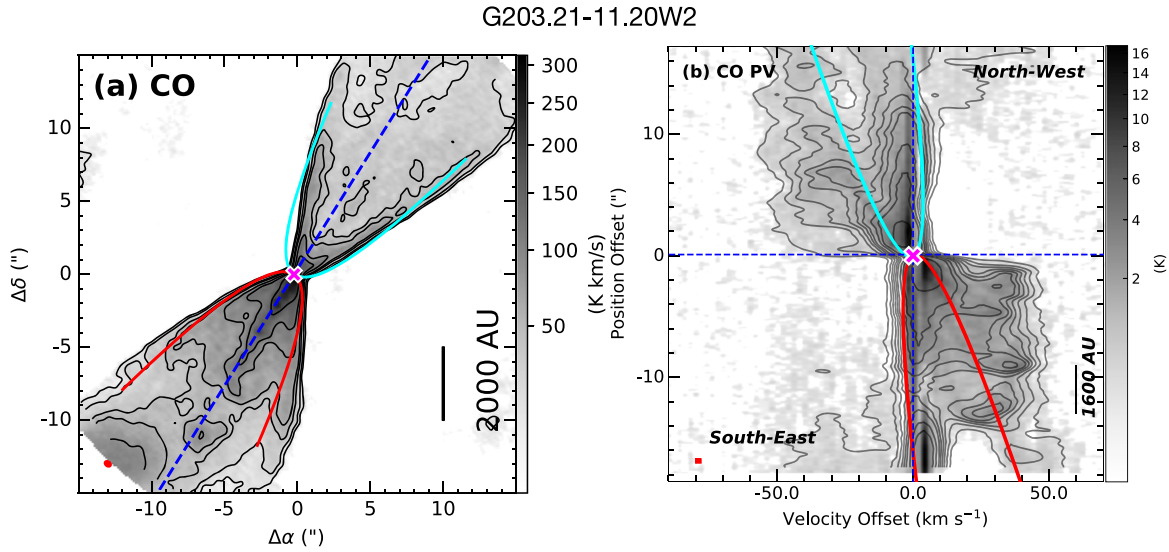

Figure 4. (a) High-resolution ALMA map of G203.21-11.20W2 in CO emission integrated from -50 to $+50$ km s^{-1}. The contours are overplotted at $3 \times$ (1, 2, 3, 4, 6, 8, 12)σ, where sensitivity $\sigma = 4.8$ K km s^{-1}. The synthesized beam size $\sim 0\farcs41 \times 0\farcs34$ is shown in the lower left corner. CO emission is extended in the northwest-to-southeast direction with a position angle of $\sim 122°$. The cyan (blueshifted) and red (redshifted) parabolas are best fits assuming a proportionality constant $c = 0.5$ arcsec^{-1}. (b) PV diagram along the jet axis of ^{12}CO (2−1) emission. The black contours are at $3 \times$ (1, 2, 3, 4, 5, 6)σ, where sensitivity $\sigma = 0.11$ K. The beam sizes are shown in the lower left (in red) emission. The red and cyan parabolas here are for inclination angle, $i = 20°$. Cyan and red represent the northwest and southeast direction, respectively, in panel (a). The magenta cross in each panel is the location of the continuum peak.

the low-velocity outflow emission, we distinguish the outflow shell by comparing the CO PV diagram with that of SiO emission (Figure 5), assuming that SiO traces mostly jet components. In Figure 4(a), fitting the parabola to the outermost contour of the outflow yields $c = 0.5$ arcsec^{-1} for both the southern and northern lobes. Using these c values, we fitted parabolas to the "outflow" emission in PV space as shown in Figure 4(b) with Equation (16) to create a complete 3D paraboloid structure, where the fitting equations include the inclination of the structure in the plane of the sky (see Appendix A for details). For example, the inclination angle for G203.21-11.20W2 is estimated to be $i \sim 20^{+5}_{-5}$ deg. In panels (c) and (d) of the figures in Appendices B, C, D, and E, we present all the fitted parabolas in integrated emission and in PV diagrams. A total of 21 outflows are fit, and the inclinations have been estimated from this model. Some of the outflows are not fit owing to indistinguishable outflow shells. The inclination angles are listed in Table 3 for all the objects. Here we note that this model is suitable only for those objects that have well-defined outflow shells, i.e., outflow walls that are well distinguished from the ambient material or outflows of multiple sources.

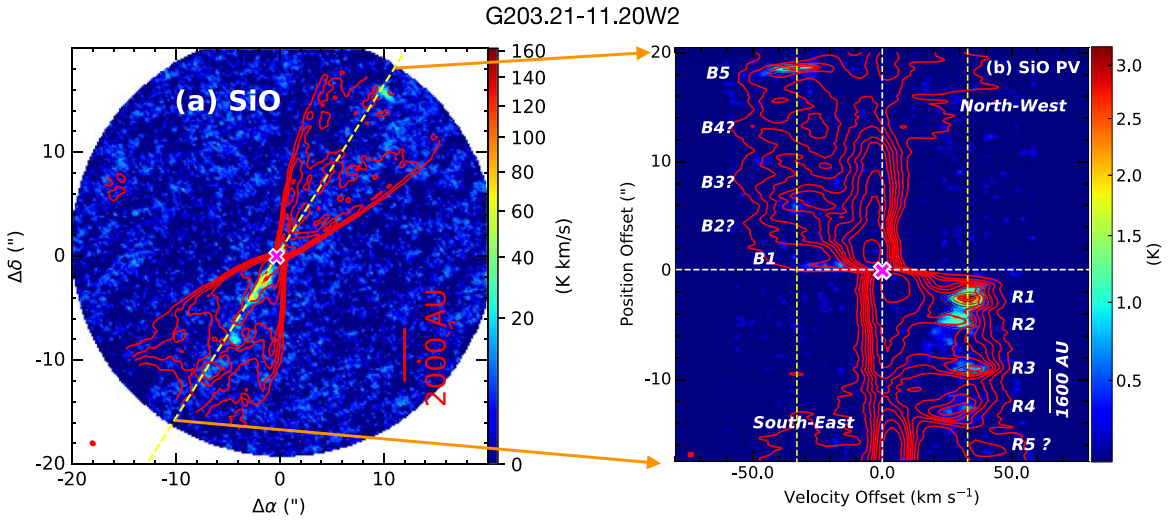

Figure 5. (a) High-resolution ALMA map of G203.21-11.20W2 in SiO emission integrated from −50 to +50 km s^{-1} with sensitivity $\sigma = 4.6$ K km s^{-1}. The CO contours are overplotted from Figure 4(a). The synthesized beam size ∼0.″41 × 0.″34 is shown in the lower left corner. The jet axis is shown with a yellow dashed line, i.e., peak of the 1.3 mm continuum adopted from Dutta et al. (2020). (b) PV diagram along the jet axis of SiO emission with sensitivity $\sigma = 0.15$ K km s^{-1}. The CO contours are the same as in Figure 4(b). The beam sizes are shown in the lower left corner (in red). The dashed lines at velocity = 33 km s^{-1} are the mean jet velocity, V_j (uncorrected for inclination). The knot location is marked in B1, B2, ... and R1, R2, ... in blue- and redshifted lobes, respectively. The "?" mark indicates that the knot positions could not be confirmed from the present observations. The magenta cross in each panel denotes the location of the continuum peak.

3.4. Outflow Force

Outflow force $F_{\rm CO}$ is the mean rate of momentum P of outflowing material, derived by estimating the outflow momentum over the dynamical time $\mathcal{T}_{\rm dyn,out}$ of the outflow, where $\mathcal{T}_{\rm dyn,out}$ is the length of the jet divided by the velocity of the outflow. Outflow force $F_{\rm CO}$ was calculated from the beam-averaged CO emission across the whole velocity range above 3σ on each lobe (blue and red) separately. To avoid contamination from ambient material, we removed a few channels near the systemic velocity after inspecting channel maps. First, outflow emission above 3σ in the whole data cube is converted into mass. For example, the kth channel has an outflow mass of M_k:

$$M_k = \mu_{\rm H_2} m_{\rm H} A \frac{\sum_l N_{{\rm CO},l}}{X_{\rm CO}}, \quad (2)$$

where the beam-averaged CO column density $N_{\rm CO}$ is summed over outflow pixels l on the kth channel and each pixel has an area of A. We assumed a CO-to-H_2 abundance ratio of $X_{\rm CO} \sim 10^{-4}$ (e.g., Hirano et al. 2010) at an excitation temperature of $T_{\rm ex} \sim 50$ K (e.g., Yıldız et al. 2015; Dutta et al. 2022b) in the lower-density extended outflow, which could be higher by a factor of a few in the high-density jets. In the next step, the estimated masses are converted into momentum $P \sim M_k V_k$, for a mass of M_k on the kth channel with the central velocity of $V_k = |V_{\rm obs} - V_{\rm sys}|$. Finally, for a total outflow extension of $R_{\rm CO}$ with maximum outflow velocity $V_{\rm CO,max}$, $F_{\rm CO}$ is expressed as

$$F_{\rm CO} = \frac{P}{\mathcal{T}_{\rm dyn,out}} = f_{ia} \frac{V_{\rm CO,max} \sum_k M_k V_k}{R_{\rm CO}}, \quad (3)$$

where the factor f_{ia} is the correction factor for the inclination of the system in the plane of the sky. The inclination-corrected $F_{\rm CO}$ values are listed in Table 3.

Here we note that we do not cover the full outflow extents within the TM1/TM2 PB (∼40″). If, however, we increase the field of view (FOV; as for ACA maps), the outflow mass and dynamical time may both increase, and so $F_{\rm CO}$ measurements are not expected to change drastically. We also compared the present $F_{\rm CO}$ values with those derived from ACA maps (FOV ∼ 60″), and we see only changes by factors of 1–1.5 from the smaller PB values. In addition, we could not recover the whole outflow emission from the ACA maps owing to their relatively poor sensitivity compared with the combined high-resolution maps. Therefore, we present only the $F_{\rm CO}$ measurements derived from the high-sensitivity combined maps.

Errors of $F_{\rm CO}$ estimation depend on the amount of missing flux in interferometric observations, the lack of coverage of the full length of the outflow lobe, calibration, the optical depth of CO, the temperature variation of the outflow, and errors in the inclination angle measurements. Since the above information could not be recovered simultaneously from the present observations, we assume a conservative error of 40% in all plots in the subsequent sections.

3.5. Molecular Jet Detection and Episodes of Accretion

To assess the high-density jets associated with protostars within the outflow cavities, we searched the CO and SiO data cubes at velocities both blue- and redshifted from the $V_{\rm sys}$. Given its higher critical density and an expected increase in SiO from dust grains shattered in shocks, the SiO emission is more suitable for detecting the high-density material and shocks in the jets, whereas the CO traces both high-density jets and low-density outflow structures. All SiO emission integrated maps are shown in Figures 6 (monopolar or likely monopolar jets), 7 (bipolar jets), and 8 (noncharacterized SiO emission). In Figures 6 and 7, SiO is clearly observed along the flow axis, where CO is seen more widely, i.e., within and surrounding the SiO emission along the flow axis, and in the CO outflow shell. In Figure 8, four sources exhibit SiO emission along one lobe, of which G211.47-19.27S_B is clearly a monopolar jet. Most of the jets are clumpy, discontinuous knot-like structures. As shown in Figure 5 for G203.21-11.20W2, in the red lobe, four knots (R1, R2, R3, and R4) are consistent in both SiO and CO emission, and another knot (R5?) is possibly detected in

Table 3
Properties of the Sources with Jet and Outflows

ALMA ID (1)	HOPS ID (2)	Class (3)	L_{bol} ($L_\odot$) (4)	T_{bol} (K) (5)	i (deg) (6)	Lobe (7)	F_{CO}[a] (10^{-8} $M_\odot$ km s^{-1} yr^{-1}) (8)	N_{SiO} (10^{-14} cm^{-3}) (9)	N_{CO}[b] (10^{-16} cm^{-3})[b] (10)	X_{SiO}/X_{CO}[b] (10^{-4})[b] (11)	V_j[b] (km s^{-1}) (12)	$V_{j,cor}$[a] (km s^{-1}) (13)	M_j[a] (10^{-7} $M_\odot$ yr^{-1}) (14)	$L_{j,kin}$[a] (10^{-2} $L_\odot$) (15)	T_{perd}[a] (yr) (16)
SiO Monopolar or Significantly Fainter Than Other Pole															
G191.90-11.21S		0	0.4 ± 0.2	69 ± 17	5^{+3}_{-4}	Blue	922.52	0.85	45.96	10.322	6 ± 3	69^{+275}_{-26}	4.88	18.99	100^{+61}_{-80}
						Red	2070.4	8.94	48.89				5.19	20.2	
G203.21-11.20W2		0	0.5 ± 0.3	15 ± 5	20^{+5}_{-5}	Blue	348.68	1.65	8.65	15.408	33 ± 5	96^{+32}_{-18}	1.29	9.83	71^{+20}_{-19}
						Red	358.98	3.01	21.59				3.21	24.56	
G205.46-14.56M1	317	0	4.8 ± 2.1	47 ± 12	75^{+5}_{-15}	Blue	90.76	7.93	14.27	73.938	88 ± 10	91^{+11}_{-2}	2.0	13.67	100^{+50}_{-53}
						Red	9.7	0.0	7.17				1.01	6.86	
G205.46-14.56S1	358	0	22.0 ± 8.0	44 ± 19	1^{+5}_{-0}	Blue	153837.41	1.42	34.35	5.873	1 ± 4	57^{+0}_{-47}	4.25	22.45	34^{+170}_{-17}
						Red	11035.28	3.41	47.91				5.92	31.31	
G209.55-19.68S2	10	0	3.4 ± 1.4	48 ± 11	20^{+10}_{-5}	Blue	50.89	0.0	0.0	46.845	50 ± 5	146^{+47}_{-46}	0.0	0.0	22^{+13}_{-6}
						Red	61.7	1.61	3.44				0.78	13.61	
G192.32-11.88N		0			9^{+5}_{-8}	Blue	184.69								
						Red	7.89								
G211.47-19.27S	288	0	180 ± 70	49 ± 21		Blue									
						Red									
SiO Bipolar															
G205.46-14.56S3	315	1	6.4 ± 2.4	178 ± 33	40^{+8}_{-8}	Blue	2150.0	3.7	9.5	30.89	80 ± 10	124^{+27}_{-16}	2.9	36.83	54^{+30}_{-20}
						Red	1100.0	2.2	9.6				3.0	38.1	
G206.12-15.76	400	0	3.0 ± 1.4	35 ± 9	15^{+15}_{-5}	Blue	57.77	2.41	9.86	14.128	40 ± 15	155^{+75}_{-75}	2.35	46.09	30^{+35}_{-10}
						Red	105.4	2.58	25.51				6.08	119.21	
G206.93-16.61W2	399	0	6.3 ± 3.0	31 ± 10	10^{+5}_{-5}	Blue	9500.0	13.0	15.0	88.38	50 ± 10	288^{+286}_{-95}	28.8	1957.97	17^{+30}_{-10}
						Red	28840.0	12.1	13.4				26.6	1808.4	
G208.68-19.20N1	87	0	36.73 ± 14.5	38 ± 13	25^{+15}_{-5}	Blue	113.0	5.81	81.95	7.398	43 ± 6	102^{+24}_{-35}	12.85	109.29	19^{+9}_{-4}
						Red	141.05	5.98	77.43				12.15	103.27	
G208.68-19.20N3		0			35^{+15}_{-15}	Blue	96.75	21.25	69.9	26.131	35 ± 15	61^{+41}_{-15}	6.58	20.11	81^{+56}_{-39}
						Red	73.51	15.28	69.9				6.58	20.11	
G208.89-20.04E		1	2.2 ± 1.0	108 ± 25	1^{+2}_{-0}	Blue	1562.03	0.92	12.0	7.572	2 ± 2	115^{+0}_{-77}	2.12	22.86	52^{+104}_{-26}
						Red	1680.27	0.73	9.73				1.72	18.55	
G208.89-20.04Walma		0	0.8 ± 0.4	31 ± 10	5^{+5}_{-4}	Blue	2.0	0.27	2.3	10.417	4 ± 2	46^{+183}_{-23}	2.02	1.9	176^{+178}_{-141}
						Red	1.2	0.18	2.02				1.9	1.8	
G209.55-19.68S1	11	0	9.1 ± 3.6	50 ± 15		Blue		3.28	11.74	19.79	27 ± 4				
						Red		4.2	26.03						
G210.37-19.53S	164	0	0.6 ± 0.3	39 ± 10	25^{+10}_{-10}	Blue	10.31	2.21	5.01	38.474	36 ± 5	85^{+54}_{-22}	0.66	3.92	23^{+18}_{-10}
						Red	5.76	1.54	4.74				0.62	3.71	
G210.49-19.79W	168	0	60.0 ± 24.0	51 ± 20	5^{+5}_{-4}	Blue	5030.76	0.72	21.31	5.255	5 ± 4	57^{+229}_{-28}	1.89	5.1	78^{+78}_{-16}
						Red	11410.83	0.8	7.56				0.67	1.81	
G215.87-17.62M		0			30^{+10}_{-10}	Blue	36.01	1.46	17.22	7.152	30 ± 10	60^{+28}_{-13}	1.59	4.71	66^{+30}_{-25}
						Red	79.06	0.92	15.94				1.47	4.36	

Table 3
(Continued)

ALMA ID (1)	HOPS ID (2)	Class (3)	L_{bol} ($L_\odot$) (4)	T_{bol} (K) (5)	i (deg) (6)	Lobe (7)	F_{CO}[a] (10^{-8} $M_\odot$ km s^{-1} yr^{-1}) (8)	N_{SiO} (10^{-14} cm^{-3}) (9)	N_{CO}[b] (10^{-16} cm^{-3})[b] (10)	X_{SiO}/X_{CO}[b] (10^{-4})[b] (11)	V_j[b] (km s^{-1}) (12)	$V_{j,cor}$[a] (km s^{-1}) (13)	M_j[a] (10^{-7} $M_\odot$ yr^{-1}) (14)	$L_{j,kin}$[a] (10^{-2} $L_\odot$) (15)	T_{perd}[a] (yr) (16)
							Complicated SiO Morphology								
G200.34-10.97N		0	1.5 ± 0.6	43 ± 10	12 $^{+10}_{-5}$	Blue	102.38								
						Red	83.76								
G205.46-14.56M2N		0				Blue									
						Red									
G205.46-14.56N2N		0				Blue									
						Red									
							No SiO Emission, Only CO Outflows								
G192.12-11.10		0	9.5 ± 4.0	44 ± 15	15 $^{+10}_{-5}$	Blue	435.86								
						Red	610.18								
G196.92-10.37		0			70 $^{+10}_{-10}$	Blue	25.52								
						Red	12.52								
G203.21-11.20W1		0			20 $^{+10}_{-5}$	Blue	22.2								
						Red	11.71								
G209.55-19.68N1	12	0	9.0 ± 3.7	47 ± 13	27 $^{+15}_{-10}$	Blue	187.43								
						Red	18.87								
G208.68-19.20S	84	1	49.0 ± 18.0	96 ± 25	10 $^{+10}_{-5}$	Blue	37.74								
						Red	2.97								
G211.01-19.54N	153	0	4.5 ± 1.8	39 ± 12	50 $^{+10}_{-20}$	Blue	2.14								
						Red	8.72								
G211.01-19.54S	152	0	0.9 ± 0.4	52 ± 8		Blue									
						Red									
G212.84-19.45N	224	0	3.0 ± 1.2	50 ± 13	25 $^{+15}_{-10}$	Blue	8.03								
						Red	14.88								

Notes.
[a] Corrected for inclination angle i.
[b] Not corrected for inclination angle i.

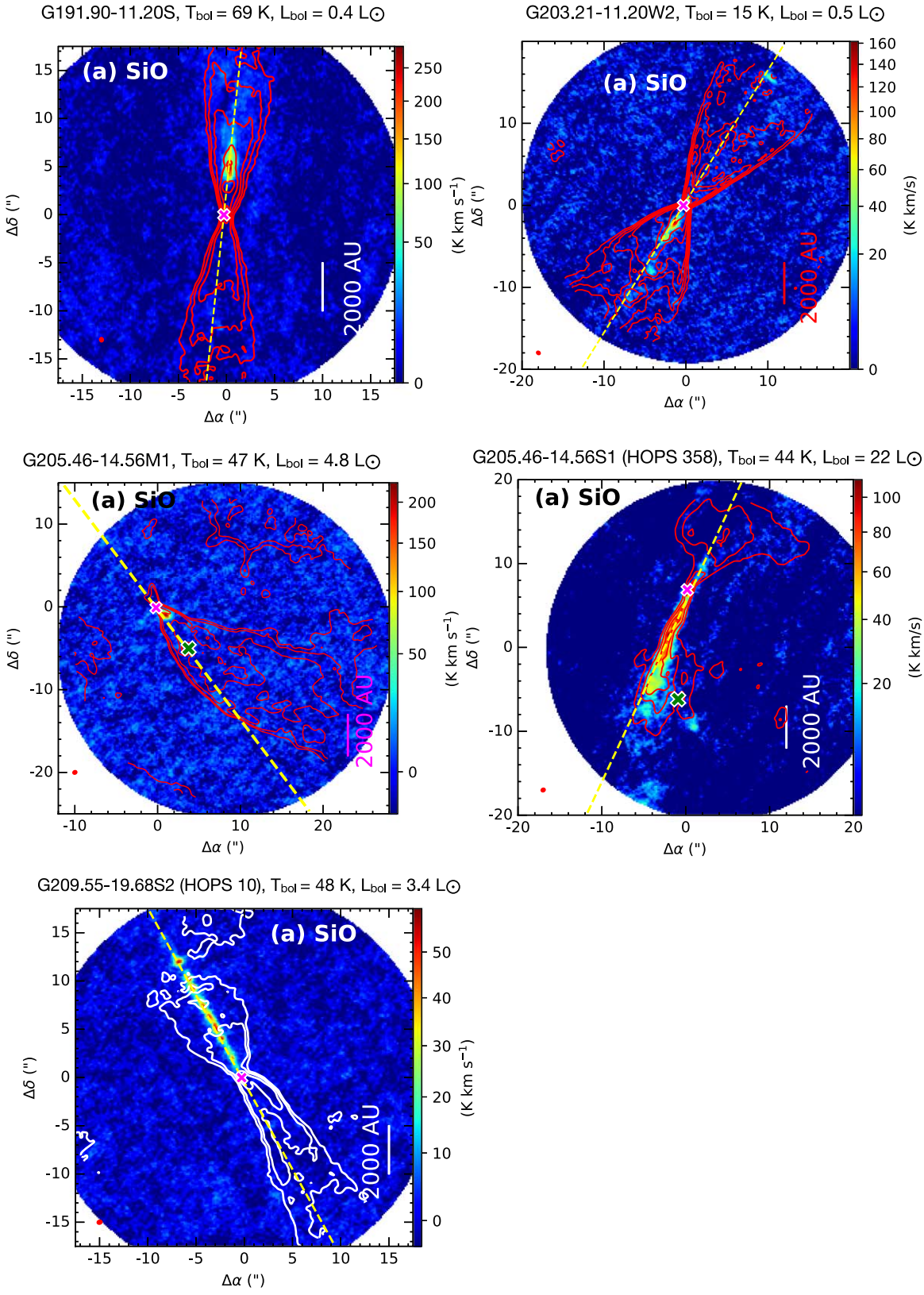

Figure 6. High-resolution integrated over whole SiO emission velocity range of monopolar or likely monopolar SiO jets of protostars. The contours and symbols are the same as in Figure 5(a). The SiO and CO velocity information and sensitivity are added in the associated figures in the appendices.

CO emission but not detected in SiO emission. In the blue lobe, two knots (B1 and B5) are detected in both SiO and CO emission, whereas the CO peaks at B2?, B3?, and B4? are not detected with SiO emission. For the other outflows, the CO and SiO integrated maps and their respective PV diagrams are presented in Appendices B (objects with confirmed molecular jet) and C (objects with complex SiO emission morphology and not considered for jet parameter estimation in this text).

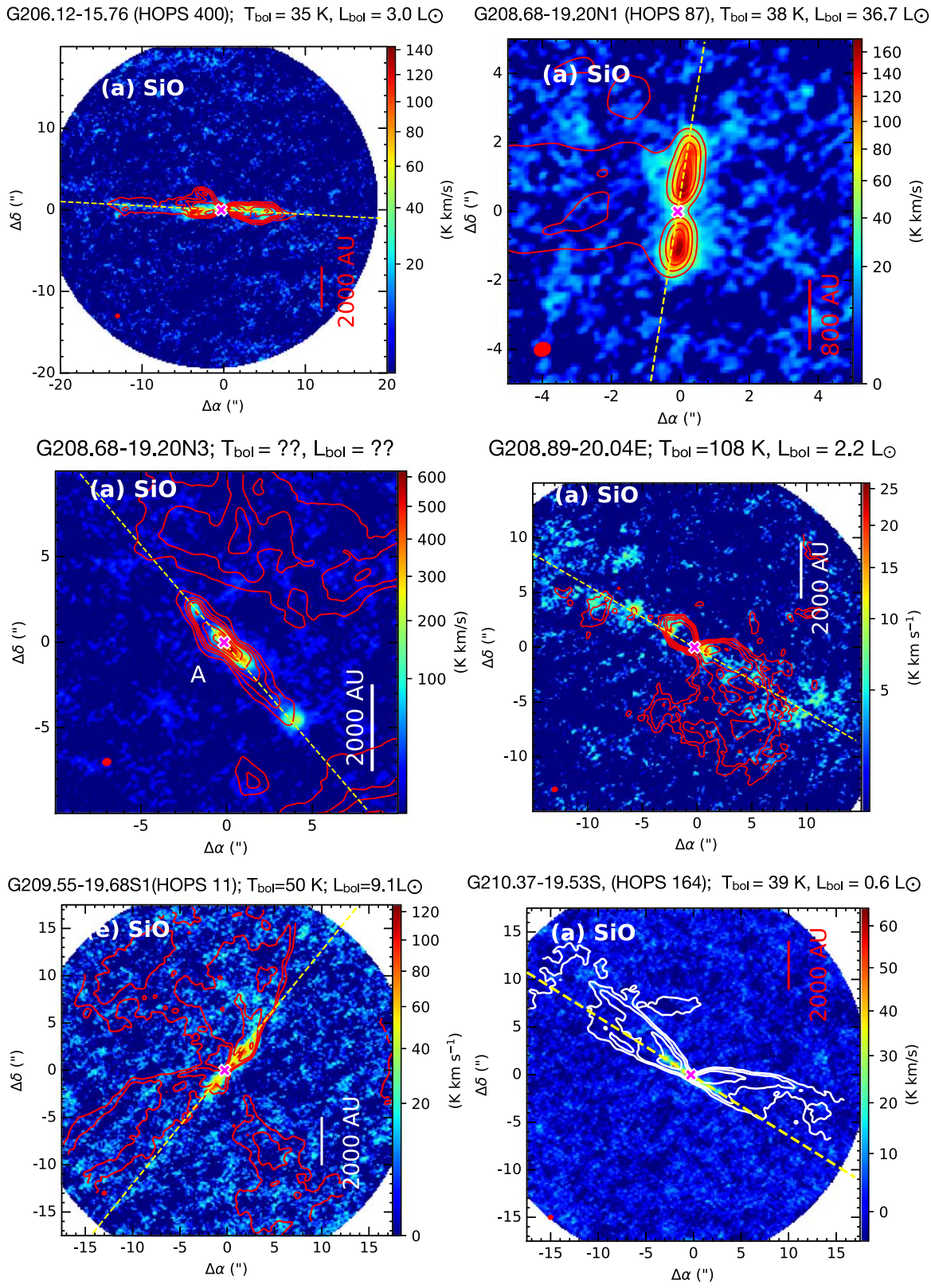

Figure 7. Bipolar jets in SiO emission. All the symbols are the same as in Figure 6. The "??" mark for T_{bol} and L_{bol} indicates that these values are yet to be determined and not available in the literature.

We observed 19 fields with SiO emission in Figures 6–8, out of which 14 have confirmed protostellar jets. Three (G200.34-10.97N, G205.46-14.56M2, and G205.46-14.56N2 in Figure 8) exhibit SiO emission along the jet axis, which could be the bow shocks of jets or collision zones between outflow and ambient material. SiO in one field within G209.55-19.68N1 is clearly a collision zone between two outflows. In the case of G205.46-14.56M2, the driving source of SiO is not clearly identified,

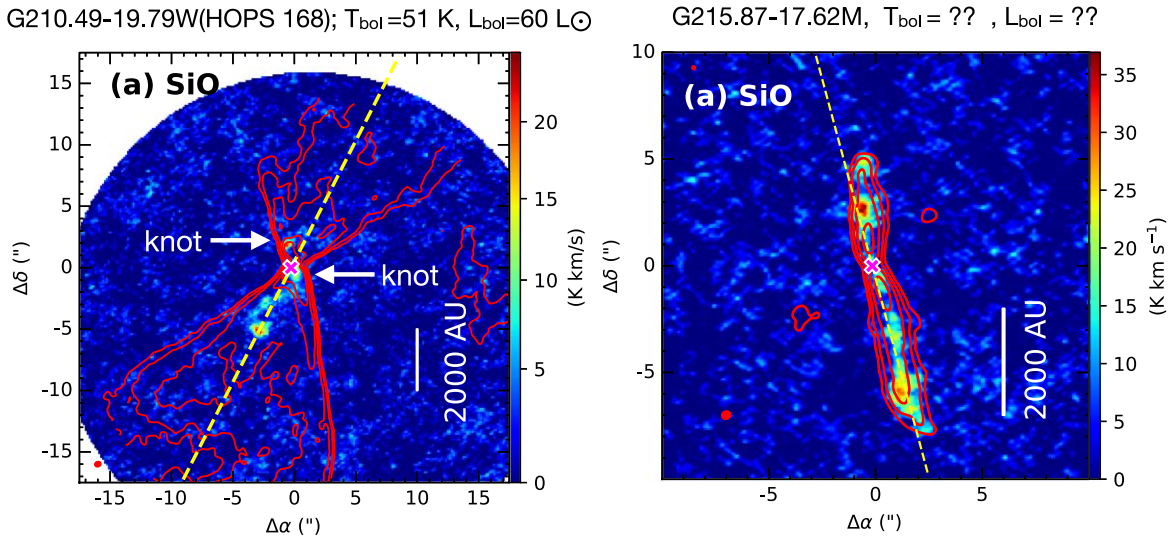

Figure 7. (Continued.)

and it could be emission from other molecules in this line-rich source (e.g., a hot corino) that mimics SiO emission. It is difficult to conclude the existence of a jet in this particular source from the present observations. All the SiO emission integrated maps and PV diagrams are shown in Figures B1–B12 and C1–C6. Six of the sources exhibit monopolar or nearly monopolar SiO jets (G203.21-11.20W2, G191.90-11.20S, G205.46-14.56M1, G205.46-14.56S1, G209.55-19.68S2, G211.47-19.27S_B). In some cases, CO traces both sides of the jet but SiO is monopolar, such as the blueshifted component of G203.21-11.20W2. In some monopolar cases, like the source G209.55-19.68S2 (Figues 6 and B.9), there is no jet emission detected in the blueshifted lobe with SiO or in the CO.

The mean of the velocity of the brightest peak knot emission is considered to be the observed jet velocity V_j, and these are listed in Table 3. While measuring jet velocities from the peak of the knot emission, we visually checked the extended knot emission and considered larger error bars to account for the visual knot extension and the uncertainty in $V_{\rm sys}$. We note that the uncertainty in $V_{\rm sys}$ is not significant compared to the extended emission of the knots. A histogram of measured mean jet velocity corrected for inclination angle, i.e., $V_{j,\rm cor}$ ($=\frac{V_j}{\sin i}$), is shown in Figure 9. Jet velocities are distributed over a large range from ∼50 to 290 km s^{-1}, where most (∼60%) are less than 100 km s^{-1}. Proper-motion studies of jet knots of the object HH 212 also reveal that the jet velocity could be as small as ∼50 km s^{-1} (Lee et al. 2022). The mean of all corrected jet velocities is estimated to be $V_{j,\rm cor_{mean}} = 112$ km s^{-1}. We note that a few of the outflows have very small inclination angles (close to edge-on), but some inclinations could not be derived accurately from present observations of outflow shells. In those cases, the jet velocities could change significantly with only a few degrees of change in inclination angle given the error bars in the measured inclination angles, as shown in Figure 9 (see also Table 3). For sources G205.46-14.56S1_A ($V_{j,\rm cor}$ = 80.22 km s^{-1}) and G208.89-20.04E ($V_{j,\rm cor}$ = 114.60 km s^{-1}) in particular, the inclination angles could be <1°, and so a significant change in velocity could be expected given improved inclination measurements.

The mean timescales between knots are measured as $\mathcal{T}_{\rm knot} = \frac{\delta R}{V_j}\tan(i)$, where δR is the mean distance between two consecutive knots. The values are listed in Table 3. The derived $\mathcal{T}_{\rm knot}$ values range from ∼20 to 175 yr for different jet knot pairs.

3.6. Jet Mass-loss Rate and Kinetic Luminosity

The jet mass-loss rates $\dot{M}_j$ were derived from the CO integrated emission. First, we disentangled the most likely jet emission from the outflow shell by considering SiO emission as being representative for the jet. Figure 5(b) shows the SiO emission of G203.21-11.20W2 in the PV diagram, where SiO emission is also found at high velocity (>15 km s^{-1}). Therefore, we consider the jet velocity range to extend from the minimum SiO velocity to the maximum available CO (or SiO) velocity. This particular object is moderately inclined ($i \sim 20°$). For a highly inclined object like G191.90-11.20S (close to edge-on; Figures 10(a)–(b) and B1), however, the SiO emission does not extend to the high velocity range, so here we consider the whole velocity range of SiO emission as jet emission, independent of higher-velocity consideration.

Next, nearest to the continuum we choose the peak emission from the knots in CO maps integrated over likely jet velocities. These knots are expected to be less distorted by flow into the ambient medium than knots that are farther away. The peak emission is converted into beam-averaged CO column density $N_{\rm CO}$ assuming a specific excitation temperature of $T_{\rm ex} \sim 150$ K within the jet (e.g., Dutta et al. 2022b). $N_{\rm CO}$ is utilized to obtain the H_2 column density N_{H_2} for a CO abundance ratio, $X_{\rm CO} = N_{\rm CO}/N_{H_2}$ (∼4×10^{-4}; Glassgold et al. 1991). Here higher values of temperature and density are assumed in the compressed shocked gas within the jet than those of an extended less dense outflow gas or wind component (Section 3.4). We consider the molecular jet to be flowing through a uniform cylinder at a constant density at constant speed along the transverse beam direction. Typical jet widths are <20 au, as measured for the HH 212 object by Lee et al. (2017a). Our observed spatial resolution is ∼140 au;

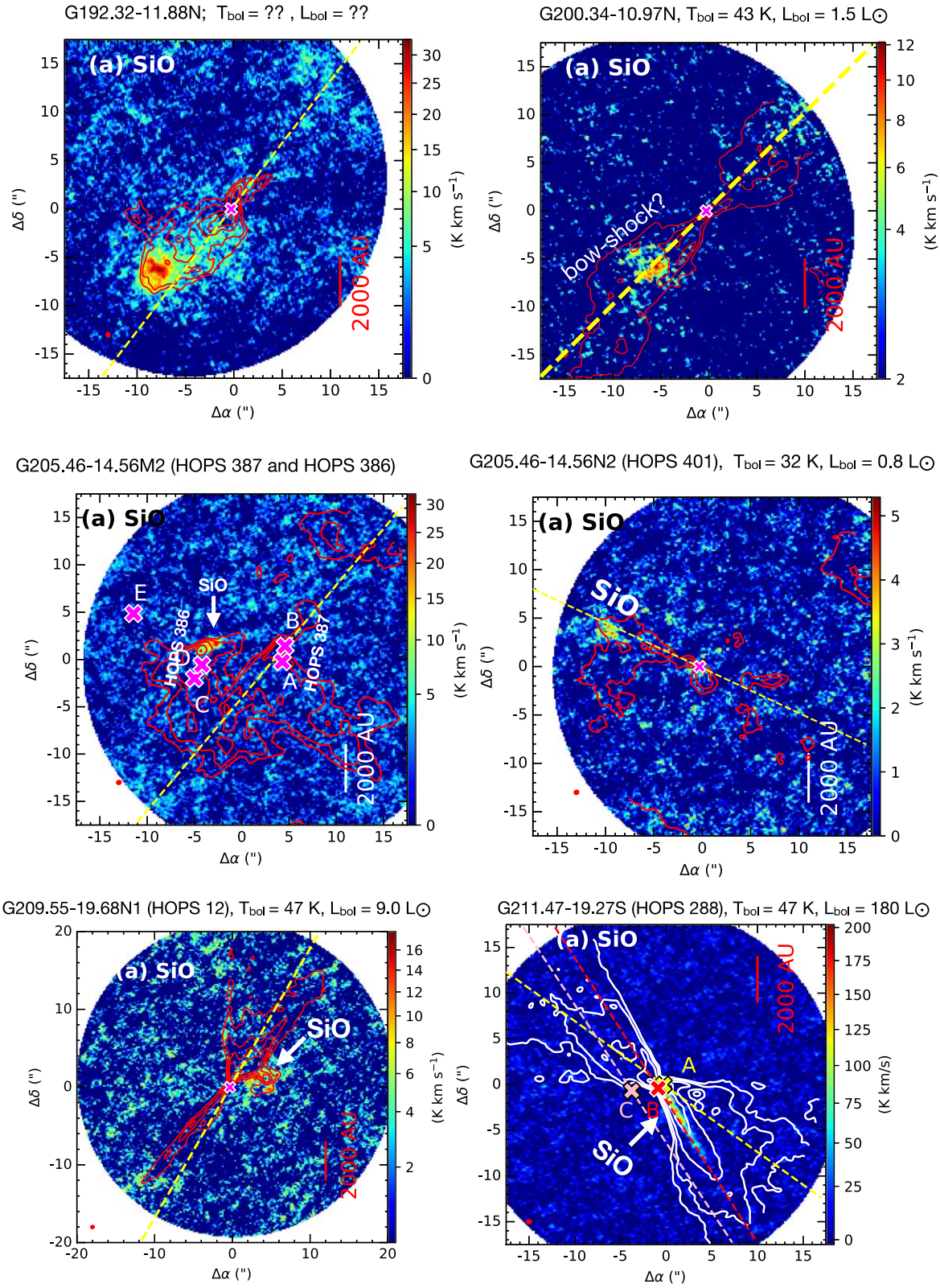

Figure 8. SiO emission along the outflow/jet axis. The SiO emission is not well characterized as jet emission in this study. All the symbols are the same as in Figure 6. Faint SiO emission locations are marked in some of the panels. The "??" mark for $T_{\rm bol}$ and $L_{\rm bol}$ indicates that these values are yet to be determined and not available in the literature. The "?" mark indicates that the structures could not be confirmed from the present observations.

therefore, our data could not spatially resolve the exact jet width even at the high spatial resolution achieved in this study. Hence, the beam size b_m is taken to be the higher limit of the jet width.

Thus, $\dot{M}_j$ can be expressed as

$$\dot{M}_j = \frac{1}{3}\mu_{\rm H_2} m_{\rm H} \frac{N_{\rm CO}}{X_{\rm CO}} V_{j,\rm cor}\, b_m, \quad (4)$$

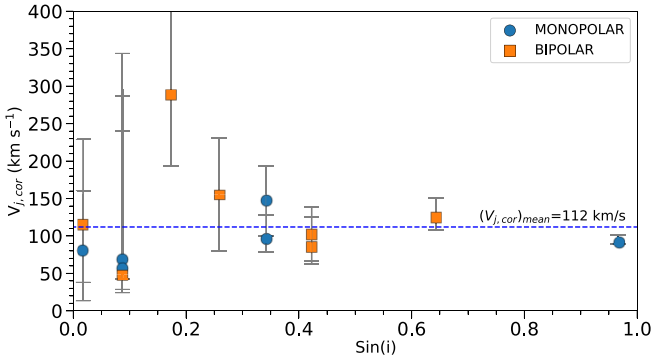

Figure 9. Inclination-corrected mean jet velocities $V_{j,\mathrm{cor}} = \frac{V_j}{\sin i}$ are shown as a function of $\sin i$, where i is the measured inclination angle. The mean value of $V_{j,\mathrm{cor}} = 112$ km s^{-1} is also shown. Monopolar and bipolar jets are shown as circles and squares, respectively.

where $\mu_{\mathrm{H_2}} = 2.8$ is the mean molecular weight and m_{H} is the mass of a hydrogen atom. $V_{j,\mathrm{cor}}$ is the mean deprojected jet velocity (i.e., $V_j/\sin(i)$). The knots observed in this spatial resolution likely delineate the internal bow shocks or gas that has been highly compressed by shocks. Since the knots are not resolved, we assume a compression factor of $1/3$ following Lee et al. (2007a, 2007b). The jet kinetic luminosity is defined as $L_{j,\mathrm{kin}} = (1/2) \times \dot{M}_j V_{j,\mathrm{cor}}^2$. The inclination-corrected $\dot{M}_j$ and $L_{j,\mathrm{kin}}$ values are listed in Table 3.

Given that CO abundances could be as small as $X_{\mathrm{CO}} \sim 10^{-4}$ instead of the present assumption (e.g., Hirano et al. 2010), the tabulated $\dot{M}_j$ and $L_{j,\mathrm{kin}}$ values could be higher. Therefore, we consider our measured values to be lower limits to the mass-loss rates. The error bars of these measurements also depend on various factors in flux measurements, as discussed above in Section 3.4. With these complications, we assumed a conservative error of 40% for the measured $\dot{M}_j$ values.

4. Discussion

4.1. Which Emission Traces Which Component?

Figure 10 shows a zoomed-in view of the jet of G191.90-11.21S for an example. The schematic diagram in Figure 10 (right panel), drawn based on the observations, describes various components of protostars traced by the 1.3 mm continuum and the C^{18}O (2–1), CO (2–1), and SiO (5–4) lines. Different structures of one knot (middle panel) are elaborated in the schematic diagram (right panel), where the corresponding PV diagram is shown in the left panel. The large extended knot (∼1600 au) is most likely a single knot in the formation stage, where the inner layer (CO peak) is still pushing the material outward (i.e., toward the SiO layer or beyond it), and it is possibly formed recently and still at the initial stage of shock formation yet to form one more compact shock structure. The continuum maps at 140 and 2200 au resolution delineate the thermal dust emission from the disk and inner envelope and the inner-to-moderate-scale envelope emission, respectively (Figures 1 and 3, left panel). At 140 au resolution, C^{18}O emission likely traces the disk and inner envelope. In a few cases, we may have resolved the larger disks, but the velocity resolution of our observations is not sufficient to probe their kinematics and geometry.

As shown in Table 1, the SiO emission has a higher critical density ($n_{\mathrm{cr}} \sim 1.66 \times 10^6$ cm^{-3}) than that of CO ($n_{\mathrm{cr}} \sim 1.06 \times 10^4$ cm^{-3}). The optical depth can be derived as $\tau = -\ln(F/F_0)$, where F is the observed flux density and F_0 is the flux density for blackbody radiation at temperature T_{ex} at a particular frequency. We estimated optical depths for SiO (τ_{SiO}) and CO (τ_{CO}) emission from the peak emission within the knots, assuming a temperature $T_{\mathrm{ex}} \sim 150$ K within the jet (see Section 3.6), and find that the SiO emission is optically thicker than that of CO ($\tau_{\mathrm{SiO}} > \tau_{\mathrm{CO}}$) within the knots. Hence, CO emission arises from deeper layers within the knots than does the SiO emission. In the ALMASOP sample, we observe that CO emission is tracing the low-density outflow shell. The shock regions or knots of higher density along the jet axis are detected in both SiO and CO emission, and we expect the latter to trace more interior parts of the knots owing to its lower optical depths. We also see CO emission forward and in front of the SiO+CO emission boundary in some knots, which could consist of relatively lower density and cooler material than the SiO+CO shock regions. Another layer of CO emission in the back was also seen in a few knots, which could be the slower-moving material of the shock (see G191.90-11.20S in Figure 10, as well as Figures B1(d) and (f) in Appendix B). In a bow shock type of knot, we indeed usually see an angular offset in CO and SiO emission (e.g., G191.90-11.20S in Figure B1(f), G208.89-20.04E in Figure B7(f), G209.55-19.68S1 in Figure B8(f)). Such bow shocks exhibit successively a CO forward front, SiO peak emission, and then CO peak emission (see also Figure 11). The backward shock detected in CO could be due to either optical depth effects or slower-moving material (discussed later).

4.1.1. Monopolar Molecular Jet

Some SiO jets are observed to be only monopolar, or have bright redshifted knots but faint blueshifted knots. Examples of such asymmetric jets include G203.21-11.20W2, G191.90-11.20S, G205.46-14.56M1, G205.46-14.56S1, and G209.55-19.68S2 in Figure 6 and G211.47-19.27S_B in Figure 8 (last panel). In these cases, the redshifted SiO emission can be observed prominently and the blueshifted emission is fainter, is missing, or has fewer knots. As an example, in G203.21-11.20W2 (Figure 5) the blueshifted CO jet is visible and SiO is not detected in most of the CO knot locations (only fainter B1 and B5). In the case of G209.55-19.68S2, however, the blueshifted jet is completely missing in both CO and SiO emission (Figures 6 (last panel) and B9).

Following the previous shock model by Lee et al. (2001), Santiago-García et al. (2009), Tafalla et al. (2017), and Jhan & Lee (2021), and based on our observation of the ALMASOP sample, a possible scenario for the monopolar jet is illustrated in Figure 11. In most knots, we observe an SiO forward peak and a CO backward peak, and additionally all the SiO+CO peaks are surrounded by a less bright CO front in both space and velocity. Therefore, we have divided the observed emission in the knots into three sublayers: layer i, a forward CO front (in red), which is possibly slow-moving, dense, cooler material; layer iii, a middle SiO+CO front (in green), which could be the faster-moving, denser, and warmer part of the knots; and layer iv, a backward CO front (in blue) that is relatively slow, less dense, and cooler than the middle front. Now, following simulation results by Lee et al. (2001), we introduce another sublayer, layer ii: a compressed layer (black and white lines)

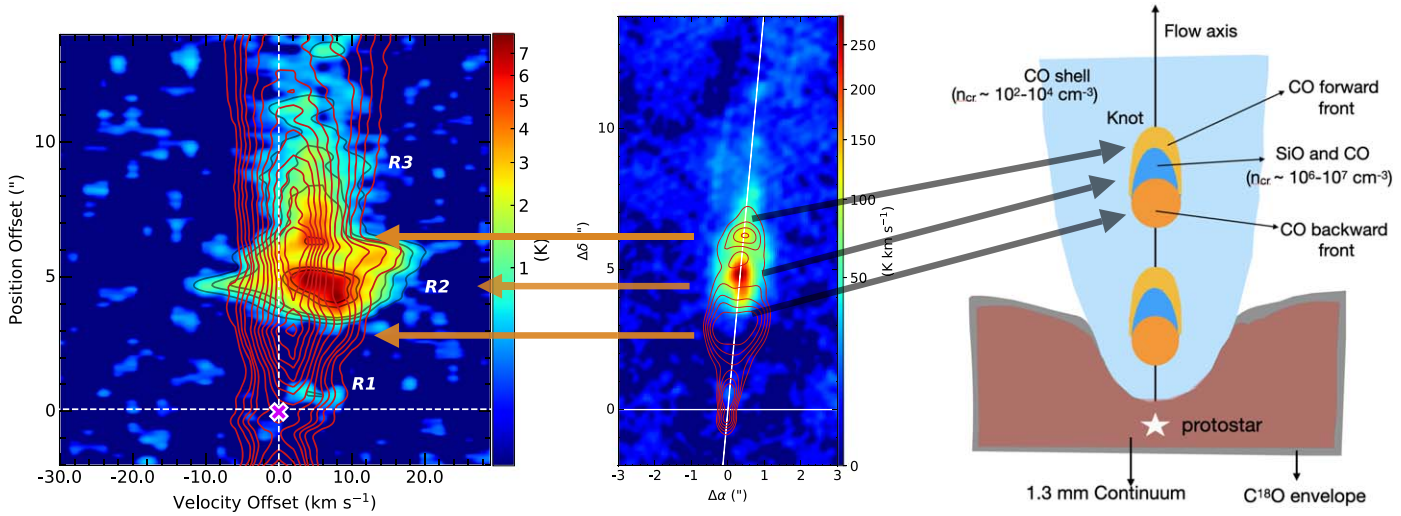

Figure 10. Left: a zoomed-in view of the jet of G191.90-11.21S compared with a schematic diagram. Middle: the SiO integrated map (same as in Figure 6). CO emission is integrated over -4 to $+8$ km s^{-1} with sensitivity $\sigma \sim 6.48$ K km s^{-1} with contour levels at (24, 27, 30, 33, 36) $\times$ σ. The location of the central core is at (0, 0). The left panel is the SiO PV diagram with sensitivity 0.16 K, and CO contours are overplotted at 3 $\times$ (1, 2, 3, 4, 5, 6)σ in red. More details on SiO and CO images are included in Appendix B.1 and Figure B1. Right: the schematic diagram based on observations that illustrate general morphologies of the 1.3 mm continuum and the C^{18}O, CO, and SiO line emission. The 1.3 mm continuum and C^{18}O emission trace the disk and envelope (comparing with Figure 3(a)). CO emission delineates the outflow shell and whole knot structure, including a CO emission forward front, a SiO+CO emission middle shock front, and a CO emission backward front.

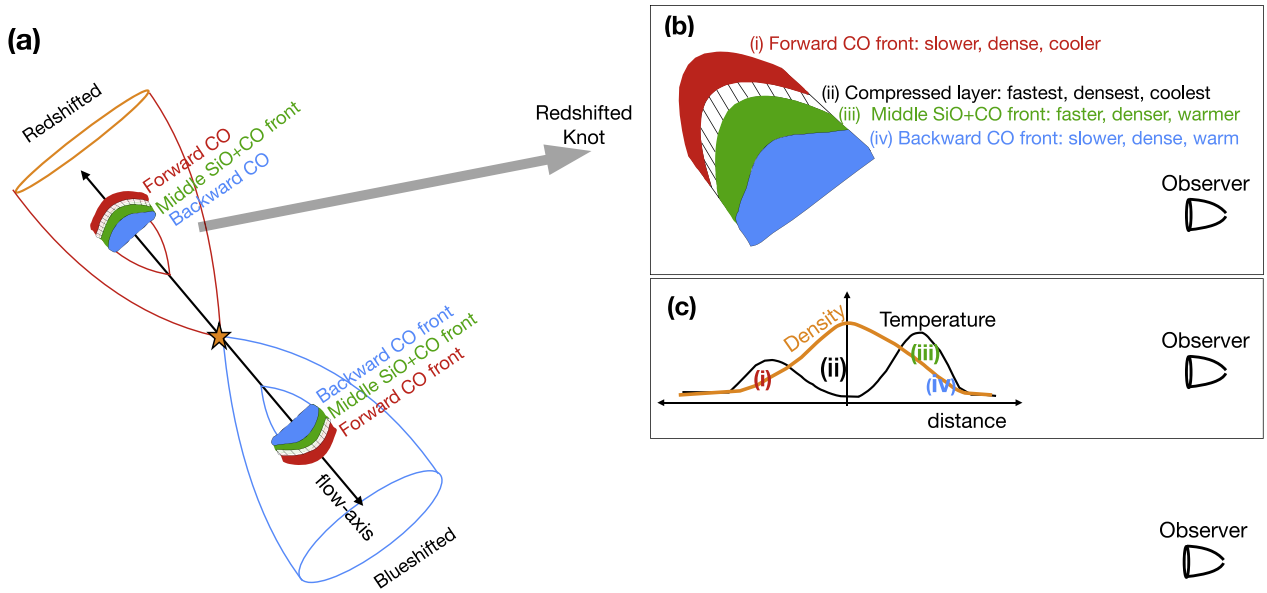

Figure 11. A schematic diagram illustrating a mechanism whereby a bipolar jet can appear to be a monopolar jet. (a) Each knot consists of three observed layers: a forward CO emission front (in red), a middle SiO+CO front (in green), and a backward CO emission front (in blue). (b) Close-up view of a knot in the redshifted lobe. The colors are the same as in panel (a). An additional compressed layer is highlighted between the forward CO front and middle SiO+CO front. (c) The possible temperature distribution of the knot of panel (b) is plotted, following the simulation results by Lee et al. (2001). Layers iii and iv have the highest temperature, and layer i is cooler than layers iii and iv. Layer ii, however, exhibits a temperature discontinuity or is much cooler than the other layers. The density of layer ii is greater than that of the other layers. For the redshifted lobe, an observer can see the middle SiO+CO (layer iii) and backward CO layers (layer iv). For the blueshifted lobe, the scenario is opposite, where an observer can see only a forward CO emission front (layer i). Emission from layers iii and iv might be shielded by the compressed and coolest layer ii. In that case, only the CO jet can be observed in blueshifted emission. If layer i is not dense enough, then even CO emission in the blueshifted lobe of the jet cannot be detected.

between layers i and iii, which could be the fastest-moving, densest, and coolest layer, but one that is not detected in our observations. As predicted by Lee et al. (2001), the density and temperature profiles of different layers are shown in panel (c). In the general scenario of shock processing, a slow-moving layer (layer i) collides with a faster-moving layer, e.g., layers ii+iii, and as a result, a very high density compressed layer ii originates. Since radiative cooling is inversely proportional to density (e.g., Blondin et al. 1990), layer ii should cool faster than the other layers and produce a temperature discontinuity, as shown in panel (c). Layer iii is the transition region between the compressed layer and the slow-moving CO layer iv. It

could be detected if it reaches the critical density of the SiO. Layer iv is the slow-moving trail of layers ii+iii.

In the redshifted lobe, an observer can see layers iii+iv in SiO and CO emission, and the forward CO front at layer i could be shielded by layer ii of high density and low temperature. In the blueshifted lobe, the scenario is opposite to that of a redshifted lobe, where an observer can only see the forward CO material front from layer i, as in the case of G203.21-11.20W2 (Figure 5). Emission from layers iii and iv might be shielded in the compressed layer ii of the highest-density and coolest material; therefore, only the CO jet can be observed in the blueshifted lobe. If the forward front (layer i) is not dense enough and the compressed layer (layer ii) is highly dense and cool, then the jet can remain undetected even with CO emission, as in the case of the blueshifted lobe of G209.55-19.68S2 (Figures 6 and B9), where the jet component is completely missing in both the SiO emission and the CO emission.

The above scenario can explain most of the redshifted SiO monopolar jets in the ALMASOP sample. Another source, NGC 1333-IRAS2A, from the CALYPSO IRAM−PdBI survey exhibits a blueshifted jet only (Codella et al. 2014). G205.46-14.56M1 (Figures 6 and B2) also exhibits one bright blueshifted knot but fainter redshifted SiO emission in the knot location. Indeed, such a scenario is difficult to explain with the above schematic diagram. Therefore, we also suggest that there could be further unknown intrinsic properties driving monopolar jets.

4.1.2. Molecular Jets and Protostellar Evolutionary Phase

Class 0 protostars are observationally defined as being in the youngest phase of star formation, with bolometric temperature $T_{\rm bol} < 70$ K and infrared spectral index of $\alpha_{\rm IR} > 0.3$ (Furlan et al. 2016). Class 0 sources exhibit typically very high accretion and mass-loss rates ($\sim 10^{-6}$ to 10^{-7} $M_\odot$ yr^{-1}) from the protostar, which could produce high-density jets ($(5-10) \times 10^6$ cm^{-3}; Ellerbroek et al. 2013; Lee 2020). The higher transitions of SiO are the most commonly observed tracers of such high-density material (Lee et al. 2014; Podio et al. 2015; Lee et al. 2017a; Podio et al. 2021). While the protostar evolves from Class 0 through Class I and on to the Class II phase, both the accretion and mass-loss rates typically decrease. Therefore, SiO should be a better tracer of jets in the earlier phases of protostars than in the later phases, and the detection of SiO emission in jets more likely indicates protostars in a younger phase and at a higher mass-loss rate.

Molecular jets with SiO emission have been detected in many of the Class 0 protostars, e.g., B335 (Bjerkeli et al. 2019; Imai et al. 2019), HH 212 (Lee et al. 2017a, 2017b), L1157 (Tafalla et al. 2015; Podio et al. 2016), HH 211 (Jhan & Lee 2016; Lee et al. 2018), and IRAS 04166 + 2706 (Santiago-García et al. 2009; Tafalla et al. 2017). One Class I multiple system, SVS13A, composed of VLA4A and VLA4B, was also found with SiO knots (Bachiller et al. 2000; Lefèvre et al. 2017), where VLA4B is identified as the base of the jet (Lefèvre et al. 2017). In this case, however, the spectral classification of the components based on infrared observations could be largely affected by the multiplicity. For example, no SiO jet has been previously detected from an isolated Class I object. On the other hand, SiO jets also have not been detected in extremely young objects, such as the candidate first hydrostatic cores (e.g., Per-Bolo 45, Barnard1b-S, Cha-MM1, CB-17 MMS; see Dutta et al. 2022a, for more details). Recently, the outflow of a very young object, L1451-mm, which was previously believed to be a candidate First Hydrostatic Core (FHSC), has been detected in SiO (3–2) emission from a region very close to the source (<1000 au) by Wakelam et al. (2022). Successive knot-like structures in the jet axis are yet to be confirmed with detections of emission from higher critical density tracers like SiO (5–4) and SiO (8–7).

In the ALMASOP sample, most SiO jet sources are in their Class 0 phase. The source G208.89-20.04Walma is one of the youngest known objects with a SiO jet (Dutta et al. 2022a). Nevertheless, G205.46-14.56S3 (see Dutta et al. 2022b, for more details) and G208.89-20.04E are two Class I objects from the ALMASOP sample with SiO molecular jets observed. The objects with SiO jets exhibit low to high bipolar mass-loss rates in the range of (0.08–5.5) $\times$ 10^{-6} $M_\odot$ yr^{-1} (including both blue- and redshifted lobes).

These results challenge previous thinking about the jet launching timescale and sustainability of jets in the molecular phase. 2D ideal magnetohydrodynamic (MHD) simulations have shown that the outflow is driven by the first core or isothermal core after the first collapse (Larson 1969). After a few hundred years, the central temperature reaches ∼2000 K, a second collapse occurs, and a rotationally supported Keplerian disk forms around the protostars (Machida & Hosokawa 2013; Machida & Basu 2019). The high-velocity jets are believed to be launched from the deep gravitational potential near this second core (or more plainly the actual protostellar core), with high velocity corresponding to the escape velocity of the protostars. These jets are detectable with molecular transitions. Such molecular jets detected with SiO emission continue up to the end of their Class 0 life cycle or the early stage of the Class I phase. Then, the increased central luminosity in evolved protostars may photodissociate the molecular jets, but the density of jets is also decreased owing to reduced mass-loss rates. As a result, jets in more evolved protostars are mostly detected with atomic and ionized emission (Nisini et al. 2015). However, given the typical uncertainty in the evolutionary stages, it should not be that surprising to find a molecular jet among the Class I system. Additionally, there is expected variability in the accretion, and therefore likely also in the ejection. Submillimeter and mid-infrared continuum monitoring suggests that accretion variability is common for Class 0 and I protostars (Lee et al. 2021; Park et al. 2021). These episodic events potentially could give rise to elevated ejection rates even at later stages.

In the ALMASOP sample, a large fraction of Class 0 protostars do not exhibit molecular jets (Appendix D and E); these could be relatively evolved protostars with reduced accretion/ejection activity.

4.2. Jet-driven or Wind-driven Outflow

Whether outflowing material is jet or wind driven is a long-standing issue with no clear conclusion yet, due to the lack of a statistically significant observational sample. We take the opportunity of the large ALMASOP data set to explore this question while studying this unique sample of protostars with high-resolution and high-sensitivity observations with simultaneous observations of jet and winds (or outflow). In the ALMASOP sample, we observe four different types of jet and outflow ejection: (i) a narrow CO wind shell (or outflow) but no SiO jet, (ii) a narrow CO wind shell and a SiO jet, (iii) a wide-

angle CO wind shell but no SiO jet, and (iv) a wide-angle CO wind shell and a SiO jet. We note that SiO (5–4) and CO (2–1), both of which could be optically thick toward the innermost region of the knots, could be detected with higher-density tracers like SiO (8–7) and CO (3–2).

If we accept that outflow is jet driven, then the SiO jets with CO outflow can be straightforwardly explained (cases ii and iv). For objects with no SiO jet and a narrow CO wind shell (case i), the outflow could be wind driven. On the other hand, those objects with a wide-angle CO shell and no SiO jet (case iii) could be evolved protostars, and their jets could be detected with ionized jet tracers. The ALMASOP sample, however, consists of mostly very young Class 0 systems that should drive high-density jets that may not have been detected with the lower transition of SiO and CO (as discussed in Section 4.1.2). It is also possible that these outflows, indeed, do not associate with any jet, or no strong jet that could entrain outflow material, which could possibly indicate that outflows are wind driven.

4.3. Origin of Gas-phase SiO

SiO emission has been frequently reported in previous studies as originating in the shock regions along protostellar jets in their earliest phases. As discussed earlier, we observe 22 fields with SiO emission in the ALMASOP sample (19 in this study, 3 previously published in Dutta et al. 2022a, 2022b). In these 22 fields, 17 protostars are confirmed to have SiO emission along the jet axis. Three other objects display bow-shock-like extended SiO emission along their jet axes, which could be associated with jets, but their small velocity ranges or insufficient velocity information make it difficult to be sure. One source exhibits SiO in the collision zone between two outflows, and for another the driving source of SiO emission is unclear. So far, the precise origin of SiO in the jet is still not constrained owing to the lack of significant observations at high resolution and high sensitivity.

There are two competing scenarios in the literature describing the mechanism of SiO formation. In the "grain sputtering" scenario, SiO could originate at the shock region within the jet itself through grain sputtering due to ion–neutral decoupling (Schilke et al. 1997; Panoglou et al. 2012). In this scenario grains are most likely coming with the launching material, originating possibly at the larger radii of the disk and inner envelope. In the "dust sublimation zone" scenario, if the jet is launched from the base or within the dust sublimation radius ($R_{\rm sub} \sim 0.15\,{\rm au} \times \sqrt{L_{\rm bol}/L_\odot}$; Yvart et al. 2016), the stellar far-ultraviolet (FUV) emission there can sublimate the silicate dust grains and release Si^+ into the gas phase near the launching zone. Once the jet is launched from the base, the material starts cooling and Si^+ recombines with oxygen through a "gas-phase reaction" to produce SiO within the jet. On the other hand, the presence of FUV excess emission can also lead to the photodissociation of molecules and cause a dramatic decrease in SiO and CO abundances near the jet base (Schilke et al. 1997). Tabone et al. (2020) also suggest that molecules like SiO can be synthesized in fast and collimated dust-free disk winds through a gas-phase formation route if the disk wind is sufficiently warm and there is a high enough mass-loss rate.

Assuming optically thin CO and SiO emission, we measure the $X_{\rm SiO}/X_{\rm CO}$ for all the SiO-emitting jet sources from the innermost knots (B1 and R1 knots) and plot these values as a function of jet mass-loss rate in Figure 12. We also plotted two well-known Class 0 objects with SiO jets, HH 211 from Jhan & Lee (2021) and HH 212 from Lee et al. (2007a), for comparison with the ALMASOP sample. We note that SiO (5–4) could be optically thicker toward the dense shock than CO (2–1) in the same region. Therefore, the SiO emission is likely the lower limit, and the $X_{\rm SiO}/X_{\rm CO}$ is the lower limit in this case. From our observations, we see that SiO jets tend to have $X_{\rm SiO}/X_{\rm CO}$ in the range $\sim 5 \times 10^{-4}$ to 10^{-2}. The majority of the ALMASOP sources have mass-loss rates $\dot{M}_j < 10^{-6}\ M_\odot\,{\rm yr}^{-1}$. We compare this sample to the tracks for different dust-to-gas mass ratios (Q) of Tabone et al. (2020; solid curves), computed using 1D laminar winds launching from 0.15 au radius, which suggests that the SiO jets are possibly dust-poor.

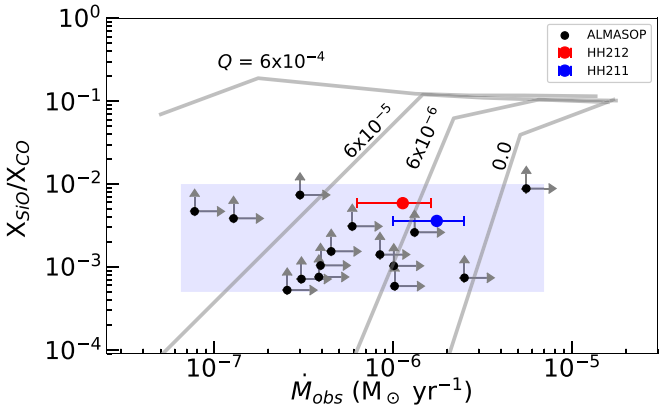

Figure 12. SiO-to-CO abundance ratios, $X_{\rm SiO}/X_{\rm CO} = N_{\rm SiO}/N_{\rm CO}$, are plotted as a function of observed jet mass-loss rate ($\dot{M}_j$ or $\dot{M}_{\rm obs}$). The error bars in the abundance ratios represent the lower limit since SiO is optically thicker than CO. The abundance ratios of HH 212 (in red) and HH 211 (in blue) are calculated from the column densities in the published literature (HH 212, Lee et al. 2007a; HH 211, Jhan & Lee 2021). Asymptotic abundance ratios (gray lines) are adopted from Tabone et al. (2020), estimated using the Paris–Durham shock code designed to model irradiated environments and a laminar 1D disk wind model. The model considered a streamline launched at $R_0 = 0.15$ au with $T = 1000$ K in the disk for dust-free models (dust-to-gas mass ratio $Q = 0$) and dust-poor models ($Q = 6\times10^{-6}$, 6×10^{-5}, and 6×10^{-4}), as well as for different values of wind mass-loss rates ($\dot{M}_w$) referring to theoretical models that account for the origin of jets. The shaded region indicates the location of most of the observed data.

These sources are observed to have higher abundances ($X_{\rm SiO}/X_{\rm CO} \sim 5\times10^{-4}$ to 10^{-2}), which could be much higher if we consider that SiO is optically thicker than CO (indicated as the lower limit of error bars in Figure 12), for relatively smaller mass-loss rates (73% sources within $(0.1–0.4) \times 10^{-6}\ M_\odot\,{\rm yr}^{-1}$). Tabone et al. (2020) show that SiO exhibits a steeper increase with mass-loss rate and it only becomes abundant for high wind mass-loss rates ($\dot{M}_w \geqslant 0.2 \times 10^{-6}\ M_\odot\,{\rm yr}^{-1}$). They manifested an SiO-rich environment for $\dot{M}_w \geqslant 2 \times 10^{-6}\ M_\odot\,{\rm yr}^{-1}$ in the dust-free wind and $\dot{M}_w \geqslant 0.5 \times 10^{-6}\ M_\odot\,{\rm yr}^{-1}$ for the dust-wind (dust-poor) model. Glassgold et al. (1991, see their Figure 6) suggest that for a typical mass-loss rate of $\dot{M}_w \sim 3 \times 10^{-6}\ M_\odot\,{\rm yr}^{-1}$ $X_{\rm SiO}/X_{\rm CO}$ could be enhanced to $\sim 5 \times 10^{-2}$. This value of mass-loss rate is somewhat higher than our measured lower limits. Therefore, it is evident that our measured mass-loss rates are slightly smaller than the model prediction to explain such high observed SiO abundances.

Discrepancies in the observed mass-loss rates and $X_{\rm SiO}/X_{\rm CO}$ with model predictions could be addressed by the different methods used for measuring mass-loss rates. Glassgold et al. (1991)

and Tabone et al. (2020) considered mass loss to be spatially extended as a wide "wind" (i.e., $\dot{M}_w$). On the other hand, we estimate the jet mass-loss rate ($\dot{M}_j$) from the innermost part of the outflowing cavity, i.e., along the jet axis. Hence, the mass-loss rates along the inner jet axis in this study could have underestimated the actual mass-loss rates (see, e.g., Figure 3 of Shu et al. 1995). Therefore, our $\dot{M}_j$ values estimated along the jet axis could be biased too low to compare accurately with the model's prediction.

Another possibility to explain the high SiO-to-CO ratios is that the efficiency of CO production is less than SiO if the SiO and CO within the jet originate by the same process. Following Draine & Salpeter (1979), Nozawa et al. (2006), and Hu et al. (2019), the dust sputtering timescale can be defined as

$$t_{\rm sput} \equiv \frac{a}{3 n_{\rm H} Y_{\rm tot}},$$
$$\approx 0.33\ {\rm Myr} \left(\frac{a}{\mu{\rm m}}\right)\left(\frac{n_{\rm H}}{{\rm cm}^{-3}}\right)^{-1}\left(\frac{Y_{\rm tot}}{10^{-6}\ \mu{\rm m\ yr^{-1}\ cm^3}}\right)^{-1}, \quad (5)$$

where grain size is denoted by a and hydrogen number density of the gas is denoted by $n_{\rm H}$. The erosion rate $Y_{\rm tot} \equiv (da/dt)/n_{\rm H}$ is adopted from Nozawa et al. (2006). For thermal sputtering, $Y_{\rm tot}$ depends on the temperature of the region and grain sputtering occurs above $\sim 10^5$ K. For nonthermal sputtering, the jet velocity should be above ~ 30 km s^{-1}. In the jets observed here, the temperatures are much smaller than the thermal sputtering limit. Nonthermal sputtering, however, could occur at a high jet velocity. We estimate that the typical critical density $n_{\rm cr,sio} \sim 10^6$ cm^{-3} is needed to excite SiO in the shocks (Section 1), which could also be considered as a typical postshock density in the jet. Therefore, the preshock density is expected to be smaller than $n_{\rm cr,sio}$ along the jet direction, i.e., $<10^6$ cm^{-3}. For a mean jet velocity of ~ 50 km s^{-1}, we estimate sputtering timescales of 2.75–275 yr for silicate dust and 5.4–540 yr in the case of carbon dust, for preshock densities $\sim 10^6$–10^4 cm^{-3}, respectively. Hence, for high preshock density and high-velocity jets, sputtering is a plausible mechanism to form SiO and CO, even in the nearest knots with dynamical timescales less than 100 yr. The erosion rate of carbonaceous dust grains (producing CO) is smaller than that of silicate dust grains (producing SiO) for the same jet velocity (Nozawa et al. 2006). Therefore, Equation (5) suggests that the SiO formation timescale is half that of CO formation for the same preshock density, which could be the reason for higher SiO-to-CO ratios in the knots. CO, however, can easily sublimate from grain mantles at temperatures of $\sim 20-25$ K, where sputtering is not necessary. Therefore, it is unlikely that the majority of the CO is formed later than SiO.

The "dust sublimation zone" scenario is well applicable to the objects with SiO emission in the knots close to the source (e.g., G205.46-14.56M1, G205.46-14.56S1, G205.46-14.56S3, G206.12-15.76, G206.93-16.61W2, G208.68-19.20N1, G208.68-19.20N3, G208.89-20.04E, G208.89-20.04Walma, G209.55-19.68S1, G209.55-19.68S2, G210.37-19.53S, G211-19.27S_B G215.87-17.62M). The jets being likely dust-poor, it is possible that gas-phase Si^+ is coming from the jet base and undergoes rapid formation of SiO within the jet. As a consequence, we observe SiO in the knots, even in the nearest knots to the source. For the "grain sputtering" scenario, the grains being carried with the launching material from the disk-envelope region take a longer time (>100 yr) to create high abundances of SiO within the jets (e.g., Podio et al. 2021). Although the dynamical timescales of the nearest knots could not be measured reliably for these sources owing to the poor spatial resolution of the studied observations, in most cases it is likely less than 100 yr. Such short timescales are not long enough to produce the high $X_{\rm SiO}/X_{\rm CO}$ ratios observed in this sample through the "grain sputtering" method, except in cases where the preshock density is very high ($\sim 10^6$ cm^{-3}). As an example, for G191.90-11.20S (Figures 10(a)–(b) and B1(f)), the jet-emitting zone is uncertain, since the nearest knot (R1) is very faint and the brightest knots (e.g., R2) are far away from the source. The grain sputtering scenario is a possible mechanism to form SiO within the jet even for a low preshock density ($\sim 10^4$ cm^{-3}). A few other objects also exhibit SiO emission in the outflow direction, such as G192.32-11.88N, G200.34-10.97N, G205.46-14.56M2, and G209.55-19.68N1. Meanwhile, SiO emission in the field of G209.55-19.68N1 is clearly in the collision zone between two outflows. The SiO emission in the remaining three cases could be processed in the location through grain sputtering or collision between the outflow material with ambient clouds.

To summarize, we suggest that gas-phase Si^+ is originating within the dust sublimation zone near the base of the source and is carried along with the launching material, later combining with oxygen within the jet to form SiO. We cannot, however, fully exclude the grain sputtering mechanism using the present observations. Further high-sensitivity and high velocity resolution observations could provide more constraints on the SiO formation scenario. Such observations could provide a more stringent view of the nearby knots and allow measurement of jet rotation that can in turn constrain the jet launching radius (Lee et al. 2017a).

4.4. Accretion and Ejection Process

The ejected material along the jet can carry vital information about the present evolutionary status, history of the accretion process, and final mass budget of the protostar. The properties of the jet ($V_{j,\rm cor}$, $\dot{M}_j$, $L_{j,\rm kin}$, $\mathcal{T}_{\rm knot}$) are possibly associated with the interior properties of the protostars and the physical structure of the surrounding material (e.g., stellar luminosity, radius, mass of the core). In this section, we explore the intercorrelation of the jet ejection with the other properties of the protostars, such as bolometric luminosity and the mass of the surrounding envelopes.

We estimated mass acceleration rates $\dot{M}_{\rm acc}$ based on the total jet mass-loss rates $\dot{M}_j$, the bolometric luminosity $L_{\rm bol}$, and the total kinetic luminosity of both the blueshifted and redshifted lobes $L_{j,\rm kin}$, as presented in Table 3. The accretion rate is defined as

$$\dot{M}_{\rm acc} \sim \frac{(L_{\rm bol} + L_{j,\rm kin}) R_*}{G M_*}\ M_\odot\ {\rm yr}^{-1} \quad (6)$$

assuming that both the bolometric luminosity and kinetic luminosity originate entirely from accretion. For these calculations, we assume a stellar radius of $R_* \sim 2\ R_\odot$ (Stahler 1988). The jet-ejecting protostars consists of mostly Class 0 and two early Class I objects. Therefore, we assume that the stellar cores have not evolved much so that their central objects are in the low mass range of $M_* = 0.05-0.30\ M_\odot$ (Simon et al. 2000; Yen et al. 2017). Specifically, we consider an average mass of $M_* = 0.1\ M_\odot$ for all the objects to estimate $\dot{M}_{\rm acc}$. The ratio of

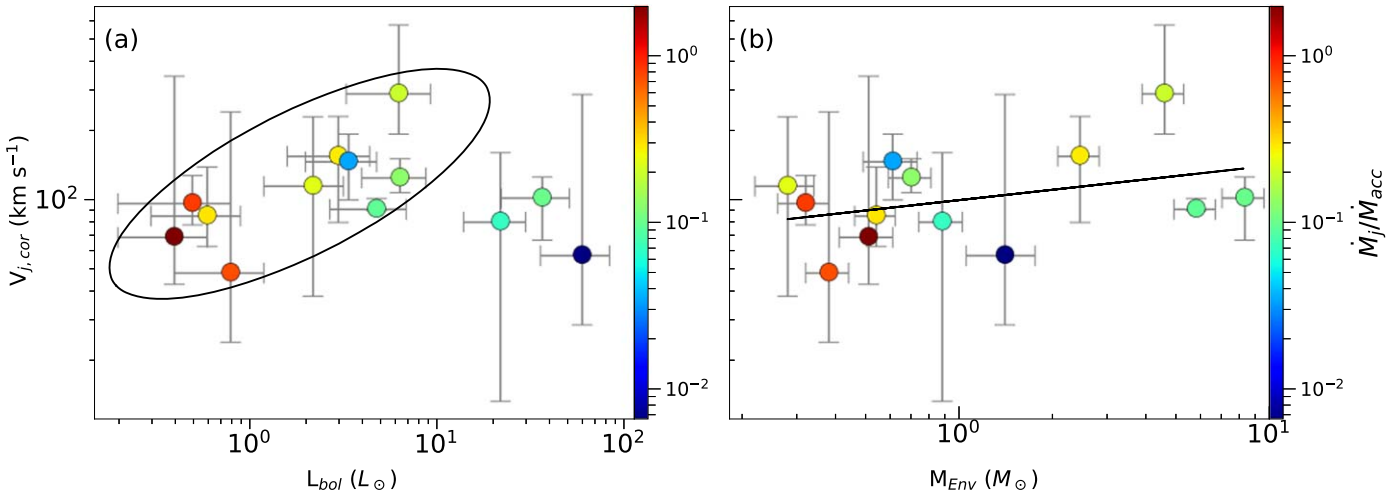

Figure 13. (a) Jet velocities (V_j) are plotted as a function of (a) bolometric luminositiy ($L_{\rm bol}$) and (b) envelope mass ($M_{\rm Env}$) estimated from ACA continuum. The color bar indicates the ratio of mass ejection rate to accretion rate ($\dot{M}_j/\dot{M}_{\rm acc}$), where the mass accretion rates $\dot{M}_{\rm acc}$ were estimated for a protostellar mass of 0.1 $M_\odot$ and total luminosity using Equation (6). Objects with increasing trends are marked with an ellipse to guide the eye. A linear fit of the data points is shown in panel (b).

$\dot{M}_{\rm j}/\dot{M}_{\rm acc}$ ranges from 0.003 to 2.1. In the subsequent sections, we discuss how these $\dot{M}_{\rm acc}$ values are correlated with the central driving force of the jet and explore possible implications on the chemical composition of the disk and planet formation.

4.4.1. Jet Velocity: Dependence on Luminosity and Envelope Mass

Figure 13 shows the jet velocity of the ALMASOP objects as a function of luminosity (panel (a)) and envelope mass (panel (b)). In panel (a), most of the objects (marked with an ellipse) exhibit a correlation between $V_{j,\rm cor}$ and $L_{\rm bol}$. Large error bars of two objects beyond the ellipse possibly restrict them to be located within the correlation zone. The $\dot{M}_j/\dot{M}_{\rm acc}$ ratio also likely decreases with bolometric luminosity from $L_{\rm bol} \sim 0.2$ to 10 $L_\odot$, which could be due to the dependency of $\dot{M}_{\rm acc}$ on $L_{\rm bol}$ (Equation (6)), indicating a possible reduction in ejection-to-accretion activity. The correlation of $L_{\rm bol}$ with protostellar evolution is not clear, however, as indicated from studies of a large protostellar sample (Dunham et al. 2014b). Note that, reduced ejection and accretion activity with protostellar evolution were reported in Ellerbroek et al. (2013) and Lee (2020; see their $\dot{M}_j$ vs. $\dot{M}_{\rm acc}$ plots).

In panel (b), most of the $V_{j,\rm cor}$ values appear to be correlated with the mass of the envelope $M_{\rm Env}$. A linear fit is consistent with the equation

$$\log(V_{j,\rm cor}) = (0.15 \pm 0.11)\log(M_{\rm Env}) + (2.0 \pm 0.05). \quad (7)$$

The Spearman statistical test gives the correlation coefficient 0.28 and the p-value 0.35, suggesting the existence of a correlation although statistically not robust. More observations are necessary to determine a statistically significant correlation.

We do not see any clear dependence of jet velocities on $\dot{M}_j/\dot{M}_{\rm acc}$ here. Higher envelope masses may increase the accretion rates given the larger local mass reservoir. In addition, larger protostellar masses have higher gravitational potentials from which high-velocity jets are ultimately powered. At evolved protostellar phases, however, the jets become ionized and accretion rates also decrease, but the jet will still be at high velocity owing to the higher mass of the central protostars. A consistent measurement of the protostellar masses from kinematics will be more helpful to illustrate this scenario.

4.4.2. Jet Mass Loss: Dependence on Luminosity and Envelope Mass

Figure 14(a) shows the observed mass ejection rates $\dot{M}_j$ as a function of the bolometric luminosity of the objects. We compare ALMASOP objects with some well-known SiO jet objects from the literature. The $\dot{M}_j$ and $\dot{M}_{\rm acc}$ of B335 are comparable to those of low-luminosity sources. The objects L1157, HH 212, HH 211, and L1448C share similar properties to ALMASOP objects of $L_{\rm bol} \sim$ 3–10 $L_\odot$. Objects with low $\dot{M}_j/\dot{M}_{\rm acc}$ (bluish colors) exhibit lower $\dot{M}_j$ rates with increases in central luminosity. The objects with high $\dot{M}_j/\dot{M}_{\rm acc}$ (green, yellow, orange, and red colors), however, do not show any obvious correlation.

Figure 14(b) shows the $\dot{M}_j$ values as a function of envelope mass, as estimated from the ACA continuum. Although there is large scatter in the data points, we see a tentative correlation of jet mass-loss rate with envelope mass. Further, we do not see any obvious effect of multiplicity on the mass accretion and ejection phenomena. A linear fit reveals a correlation as

$$\log(\dot{M}_j) = (0.53 \pm 0.23)\log(M_{\rm Env}) - (6.26 \pm 0.11). \quad (8)$$

The Spearman correlation coefficient 0.41 and the p-value 0.12 suggest the existence of a correlation; however, the conclusion is not statistically robust. More data are required to determine whether the observed candidate relation holds true. No clear dependence of jet mass-loss rates on the $\dot{M}_j/\dot{M}_{\rm acc}$ was found.

4.4.3. Episodic Ejection: Dependence on Luminosity and Envelope Mass

As discussed earlier, all of the SiO jets are discrete, clumpy, knot-like and bow-shock-like structures. Some are roughly equally spaced and may trace a quasi-periodic ejection. We estimated the mean periods between knots to be in the range of ∼20−175 yr, with the error bars based on the uncertainties in the inclination angle, jet velocity, and knot spacing. These discontinuous structures may be produced as a result of the temporal variations in the jet velocity and density. Although the mechanisms that drive the variations in jet density and velocity

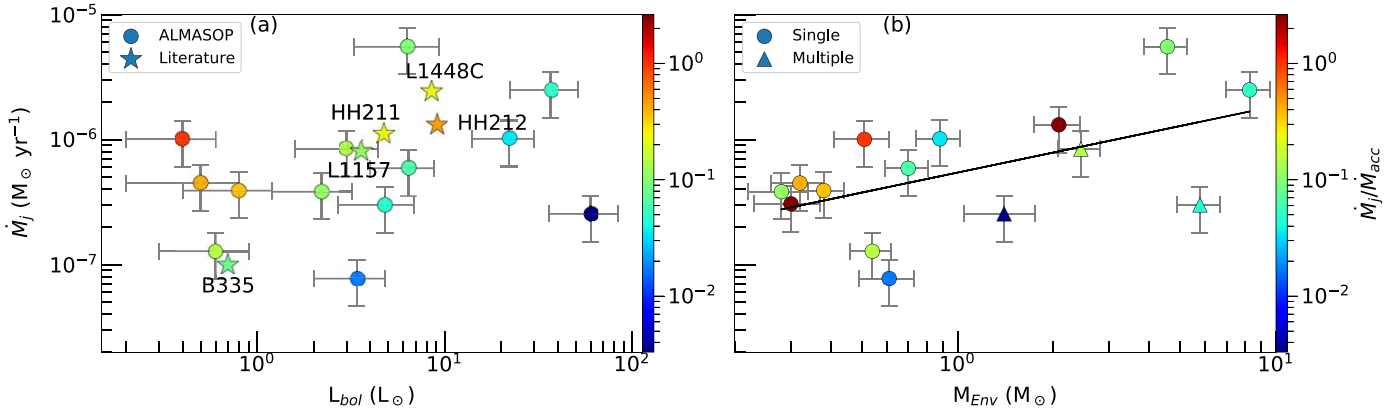

Figure 14. (a) Jet mass-loss rates ($\dot{M}_j$) are plotted as a function of (a) bolometric luminosity ($L_{\rm bol}$) and (b) envelope mass $M_{\rm Env}$. The color bar indicates the ratio of mass-loss rate to accretion rate ($\dot{M}_j/\dot{M}_{\rm acc}$). Stars in panel (a) are data points for different well-known SiO jet objects adopted from the literature (e.g., Lee 2020). The triangles in panel (b) are multiple sources within a common envelope. A linear fit of the data points is also shown in panel (b).

are still not well understood, the general consensus is that they are driven by the quasi-periodic perturbations of the underlying accretion in the disks. A few potential mechanisms have been proposed that could produce variations of accretion (e.g., Audard et al. 2014; Lee 2020; Fischer et al. 2023): (i) accretion driven by binary interaction where the variations are modulated by the orbital timescale, (ii) gravitational instabilities governed by envelope accretion, (iii) planetesimal accretion onto the central protostar, and (iv) gravitational instabilities produced at dust sublimation zones. In a few cases, episodes have been reported in the jets of objects such as HH 34 (270 and 1400 yr; Raga et al. 2002), HH 111 (60 and 950 yr; Raga et al. 2002), and HH 212 (1, 60, and 605 yr; Zinnecker et al. 1998). Different periods in a single system could be linked to different periodic perturbations of the underlying accretion in the disk. Further evidence for these timescales comes from monitoring protostars at mid-infrared and submillimeter wavelengths. The JCMT Transient Survey (Herczeg et al. 2017) has uncovered submillimeter brightness variability with what appear to be decades-long timescales from many deeply embedded protostars (Lee et al. 2021). Similarly, an analysis of mid-infrared monitoring of over 5000 young stellar objects (YSOs) by NEOWISE recovered many long-term secular variables among the most deeply embedded members of the sample (Park et al. 2021).

In our observations with relatively small FOVs, we observe mostly single periods or quasi-periodic knots/bow shocks. As a result, we estimate only mean periods of events. The corresponding orbital radii for those periods can be estimated from Kepler's third law of orbital motion following

$$a = \left(\frac{GM_* T^2}{4\pi^2}\right)^{1/3} = \left(\frac{M_*}{M_\odot}\right)^{1/3}\left(\frac{T}{\rm yr}\right)^{2/3} {\rm au}, \quad (9)$$

where $T = \mathcal{T}_{\rm knot}$ is the mean episode of ejection and M_* is the mass of the central protostars, which is assumed to be 0.05 $-$0.30 $M_\odot$. The Keplerian radius corresponding to the episodes is estimated to be 2.0$-$25 au (including error bars) for different objects (Table 4). We estimated two sets of radii for two masses. In the absence of studies on large-scale episodes beyond our FOVs and without confirmations of binary components within those perturbation zones, it is difficult to link accretion perturbation to any particular mechanism. Since the ALMASOP sample contains mostly Class 0 and early Class I, most sources are expected to have small or intermediate disks, and so the perturbation may have originated within the disk or in the outskirts of the disk. Further studies of disk size and large-scale periodicity could confirm the origins of the accretion variability.

Table 4
Perturbed (Keplerian) Radius in the Disk Plane for the Knots in the Jet

Source	Keplerian Radius (au)	
	(0.05 $M_\odot$)	(0.30 $M_\odot$)
G191.90-11.21S	$7.9^{+3.0}_{-5.2}$	$14.4^{+5.4}_{-9.5}$
G203.21-11.20W2	$6.3^{+1.1}_{-1.2}$	$11.5^{+2.1}_{-2.2}$
G205.46-14.56M1	$7.9^{+2.5}_{-3.1}$	$14.4^{+4.5}_{-5.7}$
G205.46-14.56S1	$3.9^{+8.9}_{-1.4}$	$7.0^{+16.2}_{-2.6}$
G205.46-14.56S3	$5.3^{+1.8}_{-1.4}$	$9.6^{+3.3}_{-2.5}$
G206.12-15.76	$3.6^{+2.4}_{-0.8}$	$6.5^{+4.4}_{-1.5}$
G206.93-16.61W2	$2.4^{+2.4}_{-1.1}$	$4.4^{+4.3}_{-2.0}$
G208.68-19.20N1	$2.6^{+0.8}_{-0.4}$	$4.8^{+1.4}_{-0.7}$
G208.68-19.20N3	$6.9^{+2.9}_{-2.4}$	$12.5^{+5.3}_{-4.4}$
G208.89-20.04E	$5.1^{+5.5}_{-1.9}$	$9.3^{+10.1}_{-3.5}$
G208.89- 20.04Walma	$11.6^{+6.9}_{-7.6}$	$21.0^{+12.5}_{-13.9}$
G209.55-19.68S2	$2.9^{+1.0}_{-0.6}$	$5.3^{+1.9}_{-1.0}$
G210.37-19.53S	$3.0^{+1.4}_{-0.9}$	$5.4^{+2.5}_{-1.7}$
G210.49-19.79W	$6.7^{+4.0}_{-1.0}$	$12.2^{+7.2}_{-1.7}$
G215.87-17.62M	$6.0^{+1.7}_{-1.6}$	$10.9^{+3.1}_{-3.0}$

We plotted $\mathcal{T}_{\rm knot}$ as a function of bolometric luminosity and envelope mass in Figures 15(a) and (b), respectively. Figure 15(a) exhibits a considerable scatter of data points with very large error bars. The lack of a clear trend with luminosity may be due to variable accretion. The observed luminosity could represent the true evolutionary sequence of the protostars. In Figure 15(b) there is a mild anticorrelation between the $\mathcal{T}_{\rm knot}$ and $M_{\rm Env}$. A linear least-squares fit provides

$$\log(\mathcal{T}_{\rm knot}) = (-0.22 \pm 0.16)\log(M_{\rm Env}) - (1.70 \pm 0.08). \quad (10)$$

The Spearman statistical test, however, provides the correlation coefficient $-$0.29 and the p-value 0.3, suggesting the existence of an anticorrelation that is not statistically robust. More

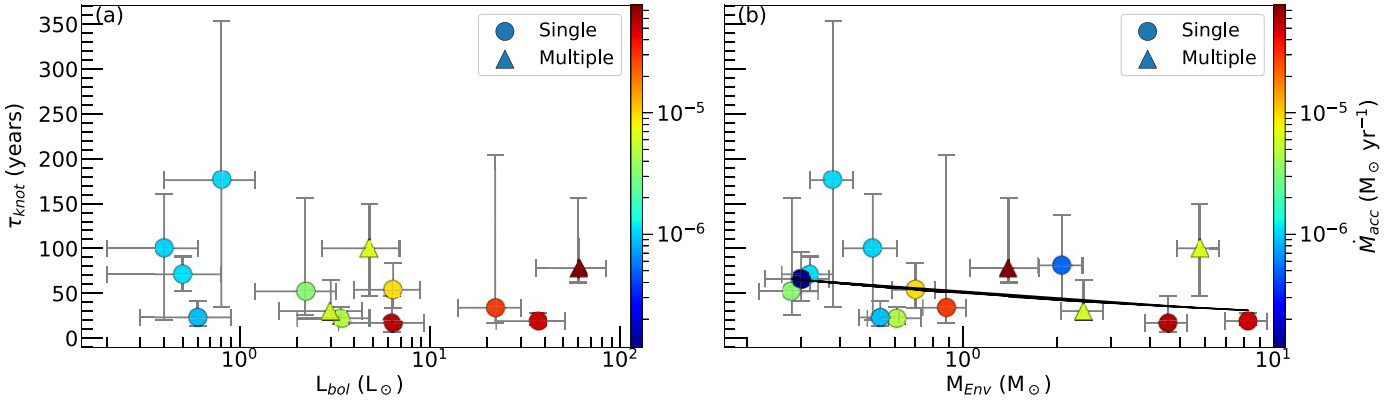

Figure 15. Mean ejection periods ($\mathcal{T}_{\rm knot}$) are plotted as a function of (a) bolometric luminosity ($L_{\rm bol}$) and (b) envelope masses ($M_{\rm env}$). Single and multiple sources are shown with circles and triangles, respectively. The color scale indicates the mass accretion rate ($\dot{M}_{\rm acc}$). The straight line in panel (b) is the linear fit to the data points.

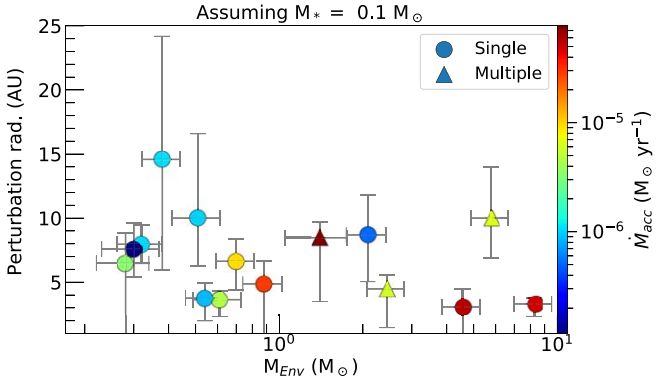

Figure 16. Keplerian radii corresponding to the observed mean periods of episodic events are plotted as a function of envelope masses. A stellar mass $M_* = 0.1\ M_\odot$ is assumed for all protostars. All notations are the same as in Figure 15(b).

observations are key to determine a robust anticorrelation. In Figure 16 the Keplerian perturbation radius corresponding to the periods of ejection is plotted as a function of envelope mass, assuming the same protostellar mass $M_* = 0.1\ M_\odot$. The data points scatter with large error bars without any clear correlation. There are three wide binary systems with separations >100 au in the plots. None have separations matching the Keplerian perturbation radius. Hence, it is unlikely that these respective accretion/ejection events are driven by binary orbital dynamics.

Future modeling of accretion bursts and comparison between observed episodic knot timescales and time-series photometric variability monitoring of the same objects will provide more insightful connections to the accretion and ejection.

4.4.4. Episodic Ejection: Implication for Complex Organic Molecule and Planet Formation

As discussed earlier, the typical duration between consecutive knots, or the knot periodicity, in the jets is possibly driven by protostellar accretion with episodic bursts (Vorobyov et al. 2018; Fischer et al. 2023). Meanwhile, the accretion outburst could have a significant impact on regulating the chemical composition or COM formation in the disk/envelope region (Taquet et al. 2016). Currently it is difficult to estimate the accretion periodicity precisely from the current accretion luminosity monitoring. Therefore, in this section we propose an alternative indirect method using the episodic ejection in the jet as a proxy to the accretion timescale to correlate episodic accretion events with COM formation timescales.

During each episodic outburst, the central luminosity increases to a maximum $L_{\rm max}$. Subsequently, the surrounding disk temperatures increase and the various snowlines shift outward. After each outburst, during the quiescent phase, the luminosity decreases exponentially with time to a minimum $L_{\rm min}$, the surrounding disk temperatures decrease, and the snowlines shift inward. Therefore, episodic outbursts affect the variation of temperature within the disk. When the temperature increases, more molecular ices on grains convert to the gas phase, which increases the possibility of complex molecule formation through gas-phase reactions (Taquet et al. 2016; Lee et al. 2019b; Jørgensen et al. 2022). During the post-outburst quiescent phase, gas-phase molecules could recondense to ice. Following Charnley et al. (2001) and Rodgers & Charnley (2003), the freezeout rate for a neutral molecule, X, can be estimated as

$$\lambda(X) = 2.3 \times 10^{-18}\left(\frac{T}{m(X)}\right)^{0.5} n_{\rm H_2}\ ({\rm s}^{-1}). \quad (11)$$

To explore variations of chemistry in these systems, we assume a mean grain radius of 0.1 μm and a grain abundance of 10^{-12} at the protostellar envelope outside the hot corino (e.g., Rodgers & Charnley 2003; Jørgensen et al. 2022). T is the temperature of the gas in kelvin, $m(X)$ is the molecular weight of the molecule X, and $n_{\rm H_2}$ is the molecular hydrogen density in cm^{-3}. CH_3OH is one of the simplest COMs, which could produce CH_3OCH_3, CH_3OCHO, $C_2H_5OCH_3$, $C_2H_5OC_2H_5$, and C_2H_5OCHO through gas-phase reactions (Taquet et al. 2016). In the case of CH_3OH, for an approximate ice-evaporation temperature $T \sim 100$ K and a density of $n_{\rm H_2} \sim 10^7$ cm^{-3} in the outer disk hot-core boundary region (Jørgensen et al. 2022), the freezeout timescale becomes ~780 yr (710 yr for a maximum temperature of 120 K or 930 yr for the 70 K evaporation temperature of CH_3OH). Based on ejection periods, the outburst timescales of 20−175 yr for the present ALMASOP objects are less than the freezeout timescale. Therefore, each episode of outburst, presumably associated with individual episodic accretion bursts (e.g., Vorobyov et al. 2018), might be linked to the temperature variation of the outer

disk and consequently the formation history of COMs through gas-phase reactions. The magnitude of temperature variation is, however, difficult to measure under these assumptions, and thus more detailed modeling connecting luminosity and temperature variations with episodic ejections is needed to determine the precise importance of episodic events on the COM formation.

Some of the studied objects have been classified as "hot corinos" by Hsu et al. (2022) owing to detection of several COMs around them. We have adopted the CH_3OH radius from that work and plotted it in Figure 17. The water sublimation radius $R(100)$ in the envelope at a given luminosity (black line) has been calculated by the equation in Bisschop et al. (2007). Most of the sources have much larger R_{CH_3OH} than what is expected from their current luminosities. The dashed lines show $R(100\ \mathrm{K})$ when the luminosity is enhanced by a certain factor. The R_{CH_3OH} of many sources is consistent with the enhancement factor of 10. G210WA and G211S seem to be in their burst phases since $R_{CH_3OH} \sim R(100\ \mathrm{K})$, and their L_{bol} values are much larger than those of typical protostars. The large discrepancy between the methanol emission size, R_{CH_3OH}, and the $R(100)$ estimated from the current luminosity suggests that all sources have had prior accretion bursts, and the intensity of the "last" outburst would cause the final observed radius increase. Future time-series monitoring of accretion luminosity variability will allow direct comparison with episodicity in the jet knots and potentially supply examples of the radii of COMs increasing. Such observations would provide more precise details on the connection between accretion/ejection outburst and the formation of COMs.

Since there is growing evidence of grain growth and planet formation in the early phase (e.g., Harsono et al. 2018), the emerging planet's chemical composition, especially in the outer disk, will be largely impacted by the repetitive outbursts. Evidence of the role of episodic outbursts on the evolution of disks and chemical composition of planets was also reported for young Class 0 binary system NGC 1333-IRAS2A (Jørgensen et al. 2022).

4.5. Correlation of Outflow Force with Luminosity and Envelope Mass

Correlations of outflow force F_{CO} with source properties have long been investigated, e.g., with bolometric luminosity and envelope mass (Bontemps et al. 1996). We compare the ALMASOP sample with other candidate first hydrostatic cores, very low luminosity objects (VeLLOs), and known young stars. Figure 18(a) shows F_{CO} as a function of L_{bol}. Despite the limiting values in our estimation, we found that the ALMASOP sample is located between the well-known Class 0/I sample and the candidate FHSCs and VeLLOs. Linear fitting to all the young sources provides a correlation:

$$\log(F_{CO}) = (1.01 \pm 0.09)\log(L_{bol}) - (5.72 \pm 0.15). \quad (12)$$

The Spearman statistical test is consistent with the correlation (correlation coefficient 0.81 and p-value $\ll 0.05$). Figure 18(a) contains mostly Class 0 objects, with a few Class I (three from the ALMASOP sample) objects. This slope in Equation (12) is similar to those found in other independent studies of Class 0 samples from Skretas & Kristensen (2022; slope $\sim 1.02 \pm 0.26$) and Bontemps et al. (1996; slope $\sim 0.90 \pm 0.15$).

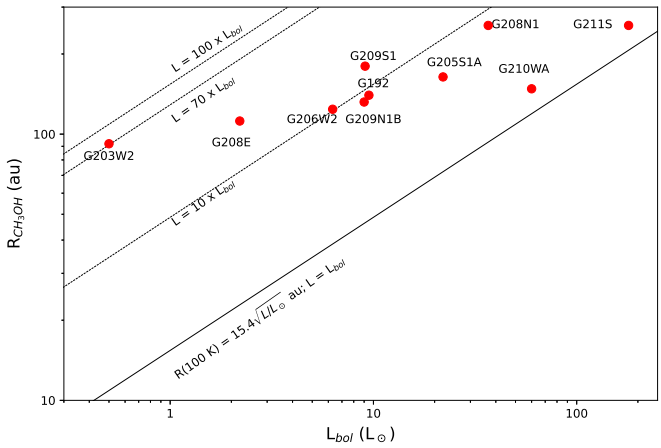

Figure 17. CH_3OH ice lines (R_{CH_3OH}) of the known hot corinos are plotted as a function of bolometric luminosity (L_{bol}). Observed CH_3OH radius and the acronyms of ALMASOP objects are adopted from Hsu et al. (2022). The diagonal lines indicate the ice-line radius at 100 K for luminosity $L_{bol} = 1$, 10, 70, and 100 $L_\odot$.

Figure 18(b) shows the outflow force as a function of envelope mass. A correlation of F_{CO} with M_{env} is seen for all sources, given by the linear fit equation:

$$\log(F_{CO}) = (1.15 \pm 0.71)\log(M_{env}) - (5.50 \pm 0.29). \quad (13)$$

However, the Spearman statistical test suggests a correlation coefficient of 0.33, which is, however, not statistically significant (p-value = 0.16). The slope in Equation (13) is similar to the slopes of Skretas & Kristensen (2022; slope $\sim$0.86) and Bontemps et al. (1996; slope $\sim$1.1). Among four Class I sources ($T_{bol} > 70$ K), three show higher values of F_{CO} than for Class 0 sources of similar M_{env}. Due to the absence of a significant Class I sample, we cannot derive separate correlations for Class 0 and Class I sources. Four multiple sources (three Class 0 and one Class I) exhibit F_{CO} $\sim(0.4\text{–}1.1) \times 10^{-6}\ M_\odot\ \mathrm{km\ s^{-1}\ yr^{-1}}$. We do not observe any special deviation in the F_{CO} of multiple sources from those of single sources.

5. Summary

We have analyzed 42 outflow fields (39 in this study and 3 from the literature) to investigate protostellar outflows and jets with ALMA observations of SiO (5–4), CO (2–1), $C^{18}O$, and 1.3 mm continuum.

(i) Observations of SiO emission mostly trace the dense knots and bow shock regions within jets. SiO emission also traces the shocks in the collision zone between two outflows or between outflows and the ambient cloud. On the other hand, CO emission traces both the outflow shell and the jet component. The CO emission is less optically thick than SiO within the dense knots; therefore, it is expected to reveal deeper structures within the knots than SiO can.

(ii) To understand the morphologies of the various outflow or wind components, we fit simple analytical models assuming a parabolic distribution of the outflow shell and determined inclination angles from the best fits. In general, if CO emission is available on both sides of the velocity axis in the PV diagram, the object is closer to being seen where the disk is edge-on. When the CO emission is well separated on both sides

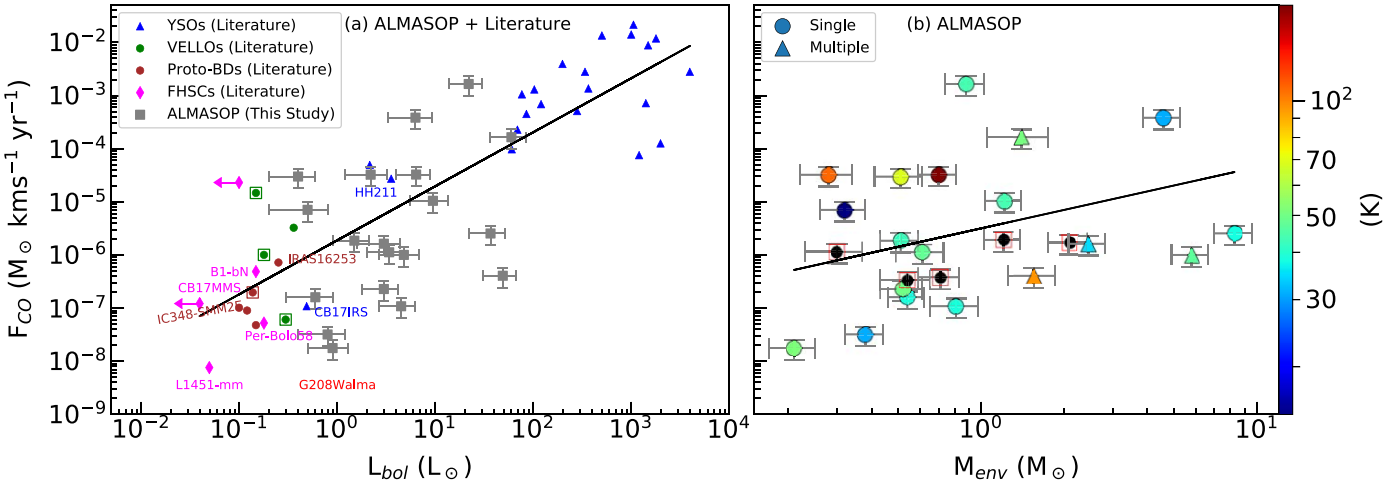

Figure 18. (a) F_{CO} is plotted as a function of L_{bol}. ALMASOP observations are shown with gray squares. Blue, green, brown, and magenta points represent YSOs, VeLLOs, proto−brown dwarfs, and candidate FHSCs, respectively. Proto−brown dwarfs are also in the VeLLO category. These data points have been adopted from Palau et al. (2014), Hsieh et al. (2016), and Dutta et al. (2022a). Open squares indicate single-dish observations. A linear fit of the whole sample (ALMASOP and literature) is shown with the black line. (b) F_{CO} is shown as a function of M_{Env}. The filled circles are single systems. Tringles indicate binary or other multiple systems. Colors are for bolometric temperature (T_{bol}), where those with $T_{bol} > 70$ K are condered as Class I objects. The black filled circles with red open squares do not have a T_{bol} estimation. A linear fit of the data points is also shown.

of the velocity axis, i.e., no emission in the positive velocity quadrant in the blueshifted lobe or vice versa, then the object is closer to being seen where the disk is face-on, or alternatively, the outflow is being viewed pole-on.

(iii) A significant fraction of the jets are observed to be monopolar in SiO emission, with only redshifted components in most cases. We suggest that a specific structure of knots and shocks is responsible for such monopolar jets.

(iv) The comparison of SiO-to-CO abundances in the knots with the model prediction of Tabone et al. (2020) and Glassgold et al. (1991) suggests that jets are possibly dust-poor. For the majority of the jets, Si^+ is possibly coming from the base of the jet or dust sublimation zone, and it combines with the oxygen within the jet to form SiO through a gas-phase reaction. However, the possibility of grain sputtering methods of SiO formation cannot be ruled out completely from the present observations.

(v) From our limited sample, we do not observe any clear correlation between the jet velocities and L_{bol}. However, objects with a lower $\dot{M}_j/\dot{M}_{acc}$ ratio tend to have smaller jet velocities. Furthermore, there is a tentative correlation between the jet velocities and surrounding envelope masses, irrespective of $\dot{M}_j/\dot{M}_{acc}$.

(vi) Mass-loss rates $\dot{M}_j$ do not show any clear correlation with L_{bol}. In most cases, objects of higher luminosity and smaller $\dot{M}_j/\dot{M}_{acc}$ tend to exhibit smaller $\dot{M}_j$. As with jet velocity, $\dot{M}_j$ appears to have some dependence on M_{env}.

(vii) The episode timescales of the knots do not show any clear dependence on L_{bol}. In most cases, however, low-luminosity sources tend to have lower $\dot{M}_j/\dot{M}_{acc}$ and longer periods. Episodes show an apparent anticorrelation with the M_{Env}, which could be due to some underlying mechanism that slows down YSO rotation by the envelope masses.

(viii) Knot timescales are usually more frequent than the freezeout timescales of COMs. Presuming a connection between episodic accretion and ejection events, the episodic ejection may trace the formation history of COMs around the protostar.

(ix) Outflow forces for different types of protostars and candidate FHSCs are correlated with the L_{bol}, along with a tentative correlation with the envelope masses.

More detailed studies are needed with high-resolution and high-sensitivity multiwavelength observations (e.g., in sub-millimeter with ALMA and infrared with JWST) to characterize the ice features and disk–jet connection. Such studies would allow a more precise investigation of the direct/indirect effect of jets on the COMs and planet formation.

Acknowledgments

This paper makes use of the following ALMA data: ADS/JAO. ALMA # 2018.1.00302.S. ALMA is a partnership of ESO (representing its member states), NSF (USA) and NINS (Japan), together with NRC (Canada), NSC and ASIAA (Taiwan), and KASI (Republic of Korea), in cooperation with the Republic of Chile. The Joint ALMA Observatory is operated by ESO, AUI/NRAO and NAOJ. S.D. and C.-F.L. acknowledge grants from the National Science and Technology Council of Taiwan (NSTC 110-2112-M-001-021-MY3 and 112-2112-M-001-039-MY3) and the Academia Sinica (Investigator Award AS-IA-108-M01). D.J. is supported by NRC Canada and by an NSERC Discovery Grant. J.-E.L. was supported by the National Research Foundation of Korea (NRF) grant funded by the Korea government (MSIT; grant number 2021R1A2C1011718). N.H. acknowledges support from the National Science and Technology Council (NSTC) of Taiwan with gtant NSTC 111-2112-M-001-060. K.T. was supported by JSPS KAKENHI (Grant Number JP20H05645). C.W.L. is supported by the Basic Science Research Program through the National Research Foundation of Korea (NRF) funded by the Ministry of Education, Science and Technology (NRF-2019R1A2C1010851), and by the Korea Astronomy and Space Sci- ence Institute grant funded by the Korea government (MSIT; Project No. 2023-1-84000). D.S. acknowledges support from the Ramanujan Fellowship (SERB) and PRL, India. T.L. acknowledges support by the National Key R&D Program of China (No. 2022YFA1603101), the National Natural Science Foundation of China (NSFC) through grant Nos. 12073061 and 12122307, the

international partnership program of the Chinese Academy of Sciences through grant No. 114231KYSB20200009, and Shanghai Pujiang Program 20PJ1415500. M.J. acknowledges support from the Research Council of Finland grant No. 348342. This research was carried out in part at the Jet Propulsion Laboratory, which is operated by the California Institute of Technology under a contract with the National Aeronautics and Space Administration (80NM0018D0004). L.B. gratefully acknowledges support by the ANID BASAL project FB210003.

Facility: ALMA.

Software: Astropy (Astropy Collaboration et al. 2013), APLpy (Robitaille & Bressert 2012), Matplotlib (Hunter 2007), CASA (McMullin et al. 2007).

Appendix A
Inclination Angle from CO Outflow Shell

The molecular CO outflow shell is assumed to be a radially expanding parabolic shell generated by the underlying wide-angle wind. By following the simple analytical model proposed by Lee et al. (2000), the inclination angle (i) of the sources in the plane of the sky can be derived from the physical structure of the wind/outflow shell as observed in CO emission. Figure A1(a) provides a schematic diagram that depicts the integrated outflow emission (here, CO zeroth-moment map). The outflow system lies in the x-y-z plane, which is inclined at an angle i to the plane-of-sky plane, $x'y'z'$. The outflow shells could be expressed in a cylindrical coordinate system:

$$z = cR^2, \tag{14}$$

where R ($=\sqrt{x^2 + y^2}$) denotes the radial distance of the shell from the outflow axis z, and c is the curvature of the parabola near the origin of the outflow or launching zone. The transformations between the two coordinate systems are $x = x'$, $y' = y\cos i + z\sin i$, $z' = z\cos i - y\sin i$. For a radially expanding shell with a velocity proportional to the radial distance, $v_R = R/t_0$, where t_0 is the dynamical time of expansion. In the case of only expansion, the observed velocity ($v_{\rm obs}$) in the sky with a coordinate system (x', z') can be expressed as $y' = -v_{\rm obs}t_0$. By substituting these values into Equation (14), we obtain

$$z'\cos i - v_{\rm obs}t_0\sin i = c[x'^2 + (-v_{\rm obs}t_0\cos i - z'\sin i)^2]. \tag{15}$$

In a narrow PV cut along the jet axis, y' (velocity) and z' (position) become the variables, and the emission along x' (or x) is essentially zero. The schematic diagram in Figure A1(b) displays a PV diagram with an outflow shell and jet (knots). Under these conditions, Equation (15) simplifies to

$$z'\cos i - v_{\rm obs}t_0\sin i = c[(-v_{\rm obs}t_0\cos i - z'\sin i)^2]. \tag{16}$$

The curvature c is determined from fitting to the integrated emission (zeroth-moment) maps (see Equation (14)). By varying i and t_0, we can obtain a parabolic fit of the PV diagram.

For the observed set of velocity (v') and distance along the flow axis (l') the inclination correction terms are $v = v'/\sin i$, $l = l'/\cos i$.

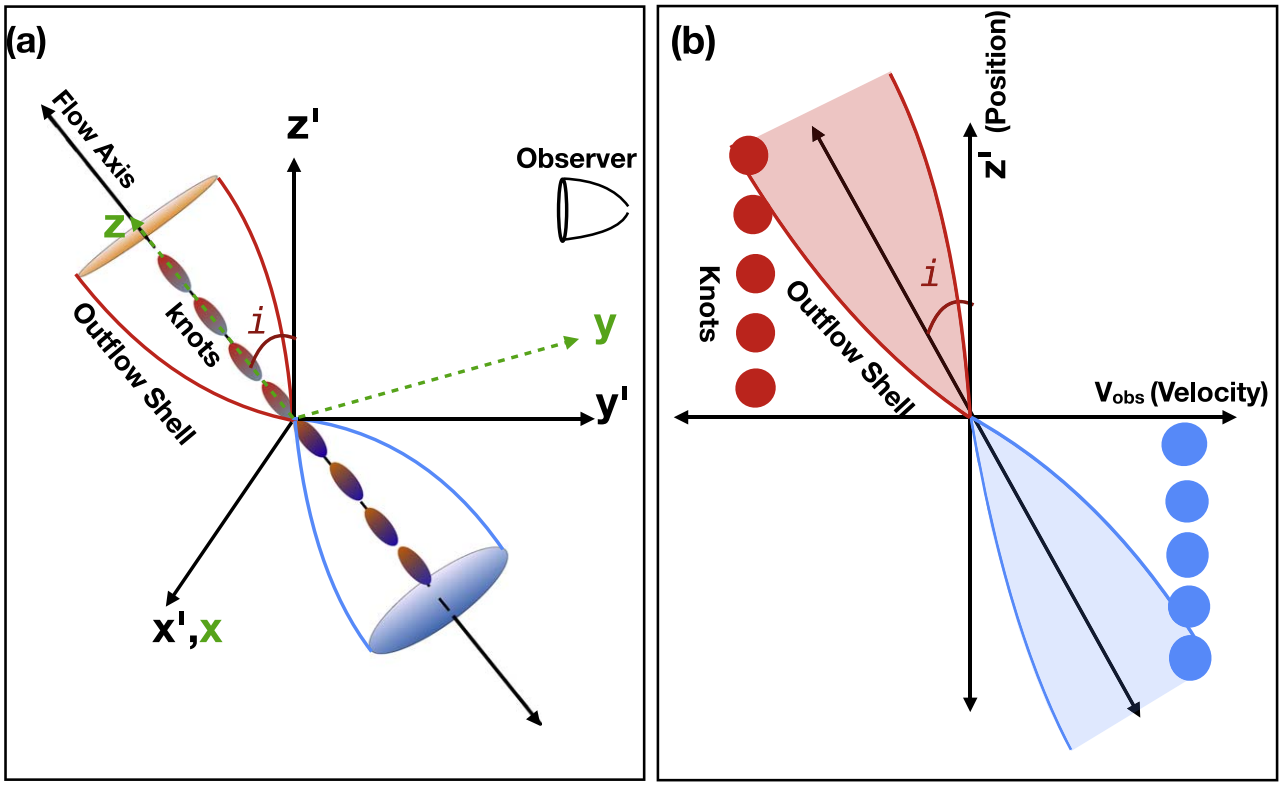

Figure A1. (a) Schematic diagram of the outflow–jet system. The system lies in the x-y-z plane, which is inclined at an angle i to the plane-of-sky plane, $x'y'z'$. The blue color indicates the blueshifted lobe, and the red color indicates the redshifted lobe. (b) PV diagram along the flow axis of panel (a). The blueshifted outflow shell and knots are depicted in blue, while the redshifted outflow shell and knots are depicted in red. The system is inclined at an angle i along the z' position axis. The typical velocities of the knots are represented by red and blue circular patches. These assume that all knots are equidistant and have equal velocities in one case study.

Appendix B
Objects with Confirmed Molecular Jet

B.1. G191.90-11.20S

Figure B1 presents the low-resolution ACA 1.33 mm continuum map (panel (a)), high-resolution $C^{18}O$ spectra (panel (b)), CO map integrated over the whole velocity dispersion (panel (c)), PV of CO along the flow axis (panel (d)), SiO map integrated over the whole velocity dispersion (panel (e)), and SiO PV diagram cut along the flow axis of G191.90-11.20S. The observed object is a Class 0–I transition protostar with $T_{\rm bol} \sim 69 \pm 17$ K and $L_{\rm bol} \sim 0.4 \pm 0.2\ L_{\odot}$. It has an envelope mass of $\sim 0.51 \pm 0.1\ M_{\odot}$.

The protostar drives a CO outflow with a well-defined cavity wall and dense jet along the flow axis detected with both SiO and CO. The source is nearly edge-on ($i\ \sim 5^{+3}_{-4}$ deg). The velocity dispersion of CO emission and SiO emission is nearly identical. A mean jet velocity $V_j = 6 \pm 3$ km s^{-1} was observed. Due to the edge-on orientation, the jet velocity appears small. The nearest knot at the redshifted lobe ($R1$) is faint. The brightest knot at $R2$ resembles a bow shock kind of structure. The other two redshifted knots ($R3$ and $R4$) do not show a dense structure, but closer inspection of the SiO PV diagram confirms the presence of separate knots. The SiO emission is primarily observed in the redshifted lobe. Only one faint SiO knot (B1) was detected in the blueshifted lobe positioned 10″–12″ (∼4000–4800 au) away from the central source. The mean episodic intervals were estimated to be $\mathcal{T}_{\rm knot} \sim 100^{+61}_{-80}$ yr, corresponding to a Keplerian radius in the range ∼3.0–20 au (including estimated error) for a mass range of 0.05–0.30 $M_{\odot}$, respectively. Therefore, the instabilities causing episodic accretion and ejection possibly originated in the disk or its outskirts. The objects exhibit a very high $\dot{M}_j/\dot{M}_{\rm acc}$ ratio of ∼2.1, indicating that it is a highly active ejection/accretion object.

B.2. G205.46-14.56M1 (HOPS 317)

The observations of the continuum, $C^{18}O$, CO, and SiO emissions for G205.46−14.56M1 are shown in Figure B2, following the same order as in Figure B1. The system comprises two sources, A and B, separated by ∼6.″14 (∼2460 au). Source A aligns with the position of HOPS 317 (Tobin et al. 2020), a Class 0 object with $T_{\rm bol} \sim 47 \pm 12$ K, $L_{\rm bol} \sim 4.8 \pm 2.1\ L_{\odot}$. This binary system possesses a combined envelope mass $M_{\rm env} \sim 5.77 \pm 0.88\ M_{\odot}$. G205.46-14.56M1_B, brighter in 1.3 mm continuum, is located at the envelope's center.

Source G205.46-14.56M1_A exhibits a small northeast outflow lobe, with the southwestern lobe potentially blended with the outflow from G205.46-14.56M1_B. However, from our current velocity resolution, we were unable to confirm the presence of an outflow from G205.46-14.56M1_B or discern between the outflow components of the sources. The presence of episodic shells in the blueshifted lobe, similar to the episodic wide-angle outflow of HH 46/47 (Zhang et al. 2019), is a possibility. When calculating $F_{\rm CO}$ from the southwest lobe of G205.46-14.56M1_A, we consider all the observed CO emissions from the lobe. The southern component (blueshifted lobe) of the source G205.46-14.56M1_A reveals a single SiO knot ($B1$), which is corroborated by CO emission. A CO knot-like structure ($R1$?) is visible in the redshifted lobe, although it is undetected in SiO emission. The mean jet velocity derived from peak SiO emission is $V_j \sim 88 \pm 10$ km s^{-1}. With an inclination of i $\sim 75^{+5}_{-15}$ deg, the source is closer to face-on orientation. The mean episodic intervals of the nearest knots are approximately $\mathcal{T}_{\rm knot} \sim 100^{+50}_{-53}$ yr, yielding a Keplerian radius of perturbation between ∼4 and 19 au. The objects exhibit significant accretion/ejection phenomena, as indicated by the high $\dot{M}_j/\dot{M}_{\rm acc}$ ratio of ∼0.67.

B.3. G205.46-14.56S1 (HOPS 358)

Various components of the observations of G205.46-14.56S1 are displayed in Figure B3, following the same sequence as in Figure B1. This system comprises a wide binary with a separation of 13.″37 (∼5349 au). Source G205.46-14.56S1_A drives a nearly north–south outflow and jet, while the outflow of G205.46-14.56S1_B is blended with the redshifted lobe (southern lobe) of G205.46-14.56S1_A. In this paper, we discuss the outflow of G205.46-14.56S1_A, which is identified as HOPS 358 in Tobin et al. (2020). It is a Class 0 source with $T_{\rm bol} = 44 \pm 19$, $L_{\rm bol} = 22 \pm 8\ L_{\odot}$, and the envelope mass of G205.46-14.56S1_A is $0.88 \pm 0.14\ M_{\odot}$.

The outflow from G205.46-14.56S1_A demonstrates a narrow inner section and a suddenly widening outflow lobe. The thick envelope likely suppresses the outflow opening near the source, allowing it to abruptly expand beyond the envelope. The CO outflow kinematics suggest that the object is nearly edge-on with an inclination $i\ \sim 1^{+5}_{-0}$ deg. Notably, the source exhibits strong SiO emission in the southern (redshifted) lobe, whereas the northern (blueshifted) lobe only has faint SiO emission near the source, resembling a monopolar SiO jet. Due to edge-on orientation, the observed mean V_j is quite small $\sim 1.4 \pm 4.0$. The error bar indicates that the jet velocity could become negative, implying that the redshifted lobe might transform into a blueshifted one, and due to the edge-on view, the redshifted and blueshifted velocities could be reliably defined. Several knots are detected in the southern part (R1, R2, ... R14). Here it is important to note that knots are identified based on peak emission, and we were unable to determine whether they form part of the forward and backward components of a single bow shock. The average episodic intervals of the knots were estimated to be $\mathcal{T}_{\rm knot} \sim 34^{+170}_{-17}$ yr, which corresponds to a Keplerian radius ranging from ∼2.5 to 23 au (including estimated error, for a mass range of 0.05–0.30 $M_{\odot}$). The objects exhibit intermediate accretion/ejection phenomena ($\dot{M}_j/\dot{M}_{\rm acc} \sim 0.09$).

B.4. G206.12-15.76 (HOPS 400)

Figure B4 shows different components of the G206.12-15.76 system following the same order as Figure B1. This system, HOPS 400 (Karnath et al. 2020; Tobin et al. 2020), is a close binary, although our observed resolution and sensitivity were not sufficient to resolve the two components. It is a Class 0 system with $T_{\rm bol} = 35 \pm 9$ K and $L_{\rm bol} = 3.0 \pm 1.4\ L_{\odot}$. The combined envelope mass was estimated at $M_{\rm env} \sim 2.44 \pm 0.37\ M_{\odot}$.

The length of the CO outflow is relatively small ($L_{\rm red} \sim 16.''0 \equiv 6400$ au; $L_{\rm blue} \sim 10.''0 \equiv 4000$ au). Both the CO emission and SiO emission have a similar range of velocity dispersion, making it difficult to distinguish outflow shells from jet components. Assuming that low-velocity CO emission is solely a wind/outflow component, we estimated the inclination angle to be $i\ \sim 15^{+15}_{-5}$ deg. Both SiO and CO exhibit high- and low-velocity components. A few knots are identified along the jet axis. From the high-velocity knots, the mean observed jet

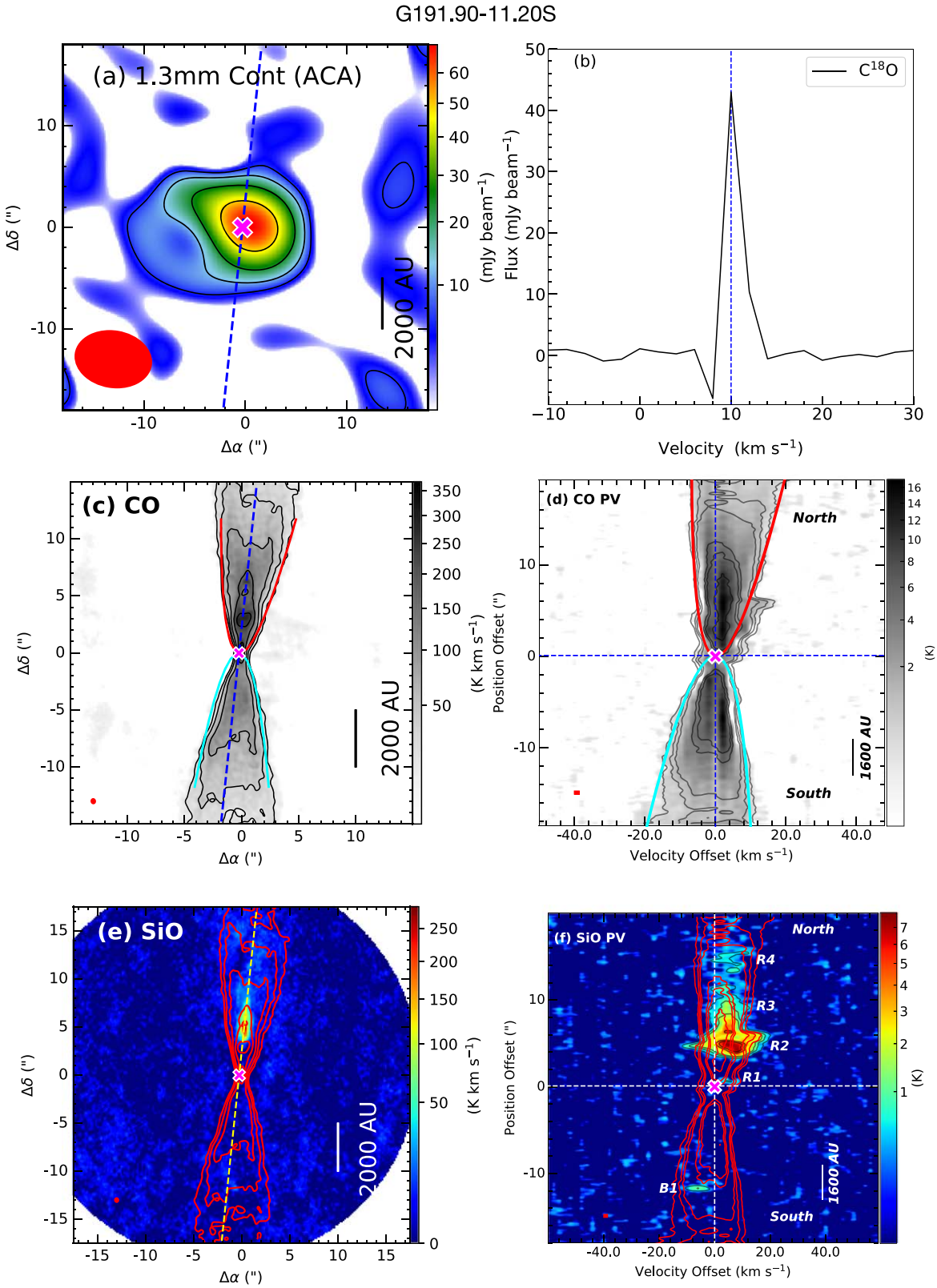

Figure B1. G191.90-11.20S. (a) 1.3 mm continuum map at ACA resolution with sensitivity ∼2.0 mJy beam^{-1}. The symbols and contour levels are the same as in Figure 1. (b) The $C^{18}O$ spectra are extracted from high-resolution maps, and $V_{sys} = 10$ km s^{-1}. All symbols are the same as in Figure 3. (c) CO emission integrated over −4 to +8 km s^{-1} with sensitivity 6.48 K km s^{-1}, with similar symbols and contours to those in Figure 4(a). (d) CO PV diagram with sensitivity 0.16 K, with similar symbols and contours to those in Figure 4(b). (e) SiO emission integrated over −10 to +18 km s^{-1} with sensitivity 3.7 K km s^{-1}, with similar symbols and contours to those in Figures 6 and 5(a). (f) SiO PV diagram with sensitivity 0.16 K, with similar symbols and contours to those in Figure 5(b).

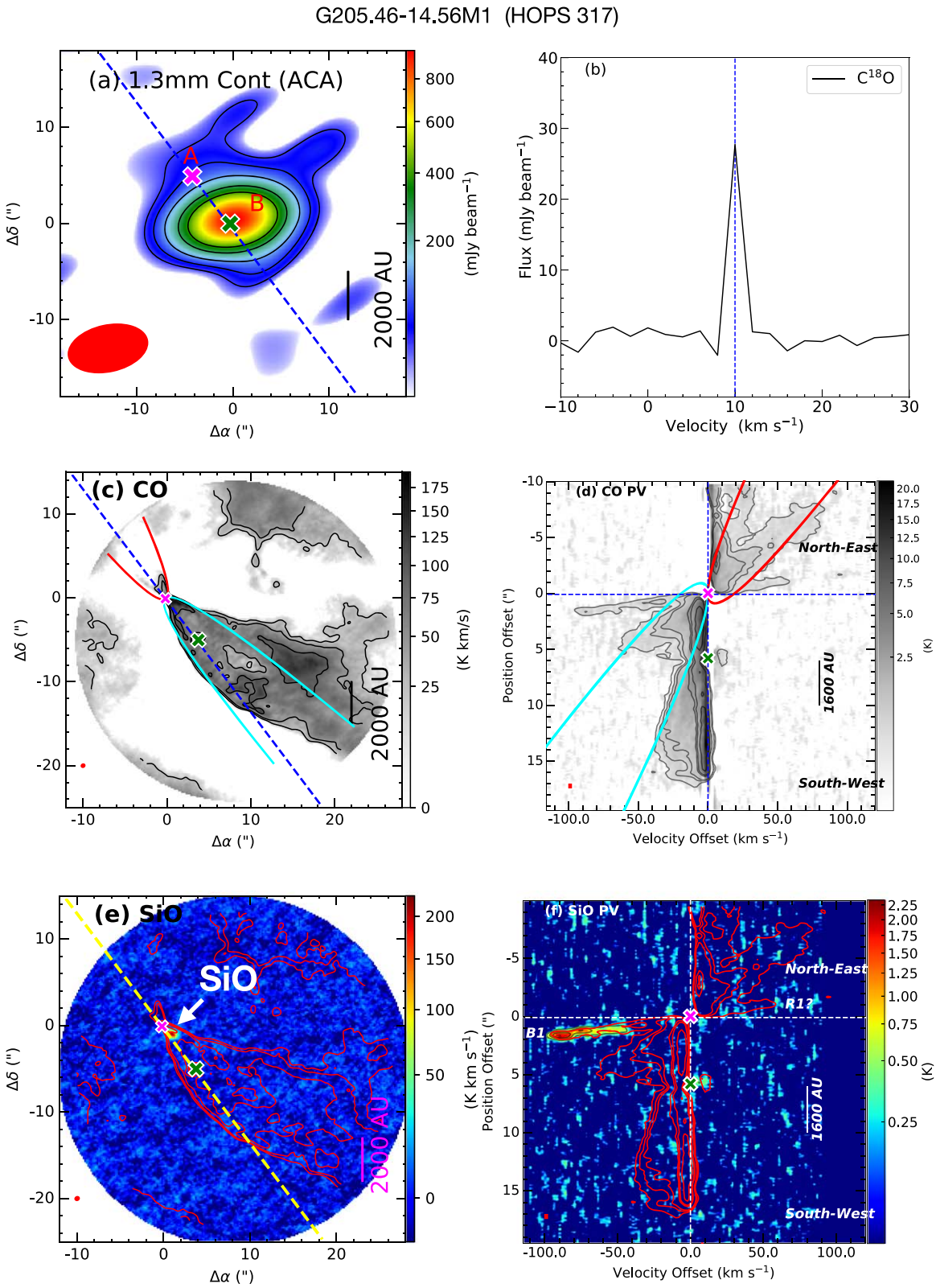

Figure B2. G205.46-14.56M1 (HOPS 317). (a) 1.3 mm continuum map at ACA resolution with sensitivity ∼2.0 mJy beam^{-1}. The symbols and contour levels are the same as in Figure 1. (b) The C^{18}O spectra are extracted from high-resolution maps, and V_{sys} = 10 km s^{-1}. All symbols are the same as in Figure 3. (c) CO emission maps integrated over −18 to −2 km s^{-1} and +2–12 km s^{-1} with sensitivity 7.4 K km s^{-1}, with similar symbols and contours to those in Figure 4(a). (d) CO PV diagram with sensitivity 0.11 K, with similar symbols and contours to those in Figure 4(b). (e) SiO emission integrated over −102 to −28] km s^{-1} and +4–12 km s^{-1} with sensitivity 3.7 K km s^{-1}, with similar symbols and contours to those in Figure 5(a). (f) SiO PV diagram with sensitivity 0.16 K, with similar symbols and contours to those in Figure 5(b). The "?" mark indicates that the present observations could not confirm the candidacy of the knot.

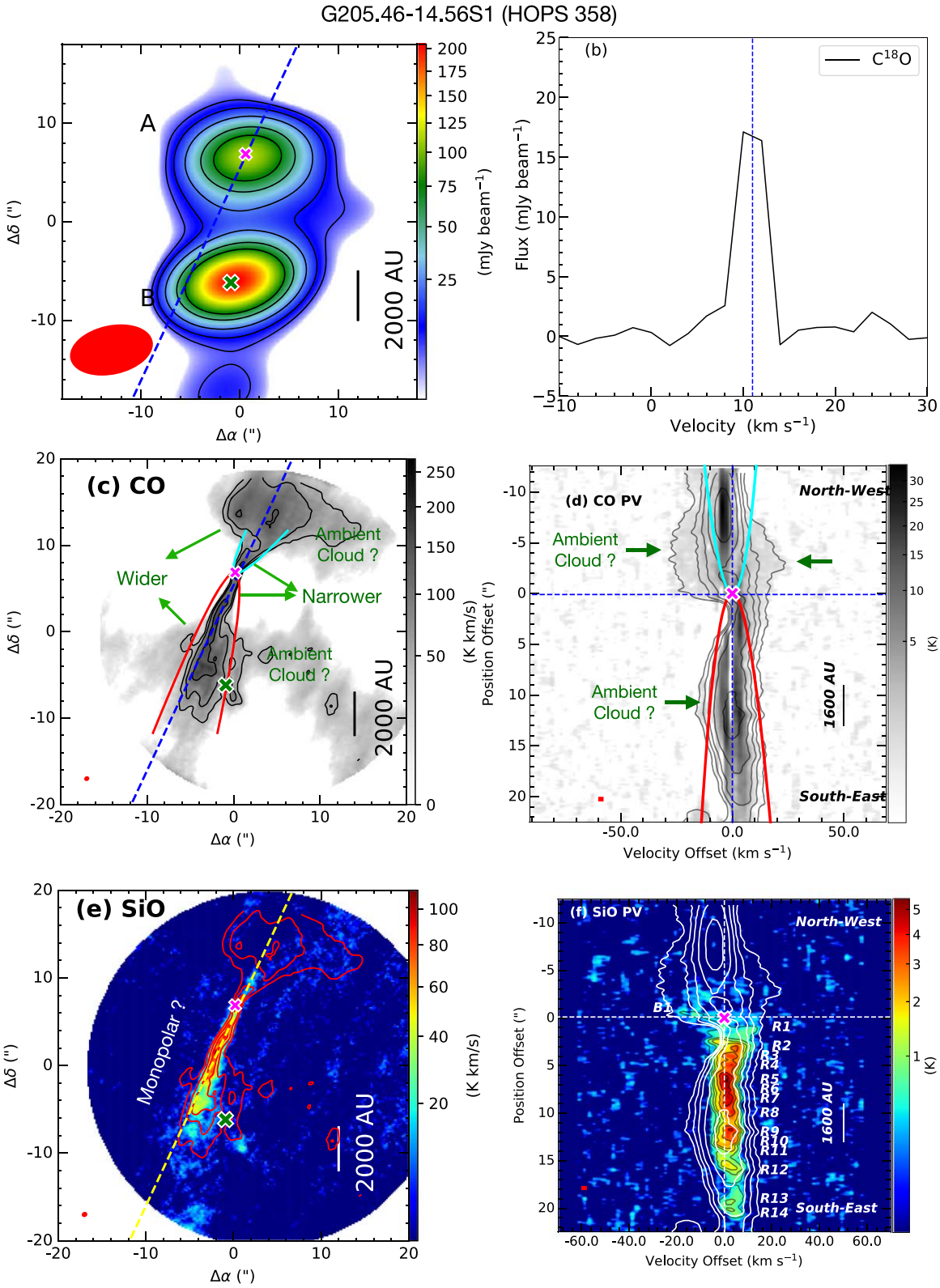

Figure B3. G205.46-14.56S1 (HOPS 358). (a) 1.3 mm continuum map at ACA resolution with sensitivity ∼2.0 mJy beam^{-1}. The symbols and contour levels are the same as in Figure 1. (b) The C^{18}O spectra are extracted from high-resolution maps, and V_{sys} = 11 km s^{-1}. All symbols are the same as in Figure 3. (c) CO emission integrated over −20 to −4 km s^{-1} and +2–20 km s^{-1} with sensitivity $\sigma \sim 14.8$ K km s^{-1}, with similar symbols to those in Figure 4(a). The contours are at (3, 9, 18, 36, 72) × σ . (d) CO PV diagram with sensitivity 0.11 K, with similar symbols and contours to those in Figure 4(b). (e) SiO emission integrated over −20 to +20 km s^{-1} with sensitivity 3.4 K km s^{-1}, with similar symbols and contours to those in Figure 5(a). (f) SiO PV diagram with sensitivity 0.14 K, with similar symbols and contours to those in Figure 5(b). The "?" mark indicates that the present observations could not confirm the scenario.

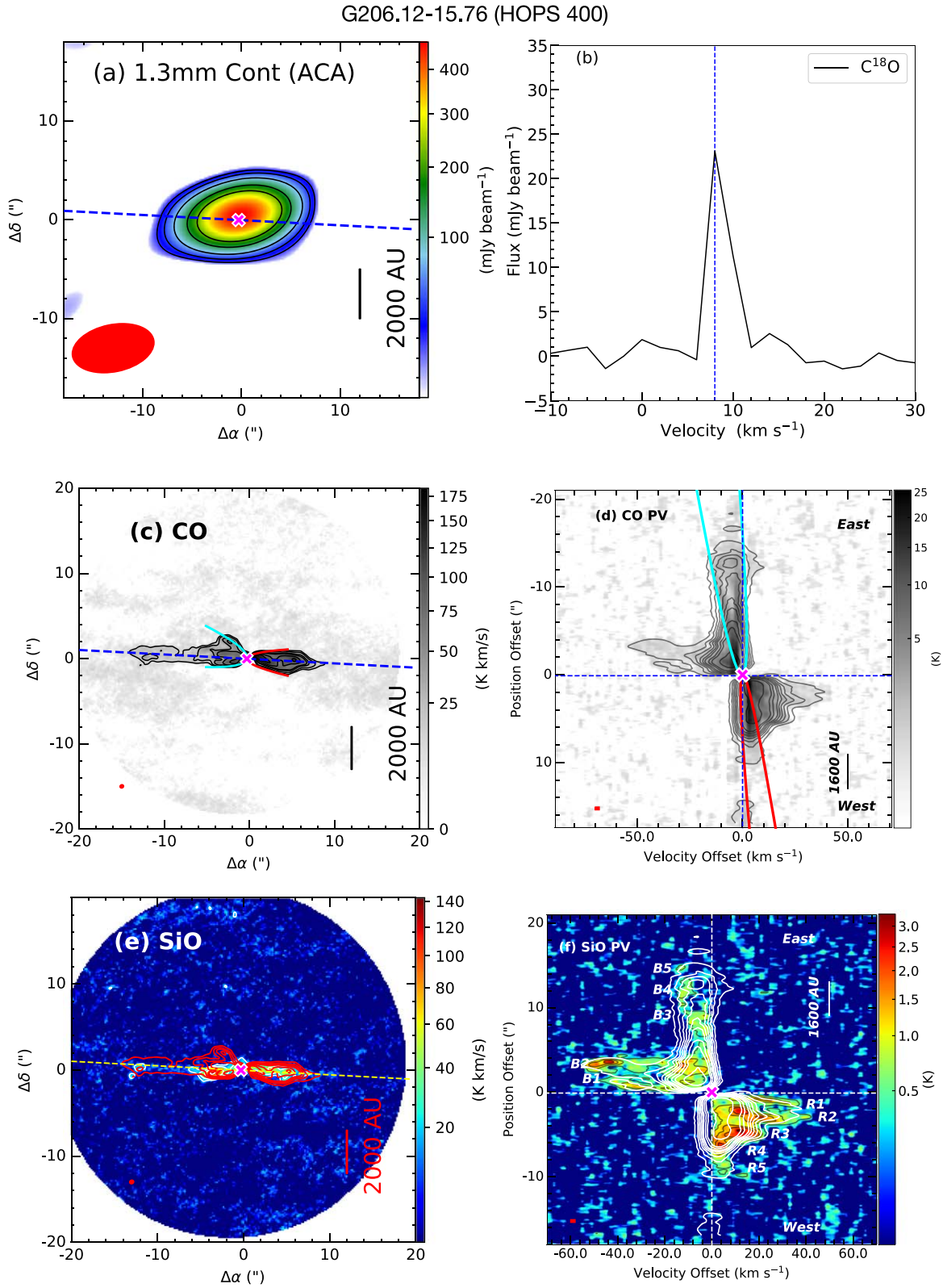

Figure B4. G206.12-15.76. (a) 1.3 mm continuum map at ACA resolution with sensitivity ∼6.0 mJy beam^{-1}. The symbols and contour levels are the same as in Figure 1. (b) The C^{18}O spectra are extracted from high-resolution maps, and $V_{sys} = 8$ km s^{-1}. All symbols are the same as in Figure 3. (c) CO emission integrated over −4 to +8 km s^{-1} with sensitivity $\sigma \sim 4.63$ K km s^{-1}, with similar symbols to those in Figure 4(a). (d) CO PV diagram with sensitivity 0.16 K ,with similar symbols and contours to those in Figure 4(b). (e) SiO emission integrated over −52 to +42 km s^{-1} with sensitivity 4.6 K km s^{-1}, with similar symbols and contours to those in Figure 5(a). (f) SiO PV diagram emission with sensitivity 0.14 K, with similar symbols and contours to those in Figure 5(b).

velocity is estimated as $V_j \sim 40 \pm 15$ km s^{-1}. The mean episodes of the knots are $\mathcal{T}_{\rm knot} \sim 30^{+35}_{-10}$ yr, corresponding to a Keplerian radius of the perturbation zone between 3 and 11 au (including estimated error, for a mass range of 0.05−0.30 $M_\odot$). This object exhibits intermediate ejection phenomena relative to accretion with $\dot{M}_j/\dot{M}_{\rm acc} \sim 0.3$. The object could be at a very young phase of protostellar evolution with a dynamical age of $\mathcal{T}_{\rm DynAge,blue} \sim 203^{+329}_{-70}$ yr for the blueshifted lobe and $\mathcal{T}_{\rm DynAge,red} \sim 127^{+205}_{-44}$ yr for the redshifted lobe (both estimated ages corrected for inclination angle). Thus, we suggest that this system is less than 1000 yr old, as a conservative estimate.

B.5. G208.68-19.20N (HOPS 87)

The details of different observed components are shown in Figure B5, in the same order as Figure B1. This system, HOPS 87 (Furlan et al. 2016; Dutta et al. 2020; Tobin et al. 2020), is a Class 0 system with $T_{\rm bol} = 38 \pm 13$ K and $L_{\rm bol} = 36.7.0 \pm 14.5$ $L_\odot$. The envelope mass was estimated at $M_{\rm env} \sim 8.26 \pm 1.28$ $M_\odot$, which is one of the most massive envelopes in this sample.

The CO emission is blended with the ambient cloud in the eastern part of the object; however, CO emission in the outflow/jet axis is clearly distinguished. The SiO emission clearly detected the outflow/jet emission. The velocity dispersions of SiO and CO are nearly similar. Based on the PV diagrams in CO and SiO, it is difficult to differentiate between wind/outflow and jet components, which leads to a poor fit of the parabola to the CO shell. We assumed that the majority of low-velocity components are likely wind components, leading the inclination angle to be $i \sim 25^{+15}_{-5}$ deg. We estimated the mean of the observed jet velocity to be $V_j \sim 43 \pm 6$ km s^{-1}. There are a few knot-like structures appearing in both the jet lobes, where "B1" and "B2" are possibly blended and not appearing like the bow shock of a single knot, and are not resolved clearly from our data. The system exhibits a high total mass-loss rate of $\dot{M}_j \sim 2.5 \times 10^{-6}$ $M_\odot$ yr^{-1}. The mean ejection episodes were estimated to be $\mathcal{T}_{\rm knot} \sim 19^{+9}_{-4}$ yr. The dynamical age of the blueshifted lobe is $\mathcal{T}_{\rm DynAge,blue} \sim 47^{+38}_{-10}$ yr and $\mathcal{T}_{\rm DynAge,red} \sim 41^{+32}_{-9}$ yr for the redshifted lobe, with both corrected for the measured inclination angle. We suggest that the system is less that 1000 yr old (a conservative timescale). The smaller dynamical age, higher jet mass ejection rate, and presence of an SiO jet indicate that the source is harboring one of the youngest jets known so far.

B.6. G208.68-19.20N3

The details of different observed components are shown in Figure B6 in the same order as Figure B1. There are three sources in the field, suggesting the presence of a multiple system. The source G208.68-19.20N3_A is located ∼16″ away from the close binary system (G208.68-19.20N3_B and G208.68-19.20N3_C). In this paper, we focus on the outflow/jet of G208.68-19.20N3_A. Neither $T_{\rm bol}$ nor $L_{\rm bol}$ for this source is available in the literature. The envelope mass of the object is estimated to be $M_{\rm env} \sim 2.08 \pm 0.34$ $M_\odot$. The locations of G208.68-19.20N3_B and G208.68-19.20N3_C align with HOPS 92. The outflows of this close binary system are blended together and situated on the edge of the PB; thus, we exclude this source from our study.

The velocity dispersions of SiO and CO are nearly identical. Based on the PV diagrams, it is challenging to differentiate between wind/outflow and jet components, leading to a poor fit of the parabola to the CO shell. We assumed that the majority of low-velocity components originate from the wind and are likely wind components. The inclination angle is measured to be $i \sim 35^{+15}_{-15}$ deg. The mean jet velocity is $V_j \sim 35 \pm 15$. There are a few knot-like structures appearing in both the outflow lobes. Although "R1" appears to be double-headed, it does not present itself as a single knot with a bow shock structure in the PV diagrams. The system exhibits a high total mass-loss rate of $\dot{M}_j \sim 1.3 \times 10^{-6}$ $M_\odot$ yr^{-1}. The mean ejection episodes were estimated to be $\mathcal{T}_{\rm knot} \sim 81^{+56}_{-39}$ yr, corresponding to a perturbation zone of Keplerian radius ∼4.5–18 au. The dynamical age of the blueshifted lobe is $\mathcal{T}_{\rm DynAge,blue} \sim 228^{+160}_{-110}$ yr and $\mathcal{T}_{\rm DynAge,red} \sim 190^{+133}_{-91}$ yr for the redshifted lobe, with both adjusted for the inclination angle. We propose that the system is less than 1000 yr old (a conservative estimate). The smaller dynamical age, higher jet mass ejection rate, and presence of an SiO jet indicate that the source is in an extremely young phase of protostellar evolution.

B.7. G208.89-20.04E

The details of continuum and emission components of the G208.89-20.04E system are depicted in Figure B7 and arranged similarly to Figure B1. It is a Class I system having $T_{\rm bol} \sim 108 \pm 25$ K and $L_{\rm bol} \sim 2.2 \pm 1.0$ $L_\odot$. The envelope mass of the source is $M_{\rm env} \sim 0.28 \pm 0.06$ $M_\odot$. The elliptical structure of the inner part of the continuum emission and a small extension along one side (western part) as compared to the other (northeast and eastern part) suggest that this object could be a highly inclined system.

The structure of the CO outflow is complex and irregularly shaped. The redshifted (southwestern) lobe appears wider than the blueshifted (northeastern) lobe. The redshifted lobe is possibly attached to an ambient cloud or outflow of an unknown source. The redshifted lobe is smaller than the blueshifted lobe, but scattered emission is noticeable along the redshifted lobe in both CO and SiO emissions. PV diagrams with CO and SiO indicate that the source is likely nearly edge-on. We measured the inclination angle to be $i \sim 1^{+2}_{-0}$ deg. Due to its edge-on orientation, the blueshifted and redshifted wind/outflow components are difficult to distinguish. Based on the peak emission of CO and SiO, we defined the blue- and redshifted velocity components. We estimated the mean jet velocity to be $V_j \sim 2.0 \pm 2.0$ km s^{-1} (negative error bar leads to zero velocity, indicating a fully edge-on orientation). Different knots are identified from the SiO emission with mean episodes of $\mathcal{T}_{\rm knot} \sim 52^{+104}_{-26}$ yr. The Keplerian radius for a potential perturbation zone is ∼15–70 au, which is a slightly larger range than that of Class 0 sources.

The ALMASOP sample includes two Class I molecular jets with SiO emission along the flow axis. One Class I source, G205.46-14.56S3, was reported with very high velocity SiO emission (Dutta et al. 2022b). Another molecular jet detected with SiO emission is the G208.89-20.04E source. This is a Class I source, or could be in the transition phase from Class 0 to Class I. The jet velocity for this source is very low, potentially due to its edge-on orientation.

B.8. G209.55-19.68S1 (HOPS 11)

The details of different continuum and emission components of G209.55-19.68S1 are illustrated in Figure B8, following the same order as Figure B1. This source coincides with the

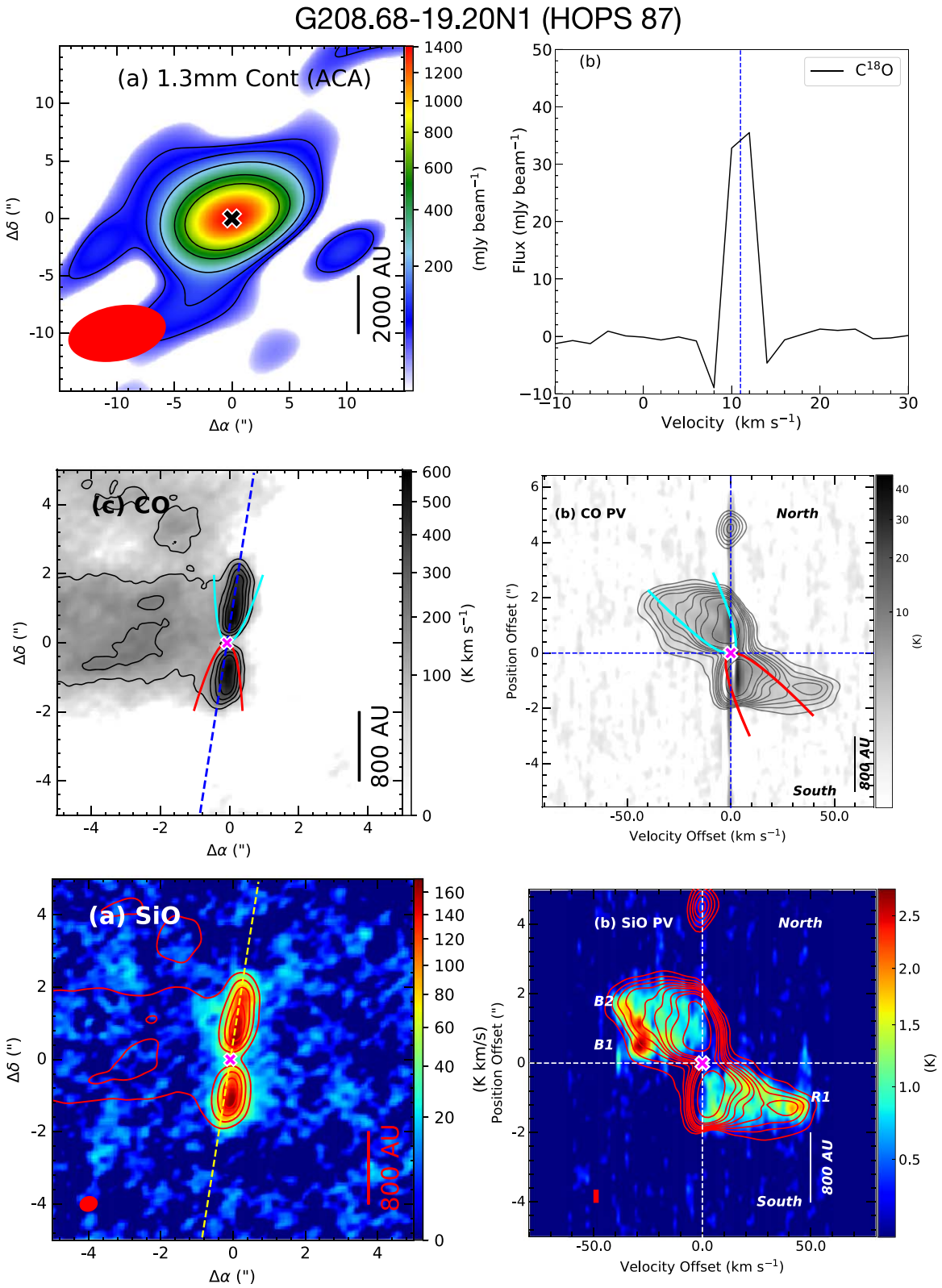

Figure B5. G208.68-19.20N1. (a) 1.3 mm continuum map at ACA resolution with sensitivity ∼18 mJy beam^{-1}. The symbols and contour levels are the same as in Figure 1. (b) The C^{18}O spectra are extracted from high-resolution maps, and $V_{sys} = 11$ km s^{-1}. All symbols are the same as in Figure 3. (c) Integrated CO emission with sensitivity 31.6 K km s^{-1}, with similar symbols to those in Figure 4(a). The contours are at (3, 5) × 31.6 K. (d) CO PV diagram with sensitivity 0.16 K, with similar symbols and contours to those in Figure 4(b). (e) SiO emission integrated over −50 to +50 km s^{-1} with sensitivity 4.6 K km s^{-1}, with similar symbols and contours to those in Figure 5(a). (f) SiO PV diagram emission with sensitivity 0.14 K, with similar symbols and contours to those in Figure 5(b).

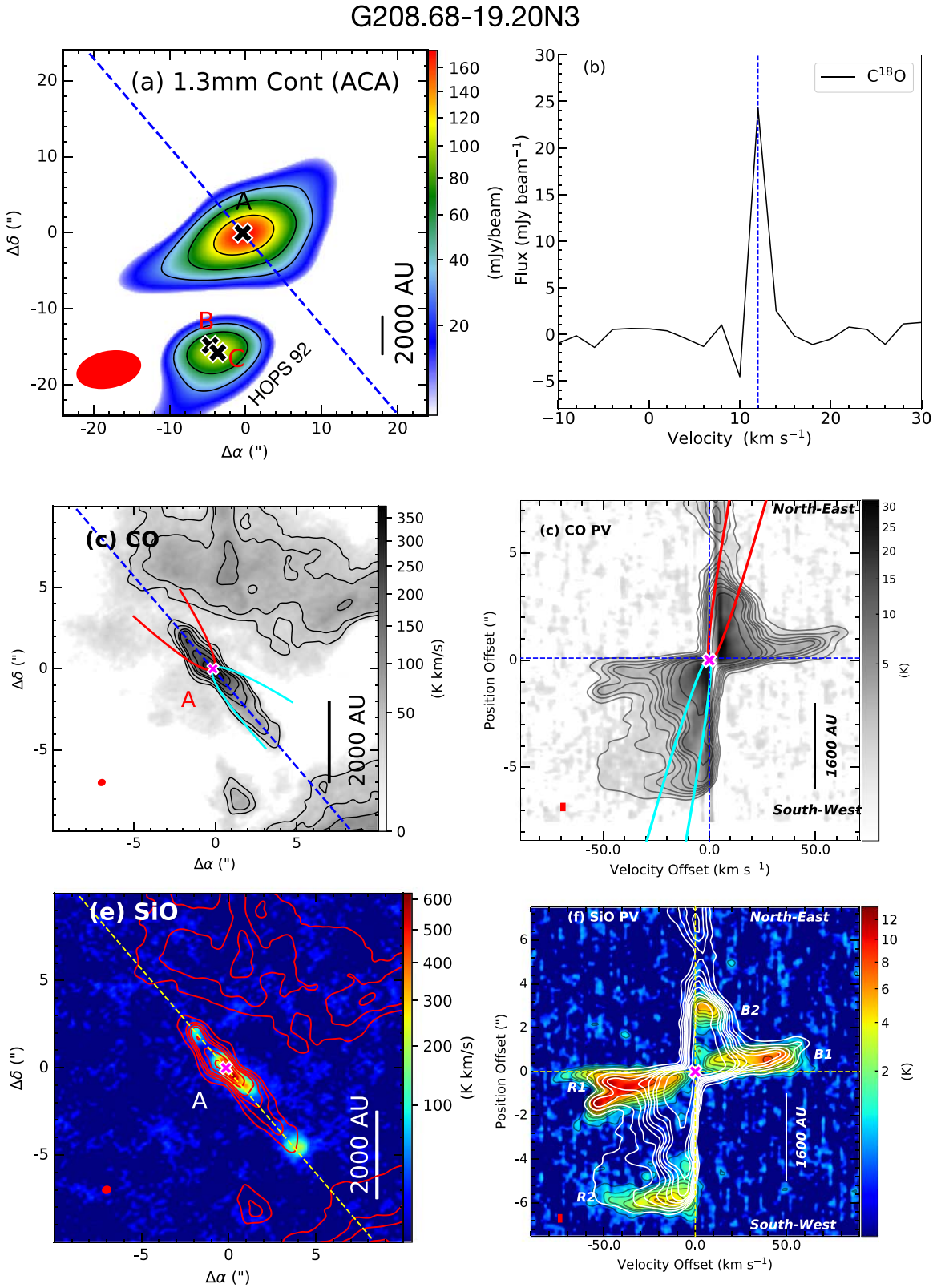

Figure B6. G208.68-19.20N3. (a) 1.3 mm continuum map at ACA resolution with sensitivity ∼10.0 mJy beam^{-1}. The symbols and contour levels are the same as in Figure 1. (b) The C^{18}O spectra are extracted from high-resolution maps, and $V_{sys} = 12$ km s^{-1}. All symbols are the same as in Figure 3. (c) CO emission integrated over −12 to +12 km s^{-1} with sensitivity $\sigma \sim 9.65$ K km s^{-1}, with similar symbols to those in Figure 4(a). (d) CO PV diagram with sensitivity 0.16 K, with similar symbols and contours to those in Figure 4(b). (e) SiO emission inetgrated over −66 to +58 km s^{-1} with sensitivity 4.6 K km s^{-1}, with similar symbols and contours to those in Figure 5. (f) SiO PV diagram with sensitivity 0.15 K, with similar symbols and contours to those in Figure 5(b).

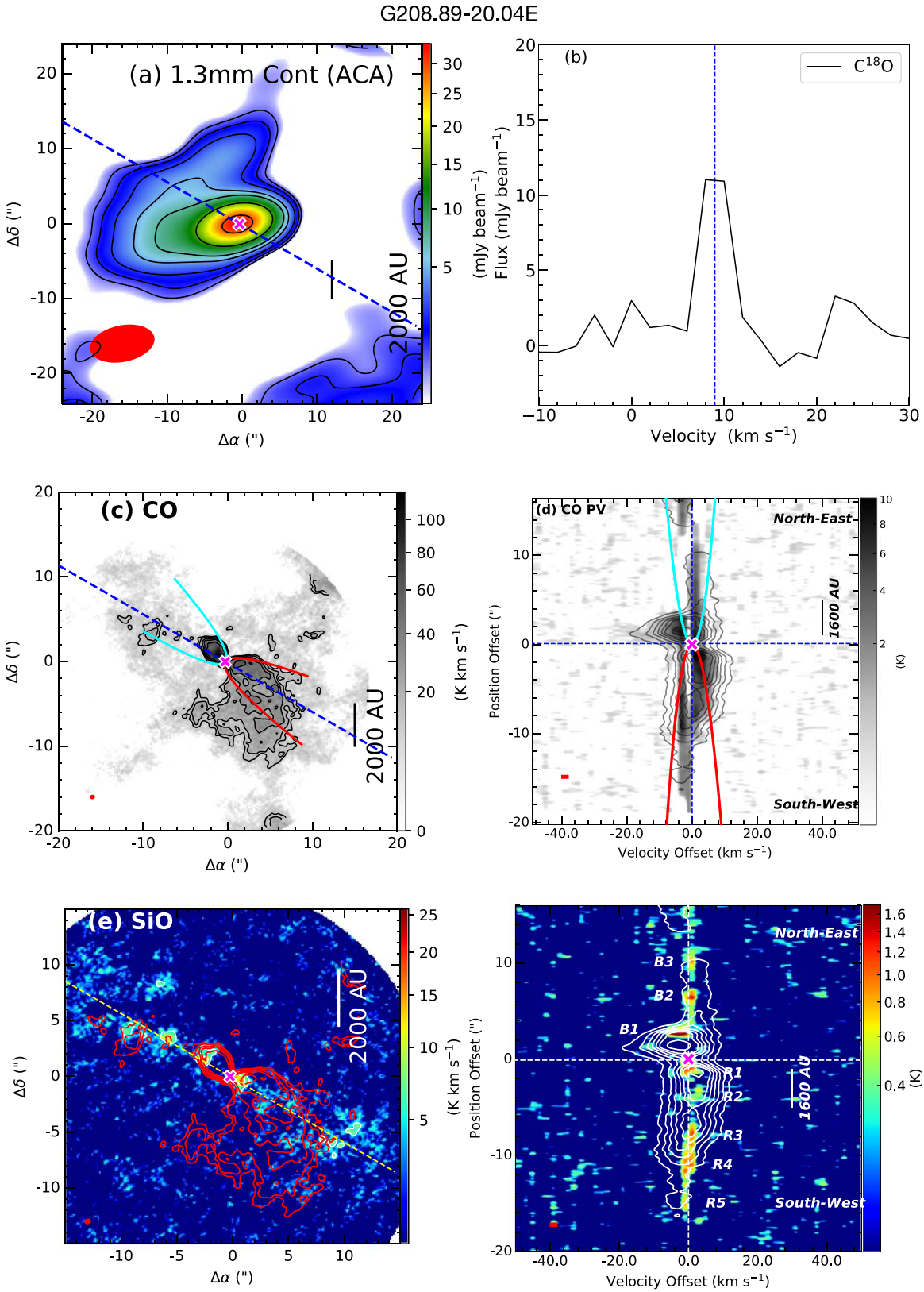

Figure B7. G208.89−20.04E. (a) 1.3 mm continuum map at ACA resolution with sensitivity ∼0.2 mJy beam^{-1}. The symbols and contour levels are the same as in Figure 1. (b) The C^{18}O spectra are extracted from high-resolution maps, and $V_{sys} = 9$ km s^{-1}. All symbols are the same as in Figure 3. (c) CO emission integrated over −4 and +2−6 km s^{-1} with sensitivity $\sigma \sim 1.52$ K km s^{-1}, with similar symbols to those in Figure 4(a). (d) CO PV diagram with sensitivity 0.16 K, with similar symbols and contours to those in Figure 4(b). (e) SiO emission integrated over −4 to +4 km s^{-1} with sensitivity 1.7 K km s^{-1}, with similar symbols and contours to those in Figure 5(a). (f) SiO PV diagram with sensitivity 0.32 K, with similar symbols and contours to those in Figure 5(b).

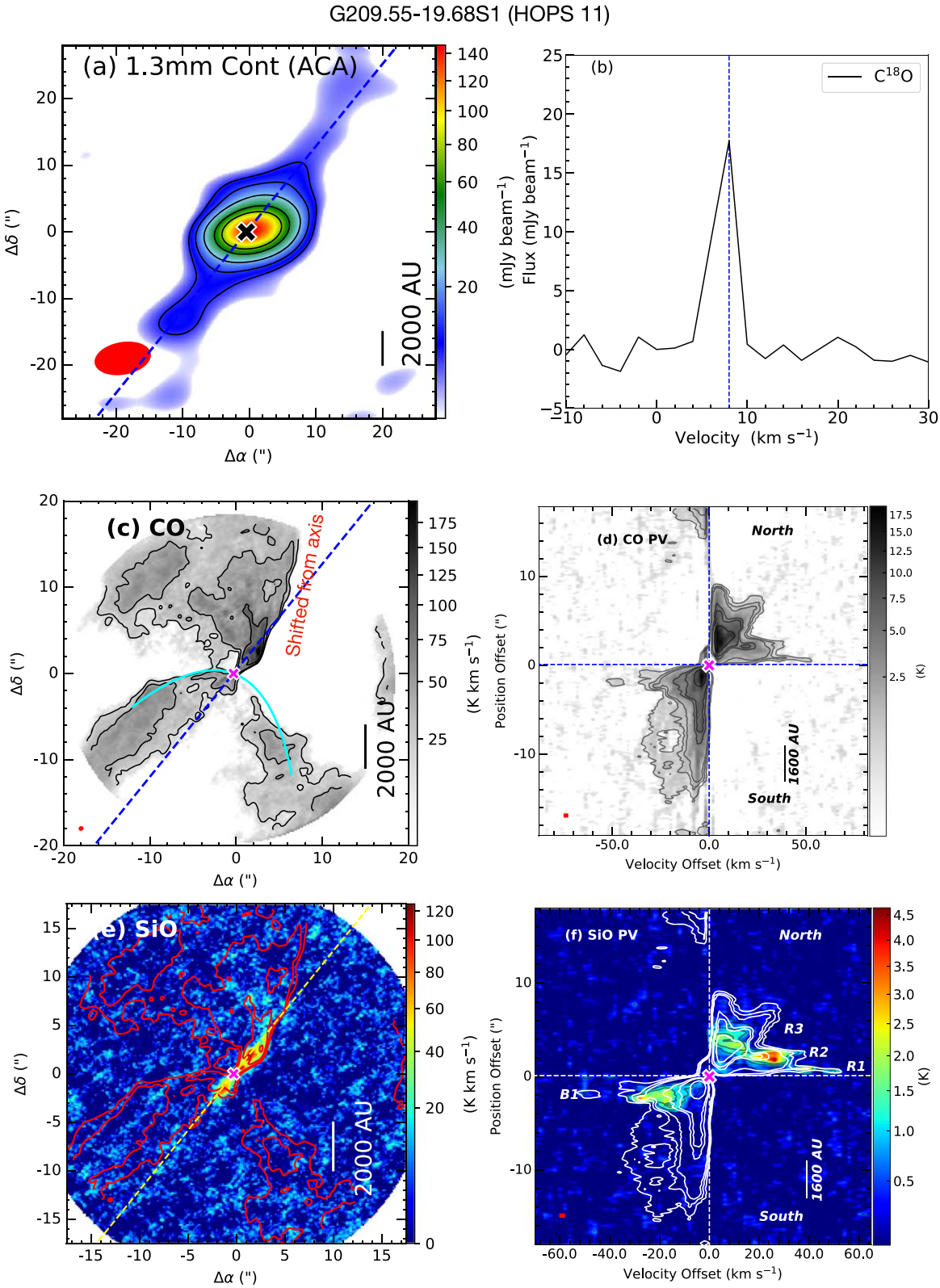

Figure B8. G209.55-19.68S1 (HOPS 11). (a) 1.3 mm continuum map at ACA resolution with sensitivity ∼2.0 mJy beam^{-1}. The symbols and contour levels are the same as in Figure 1. (b) The $C^{18}O$ spectra are extracted from high-resolution maps, and $V_{sys} = 8$ km s^{-1}. All symbols are the same as in Figure 3. (c) CO emission integrated over −8 to −4 km s^{-1} and +4−8 km s^{-1} with sensitivity $\sigma \sim 6.6$ K km s^{-1}, with similar symbols to those in Figure 4(a). (d) CO PV diagram with sensitivity 0.16 K, with similar symbols and contours to those in Figure 4(b). (e) SiO emission integrated over −60 to +60 km s^{-1} with sensitivity 8.0 K km s^{-1}, with similar symbols and contours to those in Figure 5(a). (f) SiO PV diagram with sensitivity 0.15 K, with similar symbols and contours to those in Figure 5(b).

HOPS 11 source (Tobin et al. 2020) and has $T_{\rm bol} \sim 50 \pm 15$ K and $L_{\rm bol} \sim 9.1 \pm 3.6\ L_{\odot}$. The mass of the envelope is estimated to be $M_{\rm env} \sim 1.09 \pm 0.17\ M_{\odot}$. The 1.33 mm emission is extended along the outflow direction, potentially implying that there is entrained envelope material along the outflow wall driven by the outflow.

The CO outflow's northern part (redshifted lobe) bends toward the northwest from the flow axis, and the southern outflow CO emission appears very wide. The CO and SiO PV diagrams along the flow axis suggest that the source is not an edge-on object. The outflow shells are challenging to distinguish for this source, so the exact fitting is not shown. A tentative fitting to the blueshifted lobe of the CO outflow shells suggests an inclination angle $i \sim 25^{+15}_{-15}$ deg. A few SiO knots were observed along the flow axis, and the mean jet velocities are estimated to be $V_j \sim 27 \pm 4$ km s^{-1}. Due to the unreliable inclination measurement, this source is not included in the statistical analyses in the main text.

B.9. G209.55-19.68S2 (HOPS 10)

The continuum and different emission components of G209.55-19.68S2 are displayed in Figure B9 in the same order as Figure B1. The object's location coincides with HOPS 10 (Tobin et al. 2020). The source has $T_{\rm bol} \sim 48 \pm 11$ K and $L_{\rm bol} \sim 3.4 \pm 1.4\ L_{\odot}$. The envelope mass is estimated to be $M_{\rm env} \sim 0.61 \pm 0.12\ M_{\odot}$. The peak of the continuum is shifted toward the northeast from the envelope's center. Such continuum emission could be due to an edge-on orientation of the object.

The wind/outflow component in CO emission is well separated from the high-velocity jet component. The object exhibits a redshifted monopolar jet, detectable with both SiO and CO, making it one of the most beautiful high-velocity monopolar jets discovered to date. The inclination angle is measured to be $i \sim 20^{+10}_{-5}$ deg. The observed jet velocity is $V_j \sim 50 \pm 5$ km s^{-1}. Several knots are detected in the redshifted lobe, with ejection episodes estimated to be $\mathcal{T}_{\rm knot} \sim 22^{+13}_{-6}$ yr. This corresponds to a perturbation zone at a Keplerian radius ~2–7 au.

B.10. G210.37-19.53S (HOPS 164)

Figure B10 shows the continuum, $C^{18}O$ spectra, integrated CO and SiO maps, and PV diagrams of G210.37-19.53S in the same order as Figure B1. This source has $T_{\rm bol} \sim 39 \pm 10$ K and $L_{\rm bol} \sim 0.6 \pm 0.3\ L_{\odot}$, making it one of the VeLLOs. The location of this object matches with HOPS 164 (Tobin et al. 2020). The surrounding envelope mass is estimated to be $M_{\rm env} \sim 0.54 \pm 0.08\ M_{\odot}$.

The SiO knots are considered to delineate the jet axis or flow axis. The CO emission is asymmetrically distributed on both sides of the flow axis. We calculated an inclination angle of $i \sim 25^{+10}_{-10}$ deg. Several knots are detected from integrated maps and PV diagrams of SiO and CO, close to the source on both the blueshifted (*R*1, *R*2, *R*3) and redshifted (*B*1, *B*2, *B*3) lobes. Knots *R*1, *R*2, and *R*3 appear to represent different components of the bow shock (forward shock, backward shock) in a single knot from the SiO PV diagram, even though integrated maps do not present a bow-shock-like appearance. Given the present sensitivity and velocity resolution of our observations, it is difficult to determine whether it is really a single knot or three different knots. We estimated a mean velocity of $V_j \sim 36 \pm 5$ km s^{-1}. The mean episode of the ejection events is $\mathcal{T}_{\rm knot} \sim 23^{+18}_{-10}$ yr. The perturbation zone for the episodic accretion could be at a Keplerian radius of ~ 2–8 au. The relatively higher ratio of $\dot{M}_j/\dot{M}_{\rm acc} \sim 0.3$ exhibited by this object indicates that it might be at a relatively younger phase of protostellar evolution.

B.11. G210.49-19.79W (HOPS 168)

Figure B11 shows various components of the continuum and emission in the same order as Figure B1. High-resolution maps (~140 au) reveal two continuum peaks, G210.49-19.79W_A and G210.49-19.79W_B (Dutta et al. 2020). The fainter continuum peak of G210.49-19.79W_B is yet to be confirmed as a protostar. The location of G210.49-19.79W_A coincides with HOPS 168 (Tobin et al. 2020). It has $T_{\rm bol} \sim 51 \pm 20$ K and $L_{\rm bol} \sim 60 \pm 24\ L_{\odot}$. The envelope mass is calculated to be $M_{\rm env} \sim 1.4 \pm 0.35\ M_{\odot}$. The envelope material is possibly entrained by an outflow and extends toward the southwest along the boundary wall of the redshifted outflow. The inclination angle is measured to be $i \sim 5^{+5}_{-4}$ deg from the outermost CO shell.

A close look at the CO emission near the source suggests a twisted CO shell at its base. The SiO emission does not align along a particular axis (as marked in the SiO integrated map). One SiO knot is observed in the northeast of the jet axis in the blueshifted lobe. In the redshifted lobe, one SiO knot close to the source appears to be shifted to the southwest. All SiO knots form an S-shaped structure, possibly due to wiggling of the jet. Similar wiggling structures have also been reported in molecular jets from other protostars, such as HH 211 (Lee et al. 2010; Moraghan et al. 2016). We measure the mean jet velocity $V_j \sim 5 \pm 4$ km s^{-1} ($V_{j,\rm cor} \sim V_j/\sin i$). This small velocity range is not in agreement with the SiO emission in the jet if we consider a dust sputtering scenario. SiO emission is plausible if it originates at the dust sublimation zone. Otherwise, there could be an undetected close binary with two jets originating at two different position angles.

Another possible explanation could be the scenario of episodic CO shells and SiO knots launched at different times, as in the case of the episodic wide-angle outflow in HH 46/47 (Zhang et al. 2019). The CO PV diagram in Figures B11(d) and (f) also hints at such episodic shell occurrences (marked with thicker blue and red curves in the CO PV diagram). Now consider a cloud core contracting along the magnetic field lines toward the midplane (equatorial plane) and forming a flattened envelope or pseudodisk. In this scenario, the flattened envelope is warped because of the contraction direction of the cloud core, and thus the minor axis of the flattened envelope is changed gradually from parallel to the magnetic field axis in the outer region to parallel to the rotation axis in the inner region (Lee et al. 2019a; Hirano & Machida 2019). Therefore, the position angle of the jet axis is also expected to be rotated according to the rotation direction of the disk. The SiO jet could be launched at different orientations of the jet at different timescales. Then, the inclination angle measured above could not be a true value from a single outermost CO shell, but rather a combination of multiple episodic shells. The orientation (i) of those shells could be much smaller (toward edge-on) than estimated above. We recommend further investigation of this source with higher angular resolution, higher velocity resolution, and higher-sensitivity observations to better understand its true nature.

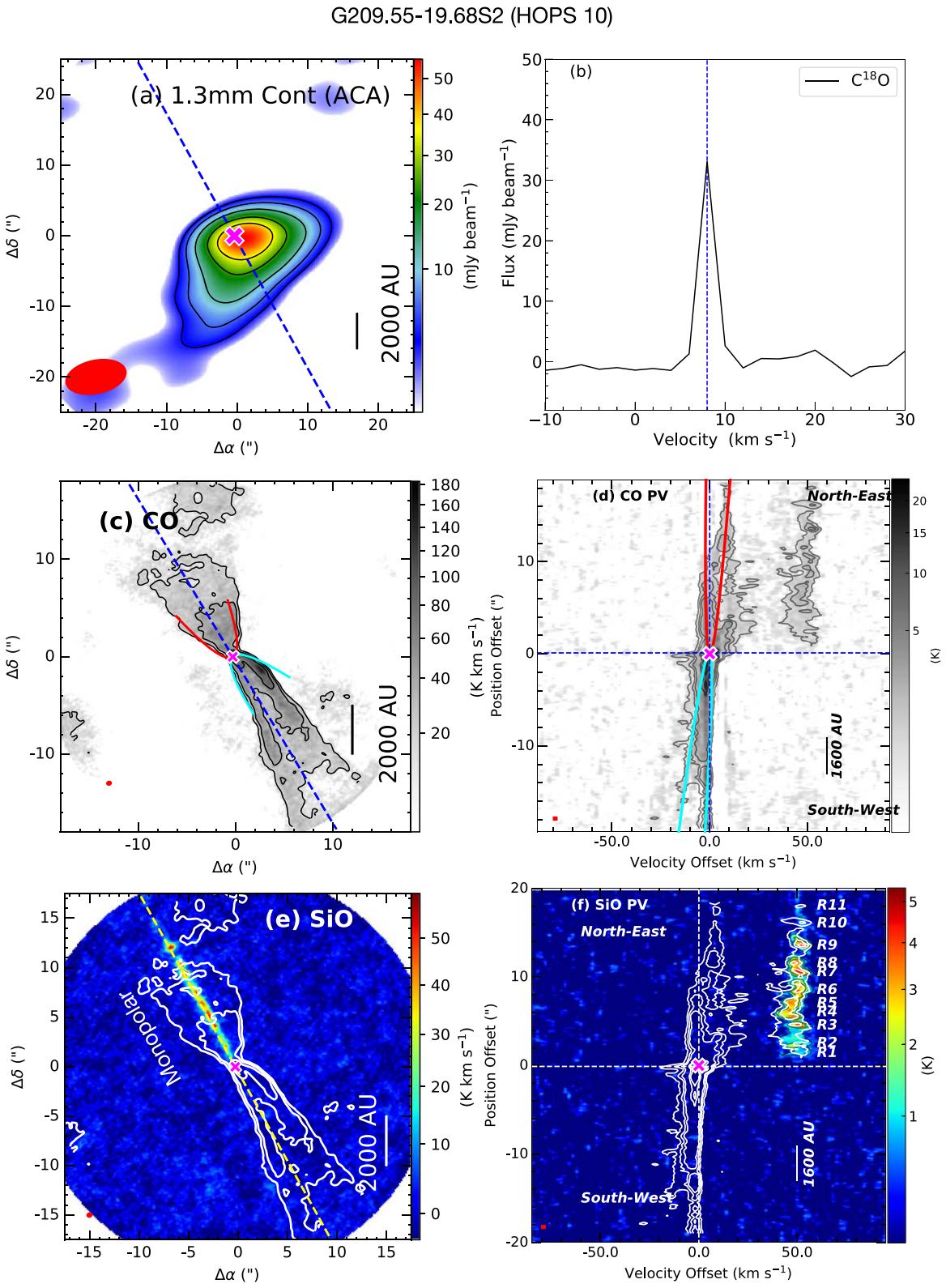

Figure B9. G209.55-19.68S2 (HOPS 10). (a) 1.3 mm continuum map at ACA resolution with sensitivity ∼1.0 mJy beam^{-1}. The symbols and contour levels are the same as in Figure 1. (b) The C^{18}O spectra are extracted from high-resolution maps, and $V_{sys} = 8$ km s^{-1}. All symbols are the same as in Figure 3. (c) CO emission integrated over −4 to −2 km s^{-1} and +2−4 km s^{-1} with sensitivity $\sigma \sim 5.8$ K km s^{-1}, with similar symbols to those in Figure 4(a). (d) CO PV diagram with sensitivity 0.21 K, with similar symbols and contours to those in Figure 4(b). (e) SiO emission integrated over +40−58 km s^{-1} with sensitivity 2.5 K km s^{-1}, with similar symbols and contours to those in Figure 5(a). (f) SiO PV diagram with sensitivity 0.21 K, with similar symbols and contours to those in Figure 5(b).

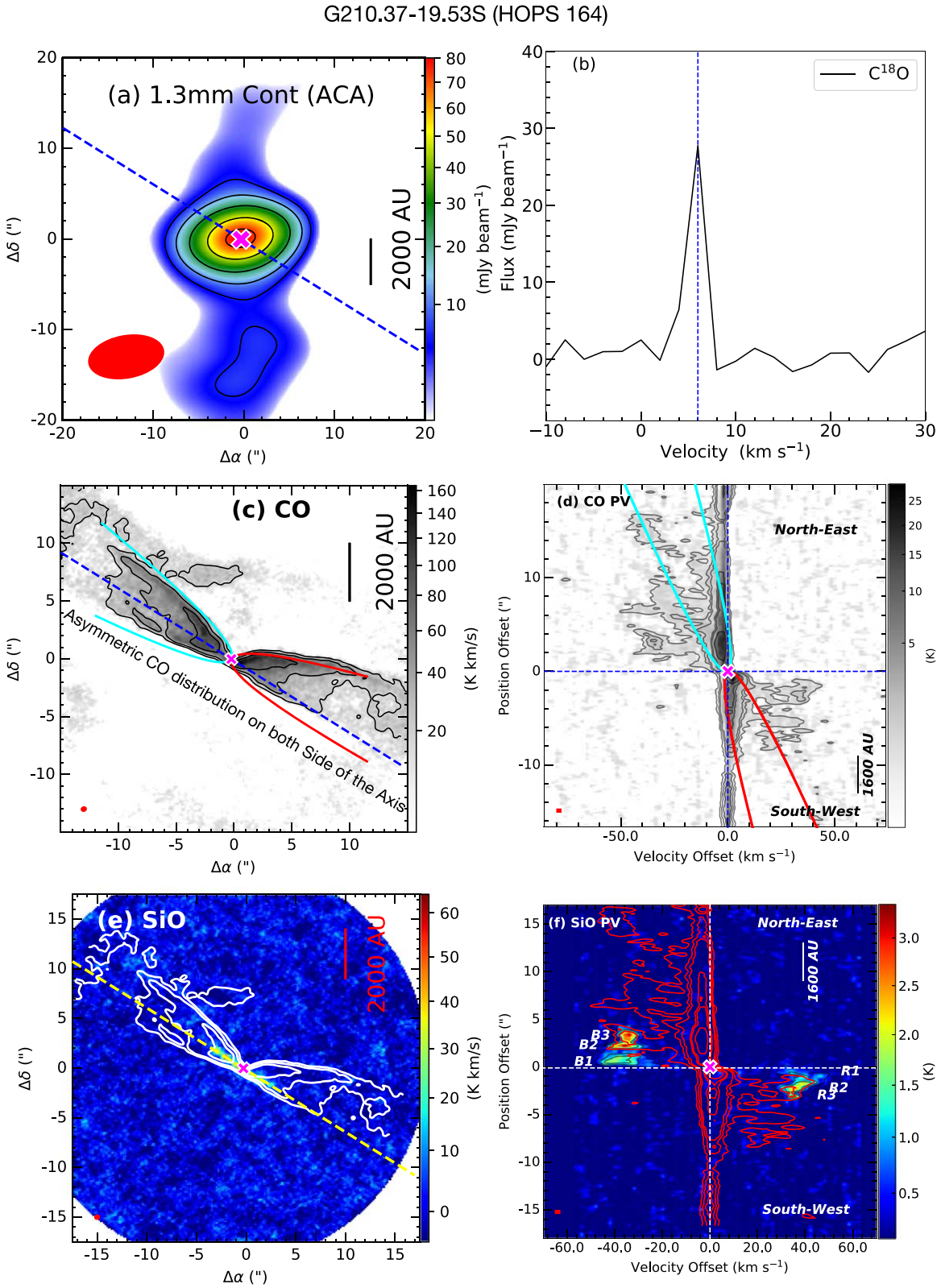

Figure B10. G210.37-19.53S (HOPS 164). (a) 1.3 mm continuum map at ACA resolution with sensitivity ∼1.0 mJy beam^{-1}. The symbols and contour levels are the same as in Figure 1. (b) The C^{18}O spectra are extracted from high-resolution maps, and $V_{sys} = 8$ km s^{-1}. All symbols are the same as in Figure 3. (c) CO emission integrated over −6 to −2 km s^{-1} and 0−4 km s^{-1} with sensitivity $\sigma \sim 5.8$ K km s^{-1}, with similar symbols to those in Figure 4(a). (d) CO PV diagram with sensitivity 0.21 K, with similar symbols and contours to those in Figure 4(b). (e) SiO emission integrated over −46 to −24 km s^{-1} and +30−48 km s^{-1} with sensitivity 2.5 K km s^{-1}, with similar symbols and contours to those in Figure 5(a). (f) SiO PV diagram with sensitivity 0.21 K, with similar symbols and contours to those in Figure 5(b).

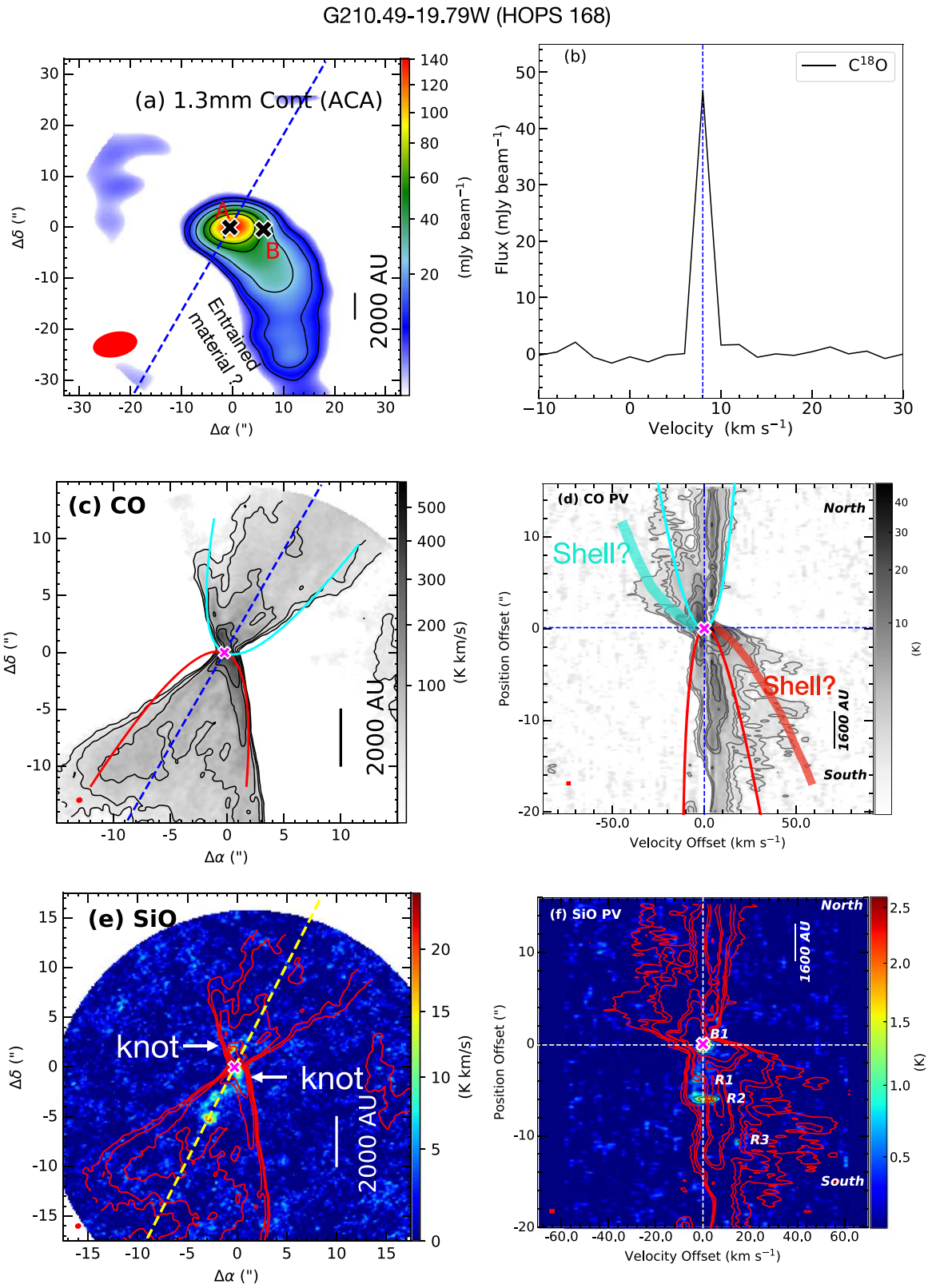

Figure B11. G210.49-19.79W (HOPS 168). (a) 1.3 mm continuum map at ACA resolution with sensitivity ∼2.0 mJy beam^{-1}. The symbols and contour levels are the same as in Figure 1. (b) The C^{18}O spectra are extracted from high-resolution maps, and $V_{sys} = 7$ km s^{-1}. All symbols are the same as in Figure 3. (c) CO emission map integrated over −45 to +55 km s^{-1} with sensitivity 6.0 K km s^{-1}, with similar symbols and contours to those in Figure 4(a). (d) CO PV diagram with sensitivity 0.15 K, with similar symbols and contours to those in Figure 4(b). The additional likely episodic shells are marked with thick blue and red lines in the blueshifted and redshifted lones, respectively. (e) SiO map integrated over −20 to +20 km s^{-1} with sensitivity 1.9 K km s^{-1}, with similar symbols and contours to those in Figure 5(a). The knots shifted from jet axis are marked. (f) SiO PV diagram with sensitivity $\sigma = 0.15$ K, with similar symbols to those in Figure 5(b). The "?" mark indicates that the present observations could not confirm the scenario.

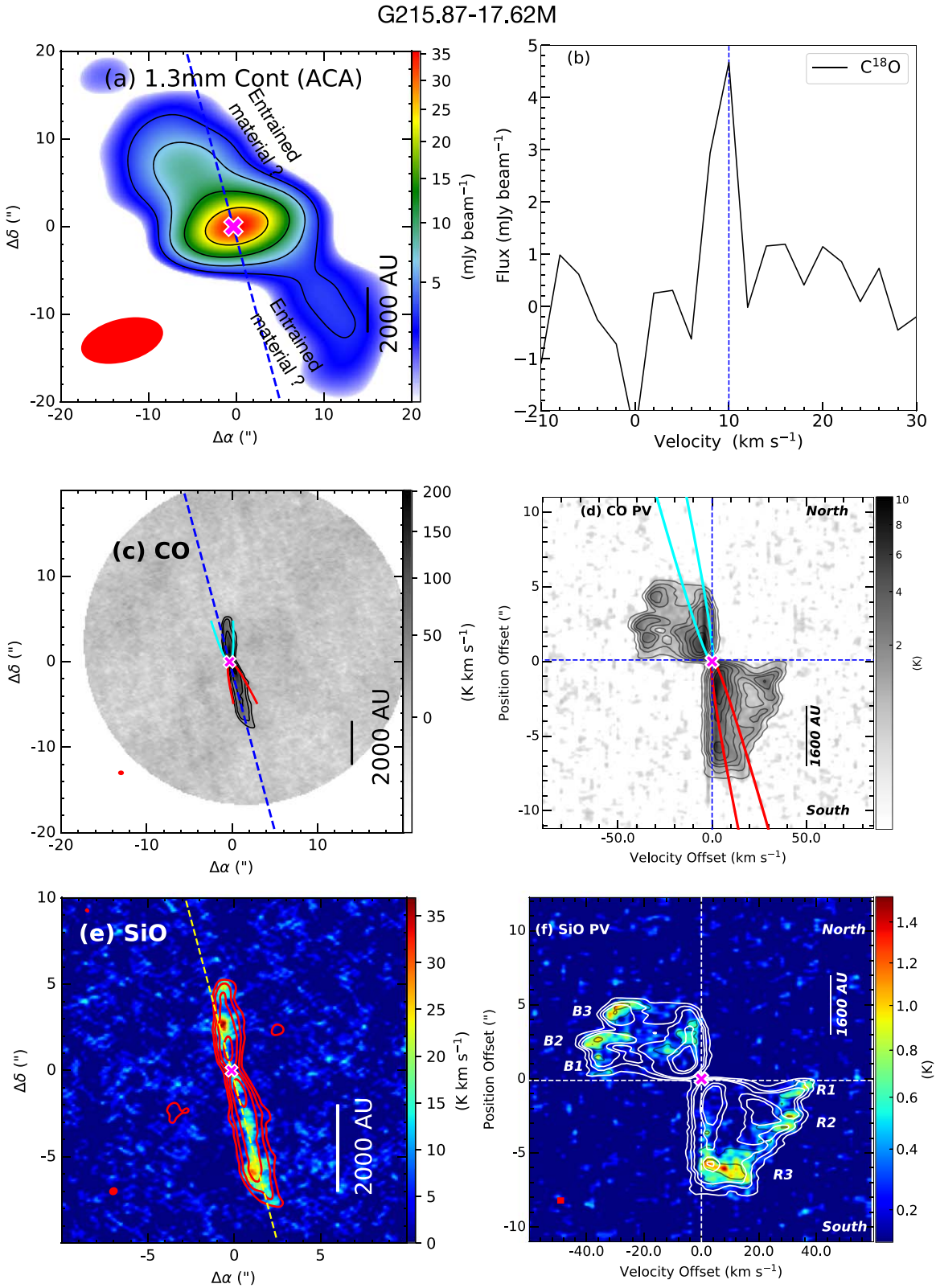

Figure B12. G215.87-17.62M. (a) 1.3 mm continuum map at ACA resolution with sensitivity ∼1.0 mJy beam^{-1}. The symbols and contour levels are the same as in Figure 1. (b) The $C^{18}O$ spectra are extracted from high-resolution maps, and $V_{sys} = 10$ km s^{-1}. All symbols are the same as in Figure 3. (c) CO emission integrated over −10 to −4 km s^{-1} and +2−10 km s^{-1} with sensitivity $\sigma \sim 5.8$ K km s^{-1}, with similar symbols to those in Figure 4(a). (d) CO PV diagram with sensitivity 0.21 K, with similar symbols and contours to those in Figure 4(b). (e) SiO emission integrated over −40 to +38 km s^{-1} with sensitivity 2.5 K km s^{-1}, with similar symbols and contours to those in Figure 4(a). (f) SiO emission with sensitivity 0.13 K, with similar symbols and contours to those in Figure 4(b). The "?" mark indicates that the present observations could not confirm the scenario.

B.12. G215.87-17.62M

Figure B12 shows the continuum and different components of emissions for G215.87-17.62M in the same order as Figure B1. Currently, there are no available measurements of $T_{\rm bol}$ and $L_{\rm bol}$ for this source in the literature. The envelope mass is estimated to be $M_{\rm env} \sim 0.3 \pm 0.07\ M_{\odot}$. The 1.3 mm continuum is extended along the northeast-to-southwest direction, possibly representing the entrained material along the outflow cavity wall. However, the continuum emission is extended beyond the length of the outflow/jet; thus, it is not clear whether the entirety of the extended continuum emission is due to the entrained material or there is some other mechanism involved.

The CO and SiO velocity dispersion and spatial extensions are relatively similar. From PV diagrams, it is difficult to separately identify the wind/outflow and jet components. Assuming that most of the low-velocity material is from wind/outflow shell, the inclination angle is estimated to be $i \sim 30^{+10}_{-10}$ deg. The SiO emission is extended from low velocity to high velocity, making it difficult to measure the jet velocity. The mean jet velocity is $V_j \sim 30 \pm 10$ km s^{-1}. A few knot-like structures appear in both the outflow lobes. It exhibits a relatively low mass-loss rate $\dot{M}_j \sim 3.2 \times 10^{-7}\ M_{\odot}\,{\rm yr}^{-1}$. The mean episodes of the ejection are $\mathcal{T}_{\rm knot} \sim 66^{+30}_{-25}$ yr, corresponding to a perturbation zone of Keplerian radius ∼4.5–14 au. The dynamical age of the blueshifted lobe is $\mathcal{T}_{\rm DynAge,blue} \sim 219^{+99}_{-81}$ yr, and for the redshifted lobe it is $\mathcal{T}_{\rm DynAge,red} \sim 292^{+133}_{-108}$ yr, each corrected for inclination angle. We estimate that this system is less than 1000 yr old, a conservative value. A smaller spatial extension, smaller dynamical age, lower jet mass ejection rate, and the presence of a brighter SiO jet suggest that this source could be a very low mass and low luminosity object in an extremely early stage of protostellar evolution.

Appendix C
Objects with Complex SiO Emission Morphology and Not Considered for Jet Parameter Estimation

C.1. G192.32-11.88N

Figure C1 shows different components of the studied continuum and emission maps in the same order as Figure B1. No $T_{\rm bol}$ and $L_{\rm bol}$ estimations are currently unavailable for this object in the literature. The envelope mass deduced from 1.3 mm continuum is estimated to be $\sim 1.2 \pm 0.18\ M_{\odot}$.

The CO integrated map shows that the outflow shell structure is blended with the ambient molecular cloud in the southeast (blueshifted) lobe. Therefore, to probe the outflow shell, we consider high-velocity components, represented by the higher contours in the CO integrated map. The redshifted lobe appears to be much shorter in length than the blueshifted lobe, possibly due to the presence of the ambient cloud in the blueshifted lobe, forming an extended blended structure. We measured the average inclination angle to be $i \sim 50^{+10}_{-10}$ deg. In the SiO integrated emission, a bright SiO emission is evident at the tip of the blueshifted lobe but absent in the redshifted lobe. Scattered SiO emission is also observed along the whole blueshifted lobe. The SiO PV diagram shows SiO emission along the outflow axis, close to the systemic velocity of the source. If this emission originates from the jet, then the jet velocity would be $V_j \sim 2 \pm 2$ km s^{-1}, where $V_{j,\rm cor} = V_j/\sin i$. Such a low velocity is unlikely to synthesize a high-density SiO jet. Therefore, we suggest that the SiO emission at the tip of the blueshifted lobe could be the interaction zone between two outflows and the ambient material, as in the case of G208.89-20.04Walma (Dutta et al. 2022a). To confirm the origin of the SiO emission—whether it is indeed a jet or a collision zone—further high-sensitivity observations are required.

C.2. G200.34-10.97N

Figure C2 shows the continuum, C^{18}O, CO, and SiO emission of the object G200.34-10.97N in the same order as Figure B1. The object is a Class 0 source with $T_{\rm bol} \sim 43 \pm 10$ K and $L_{\rm bol} \sim 1.5 \pm 0.6\ L_{\odot}$. The envelope mass is estimated to be $M_{\rm env} \sim 0.51 \pm 0.08\ M_{\odot}$.

The outflow opening near the source is narrow; however, as we move outward, the outflow appears wider. One possible explanation for this could be that the thick envelope near the source compresses the outflow opening and, upon moving away from the envelope, the outflow suddenly opens up and becomes wide-angle. Another possibility is that the outflow is blending with the ambient cloud, so it appears wider as a combination of outflow and ambient cloud. Higher spatial resolution and higher velocity resolution observations would be beneficial to study the kinematics and disentangle these components. We are not able to find a good fit for the outer shell to determine the inclination angle. A tentative fitting suggests that the inclination could be $i \sim 12^{+10}_{-5}$ deg.

The SiO emission along the jet axis appears bow-shock-like, with no dense knot-like structure appearing in this observation. The SiO emission is not at a very high velocity range. The mean SiO velocity is $V_j \sim 4 \pm 2$ km s^{-1}, where $V_{j,\rm cor} = V_j/\sin i$. This suggests that the SiO emission may not be associated with the jet, but could rather be from the collision zone between the outflow and the ambient cloud. Further higher velocity and higher sensitivity could help to disentangle these two scenarios.

C.3. G205.46-14.56M2 (HOPS 387 and HOPS 386)

Figure C3 displays the 1.3 mm continuum (panel (a)), C^{18}O spectra (panel (b)), integrated CO map (panel (c)), and integrated SiO map (panel (d)) of the G205.46-14.56M2 system. It contains five sources, of which G205.46-14.56M2_A, B, C, and D are in a common envelope of mass $M_{\rm env} \sim 1.04 \pm 0.19\ M_{\odot}$. Sources A and B form part of the Class I system HOPS 387, while sources C and D are components of another Class I system, HOPS 386 (Tobin et al. 2020).

From the CO map, the outflow components from different sources are not clearly identified. The outflow direction of "B" can be determined, but the outflow components from different sources are not distinguishable. A knot-like emission in the SiO emission is observed, which could be a jet component of source D or C. Alternatively, it could be possible that sources C and/or D are line-rich, akin to hot corinos. As such, the detected emission is mimicking SiO emission; however, it could actually represent other line emissions emanating from the hot corinos near the source. The possibility of another

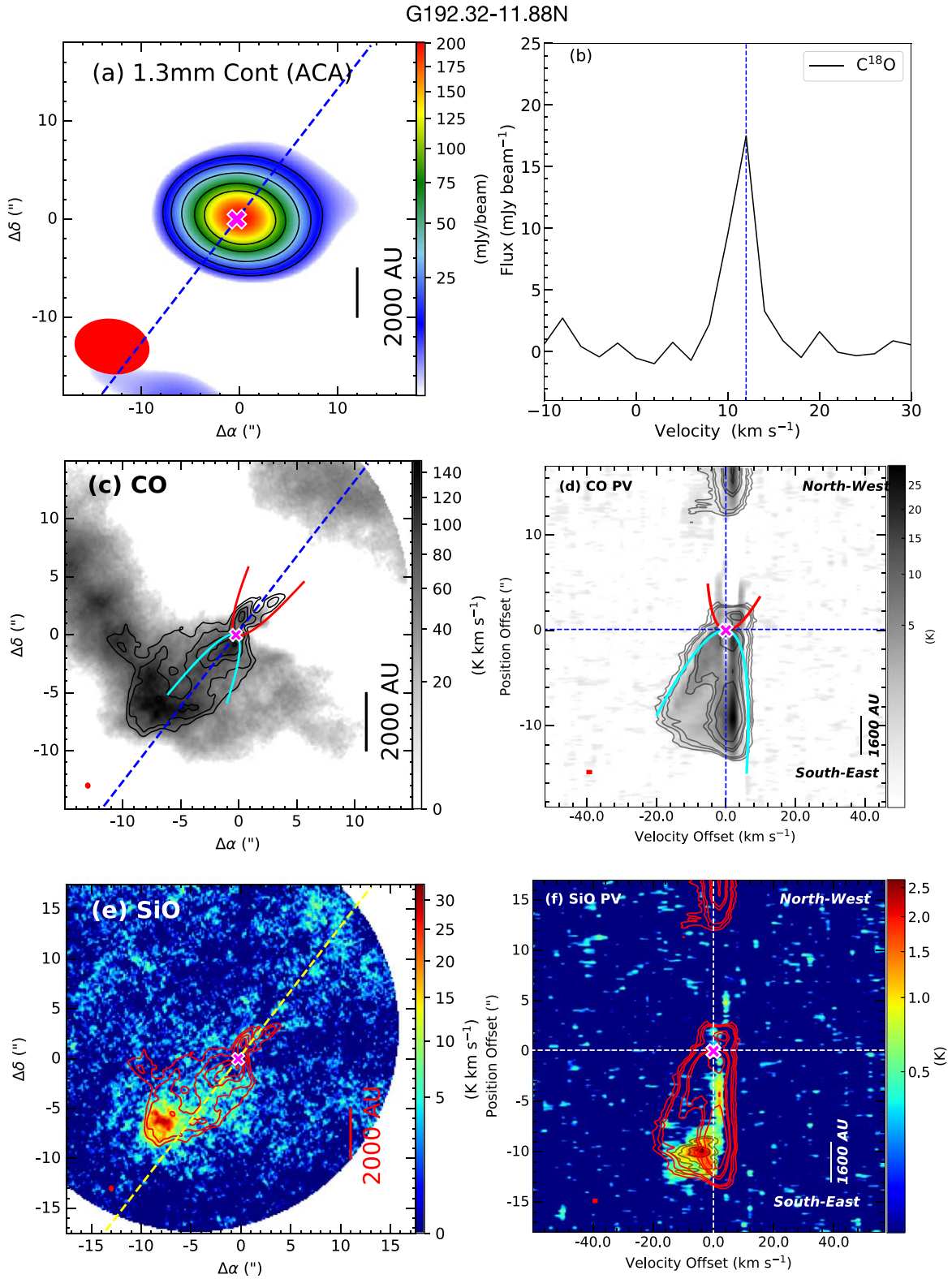

Figure C1. G192.32-11.88N. (a) 1.3 mm continuum map at ACA resolution with sensitivity ∼2.9 mJy beam^{-1}. The symbols and contour levels are the same as in Figure 1. (b) The $C^{18}O$ spectra are extracted from high-resolution maps, and $V_{sys} = 12$ km s^{-1}. All symbols are the same as in Figure 3. (c) Integrated CO emission with sensitivity 6.4 K km s^{-1}, with similar symbols and contours to those in Figure 4(a). (d) CO PV diagram with sensitivity 0.13 K, with similar symbols and contours to those in Figure 4(b). (e) Integrated SiO emission with sensitivity 2.7 K km s^{-1}, with similar symbols and contours to those in Figure 5(a). (f) SiO PV diagram with sensitivity $\sigma = 0.47$ K, with similar symbols to those in Figure 5(b). The SiO contour labels are at (1.5, 2, 3, 4) × σ.

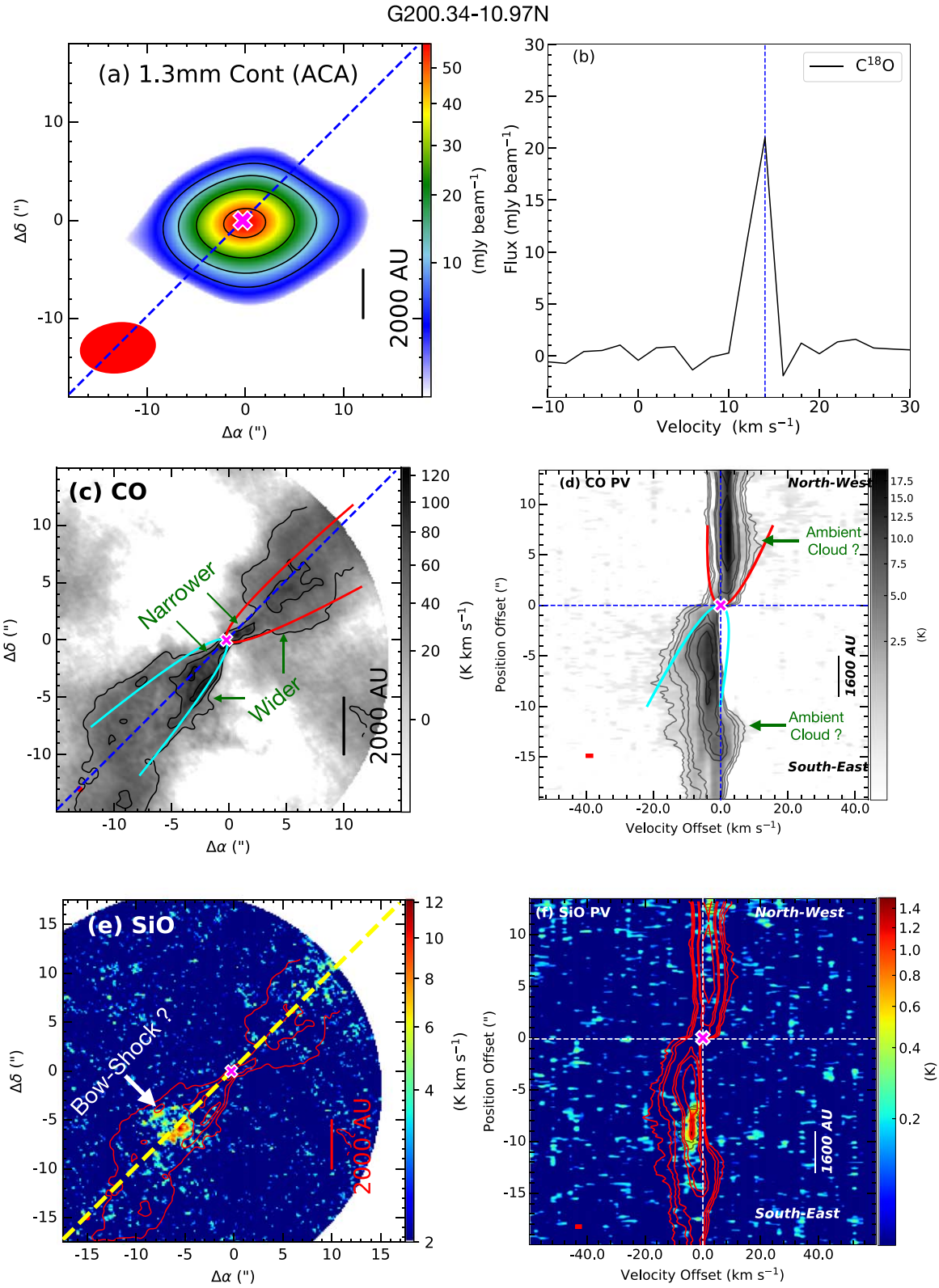

Figure C2. G200.34-10.97N. (a) 1.3 mm continuum map at ACA resolution with sensitivity ∼2.0 mJy beam^{-1}. The symbols and contour levels are the same as in Figure 1. (b) The C^{18}O spectra are extracted from high-resolution maps, and V_{sys} = 14 km s^{-1}. All symbols are the same as in Figure 3. (c) CO map integrated over −20 to +12 km s^{-1} with sensitivity 9.9 K km s^{-1}, with similar symbols and contours to those in Figure 4(a). (d) CO PV diagram with sensitivity 0.14 K, with similar symbols and contours to those in Figure 4(b). (e) SiO emission map integrated over −10 to +10 km s^{-1} emission with sensitivity 3.7 K km s^{-1}, with similar symbols and contours to those in Figure 5(a). (f) SiO PV diagram with sensitivity σ = 0.12 K, with similar symbols to those in Figure 5(b). The SiO contour labels are at (2, 3, 4) × σ. The "?" mark indicates that the present observations could not confirm the scenario.

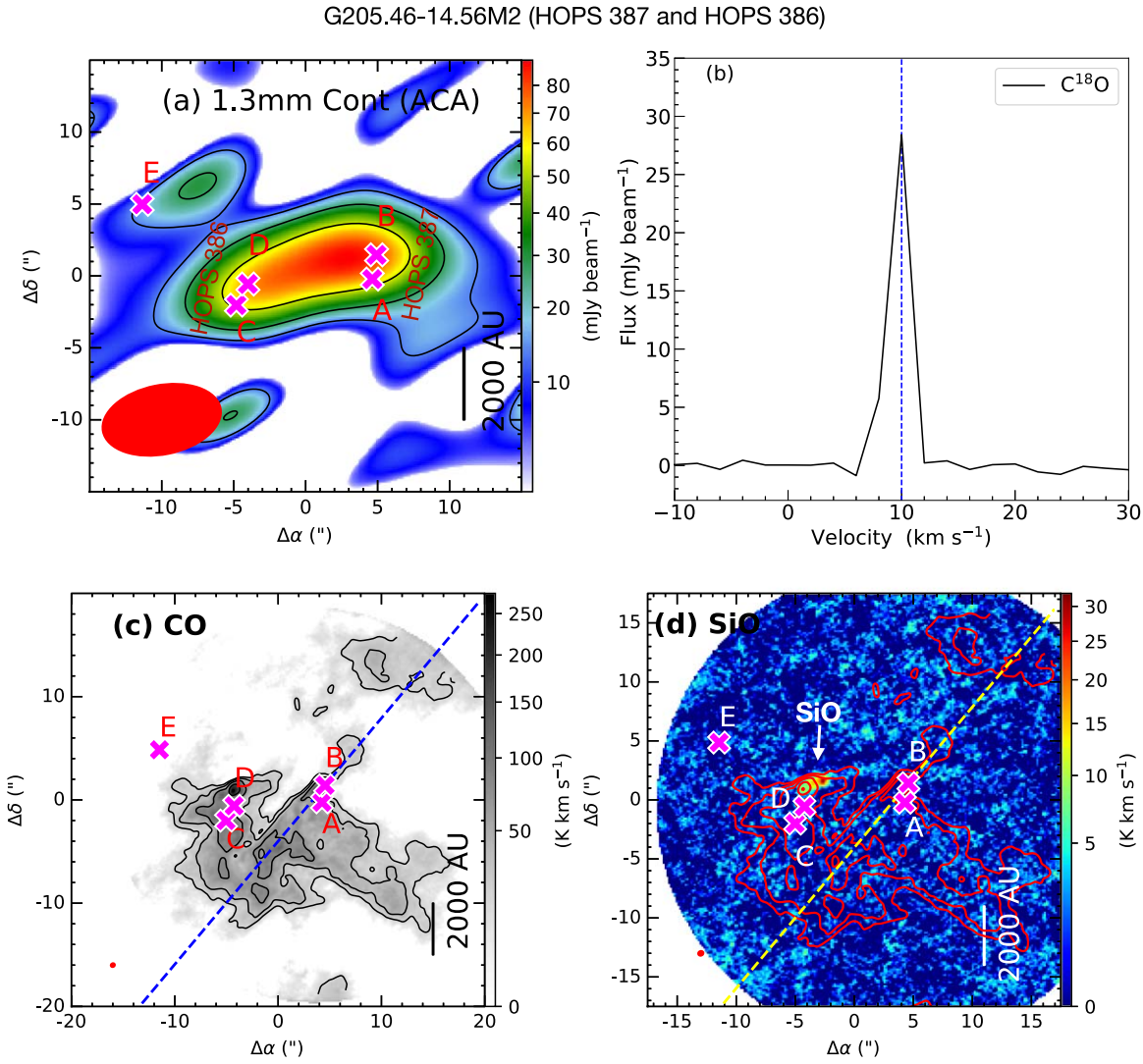

Figure C3. G205.46-14.56M2. (a) 1.3 mm continuum map at ACA resolution with sensitivity ∼4.5 mJy beam^{-1}. The symbols and contour levels are the same as in Figure 1. (b) The C^{18}O spectra are extracted from high-resolution maps, and $V_{sys} = 14$ km s^{-1}. All symbols are the same as in Figure 3. (c) Integrated CO emission with sensitivity 6.15 K km s^{-1}, with similar symbols and contours to those in Figure 4(a). (d) Integrated SiO emission with sensitivity 2.1 K km s^{-1}, with similar symbols and contours to those in Figure 5(a).

unidentified origin is also viable. From the present status of the observations, it is not possible to conclusively determine the origin of this emission.

C.4. G205.46-14.56N2 (HOPS 401)

Figure C4 shows the continuum and emission components of G205.46-14.56N2 in the same order as Figure C3. This is a Class 0 source with $T_{bol} \sim 32 \pm 8$ K, $L_{bol} \sim 0.8 \pm 0.3\ L_{\odot}$, and an envelope mass of $M_{env} \sim 0.85 \pm 0.13\ M_{\odot}$. The source also coincides with the location of HOPS 401 (Karnath et al. 2020; Tobin et al. 2020).

The outflow seen in the CO map is difficult to distinguish from the ambient cloud. We detected SiO emission in the tip of the northeastern lobe of the outflow, which could be either a bow shock structure of the jet or a collision zone between the outflow and ambient cloud. Unfortunately, due to the low sensitivity in both the SiO and CO maps, we were unable to determine the outflow and jet parameters for this source.

C.5. G209.55-19.68N1 (HOPS 12)

Figure C5 shows different continuum and emission components of G209.55-19.68N1 in the same order as Figure B1. G209.55-19.68N1 is a multiple system, where source "A" is responsible for driving the largest outflow. Two other sources, "B" and "C," form a close system that drives a smaller-scale outflow. High-resolution maps of G209.55-19.68N1 reveal that "A" is itself a close binary system and "B-C" is a single source (HOPS 12; Dutta et al. 2020). In the ACA resolution, all three sources are within the same common envelope of mass $M_{env} \sim 1.98 \pm 0.3\ M_{\odot}$. In this paper, we consider $T_{bol} \sim 47 \pm 13$ K and $L_{bol} \sim 9.0 \pm 3.7\ L_{\odot}$ for the main outflow source "A."

The northern component of the outflow shell from source "A" appears wider than the southern part. Within the northern outflow shell, there is a secondary outflow from the "B" or/and "C" system. The interaction between those two outflows creates a shock region, which is faintly detected with SiO emission. This SiO emission is not located along the jet axis. Due to the presence of the secondary source and blending with

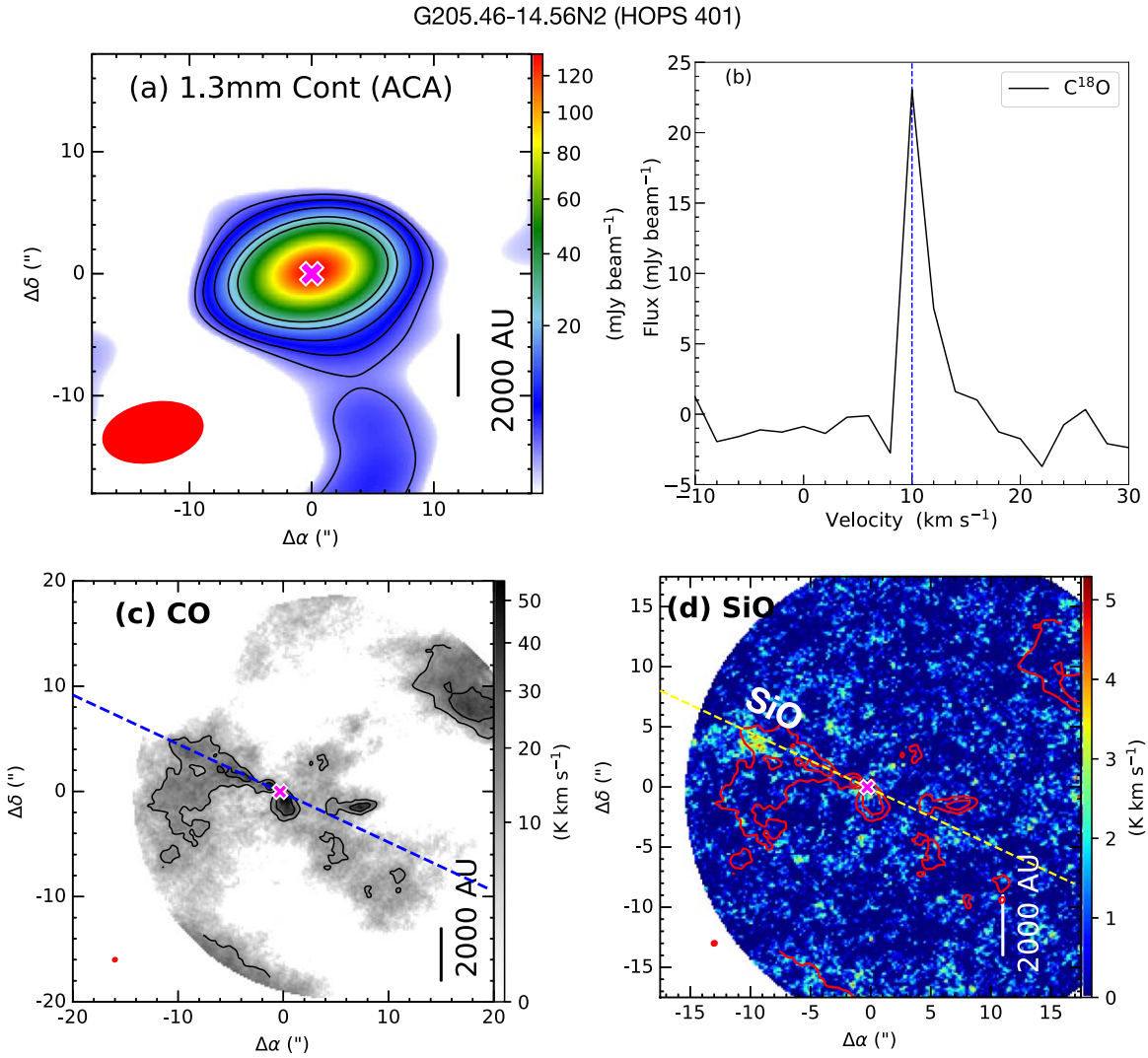

Figure C4. G205.46-14.56N2. (a) 1.3 mm continuum map at ACA resolution with sensitivity ∼0.8 mJy beam^{-1}. The symbols and contour levels are the same as in Figure 1. (b) The C^{18}O spectra are extracted from high-resolution maps, and $V_{sys} = 10$ km s^{-1}. All symbols are the same as in Figure 3. (c) Integrated CO emission with sensitivity 4.5 K km s^{-1}, with similar symbols and contours to those in Figure 4(a). (d) Integrated SiO emission with sensitivity 1.15 K km s^{-1}, with similar symbols and contours to those in Figure 5(a).

the ambient cloud, the northern outflow appears wider than the southern component. A similar outflow collision zone was reported for another protostellar system, BHR 71 (Zapata et al. 2018). The southern component of CO emission (redshifted) is narrower than the northern lobe. Here we visually checked each channel to identify the likely outflow shell. In the northern lobe, we chose a CO emission width close to the source, and in the southern lobe, we consider up to 2σ to define the outflow shell. We measured the average inclination angle from the CO shell to be $\sim i \sim 27^{+15}_{-10}$ deg. The tiny knot-like structure in SiO emission (PV diagram) could not be confirmed as a real knot from the current observations.

C.6. G211.47-19.27S (HOPS 288)

Figure C6 shows the continuum and emission components of G211.47-19.27S in the same order as Figure C3. From the CO velocity channel maps, we have detected three distinct outflow sources, all of which are within a common envelope of mass $M_{env} \sim 3.37 \pm 0.52\ M_{\odot}$. The location of the system coincides with HOP 288. The combined system has $T_{bol} \sim 49 \pm 21$ K and $L_{bol} \sim 180 \pm 70\ L_{\odot}$. Such a high bolometric luminosity and temperature suggest that the system is in the Class I phase; however, disentangling the nature of individual components within this multiple-source system is challenging owing to the low-resolution infrared observations.

The properties of the three CO outflows could not be separated based on the current state of our observations. Bright monopolar SiO emission is observed along the jet axis of source "B." The SiO emission is in the redshifted outflow lobe of "B" with a mean velocity $V_j \sim 5 \pm 2$ km s^{-1}. Source "A" is possibly a line-rich "hot-corino" object (Hsu et al. 2022). Given that the outflow/jet components for the different sources could not be differentiated, the outflow/jet parameters have not been estimated.

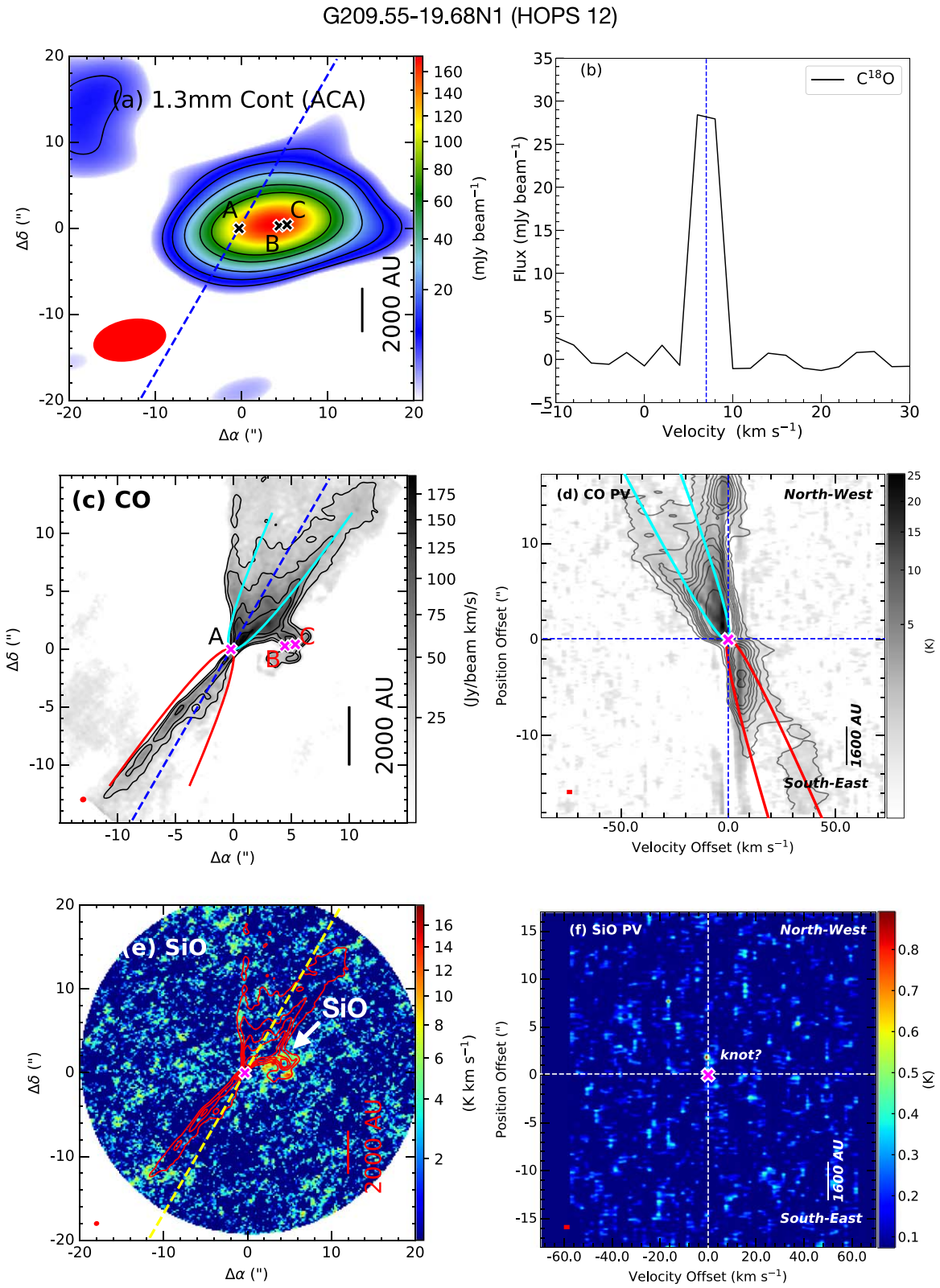

Figure C5. G209.55-19.68N1. (a) 1.3 mm continuum map at ACA resolution with sensitivity ∼2.0 mJy beam^{-1}. The symbols and contour levels are the same as in Figure 1. (b) The C^{18}O spectra are extracted from high-resolution maps, and $V_{sys} = 7$ km s^{-1}. All symbols are the same as in Figure 3. (c) Integrated CO emission with sensitivity 7.8 K km s^{-1}, with similar symbols and contours to those in Figure 4(a). (d) CO PV diagram with sensitivity 0.12 K, with similar symbols and contours to those in Figure 4(b). (e) Integrated SiO emission with sensitivity 2.6 K km s^{-1}, with similar symbols and contours to those in Figure 5(a). (f) SiO PV diagram with sensitivity $\sigma = 0.15$ K, with similar symbols to those in Figure 5(b). The "?" mark indicates that the present observations could not confirm the candidacy of the knot.

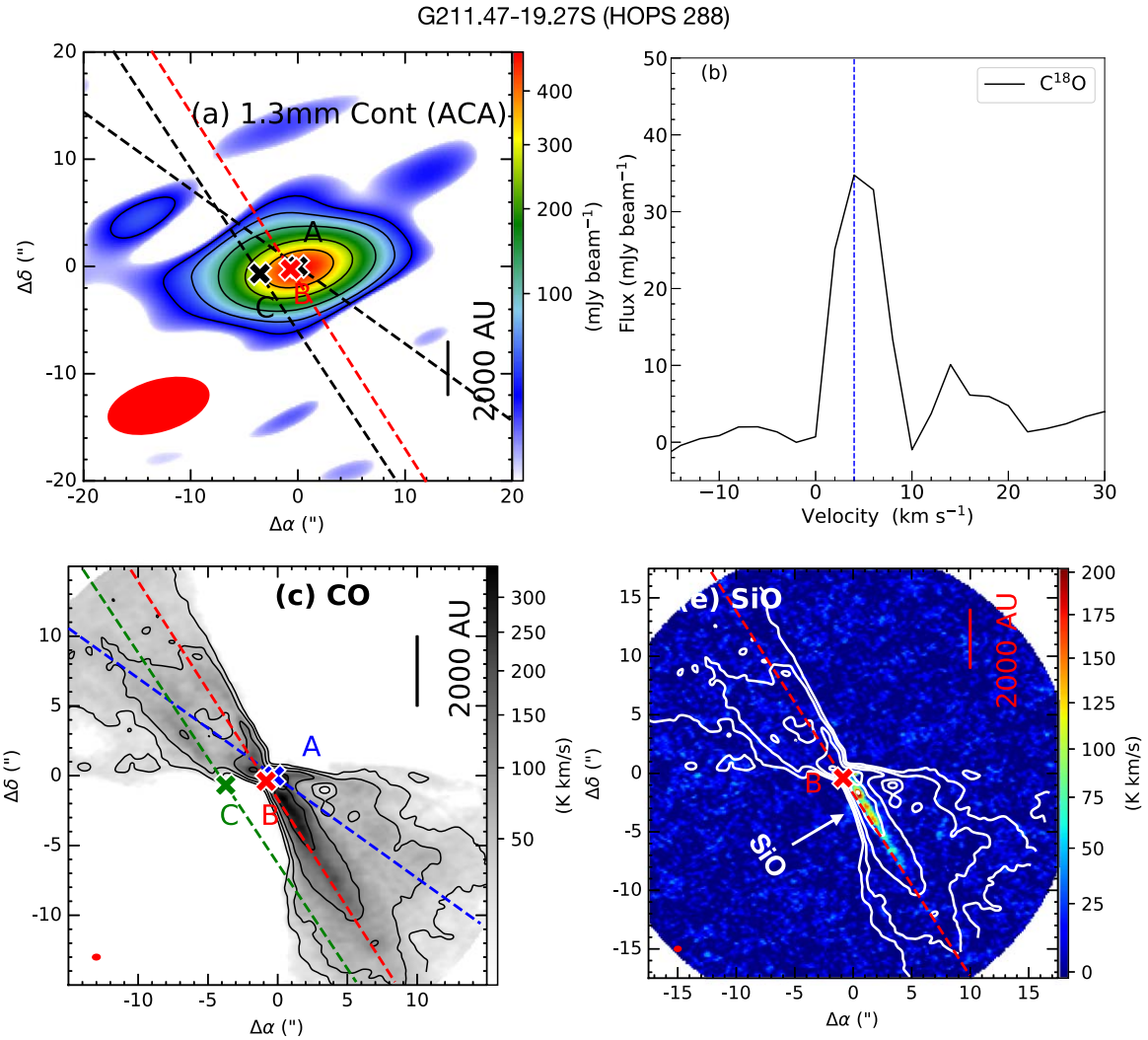

Figure C6. G211.47-19.27S. (a) 1.3 mm continuum map at ACA resolution with sensitivity ∼2.0 mJy beam^{-1}. The symbols and contour levels are the same as in Figure 1. (b) The C^{18}O spectra are extracted from high-resolution maps, and $V_{sys} = 4$ km s^{-1}. All symbols are the same as in Figure 3. (c) Integrated CO emission with sensitivity 8.6 K km s^{-1}, with similar symbols and contours to those in Figure 4(a). (d) CO PV diagram with sensitivity 0.15 K, with similar symbols and contours to those in Figure 4(b). (e) Integrated SiO emission with sensitivity 1.9 K km s^{-1}, with similar symbols and contours to those in Figure 5(a).

Appendix D
Objects with No SiO Emission but Well-defined CO Outflow

D.1. G192.12-11.10

Figure D1 shows the 1.3 mm continuum (panel (a)), C^{18}O spectra (panel (b)), integrated CO map (panel (c)), and CO PV diagram (panel (d)) of G192.12−11.20. It is a Class 0 source with $T_{bol} \sim 44 \pm 15$ K, $L_{bol} \sim 9.5 \pm 4.0$ $L_{\odot}$, and an envelope mass of $M_{env} \sim 1.21 \pm 0.18$ $M_{\odot}$. Although the source is in the Class 0 phase, we do not observe any jet-like components along the flow axis in either SiO or CO. However, if the jet is very high density and optically thicker for SiO (5–4) and CO (2–1), then the jet components could be detected in higher transitions, such as SiO (8–7) and CO (3–2). The object appears to be oriented nearly edge-on with an inclination angle of $i \sim 15^{+10}_{-5}$ deg.

D.2. G196.92-10.37

G196.92-10.37 (Figure D2; in the same sequence as Figure D1) is a wide multiple system, where the strongest outflow is driven by source "A" along the northeast-to-southwest direction. T_{bol} and L_{bol} of source "A" are currently unknown. The outflows from sources "B" and "C" are less spatially extended following a north–south direction, and they blend with the blueshifted lobe from source "A." There is no way to disentangle the outflow components from different sources from the present data set. Assuming minimal contamination from the outflows of "B" and "C" to the "A" outflow, we have estimated the outflow force for source "A." The envelope mass for source "A" is $M_{env} \sim 0.71 \pm 0.12$ $M_{\odot}$. It is possibly highly inclined, close to face-on (i $\sim 70^{+10}_{-10}$ deg). There is no detection of SiO emission in this target field.

D.3. G203.21-11.20W1

Figure D3 shows various components of G203.21-11.20W1 in the same sequence as Figure D1. An outflow is emanating from the source, which has an envelope mass of $M_{env} \sim 0.54 \pm 0.11$ $M_{\odot}$. Notably, there is no reported infrared emission for this source in the literature. The outflow is characterized by a narrow angle and has a well-defined cavity wall. No jet-like

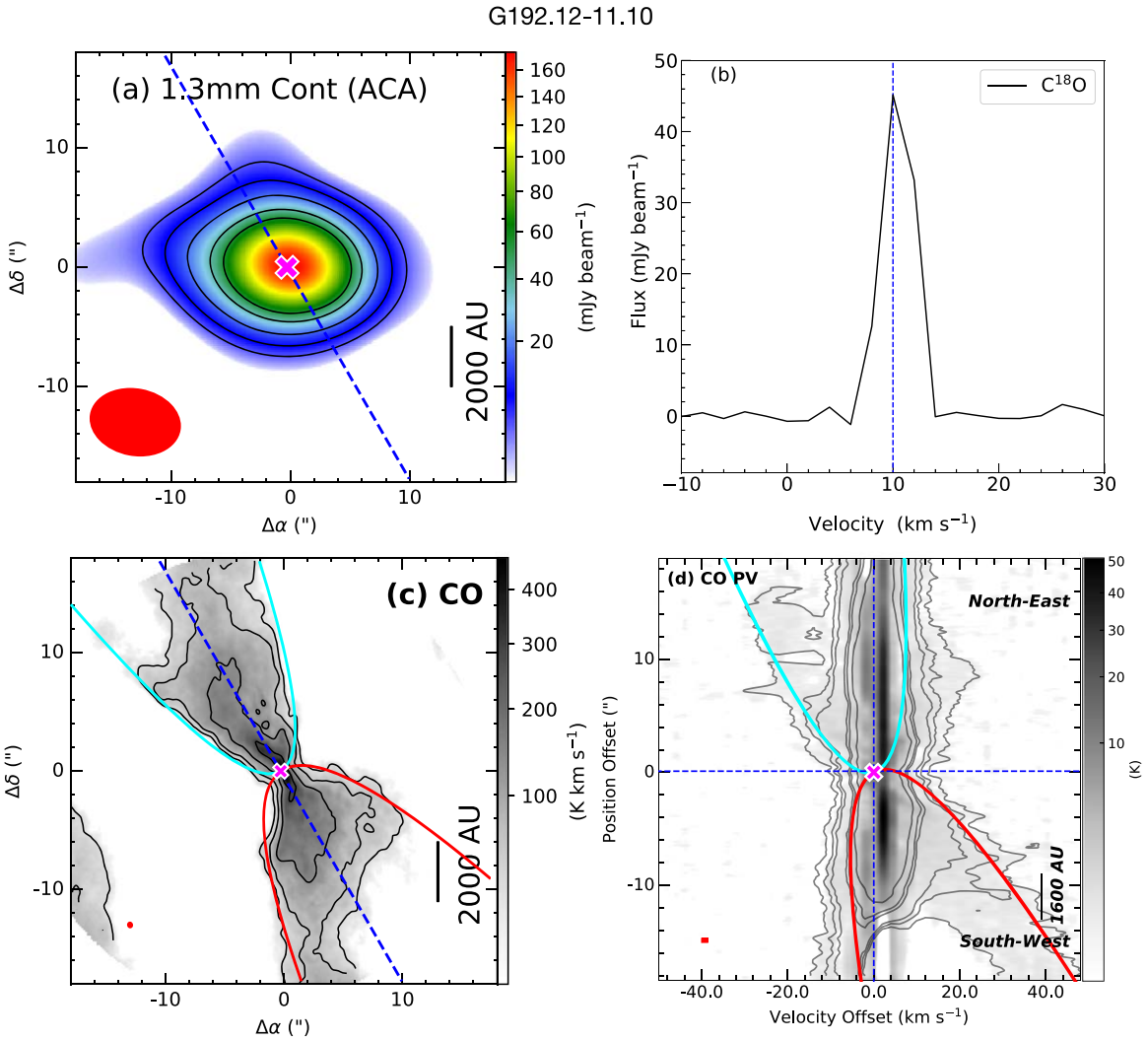

Figure D1. G192.12-11.10. (a) 1.3 mm continuum map at ACA resolution with sensitivity ∼1.5 mJy beam^{-1}. The symbols and contour levels are the same as in Figure 1. (b) The C^{18}O spectra are extracted from high-resolution maps, and $V_{sys} = 10$ km s^{-1}. All symbols are the same as in Figure 3. (c) Integrated CO emission with sensitivity 11.5 K km s^{-1}, with similar symbols and contours to those in Figure 4(a). (d) CO PV diagram with sensitivity 0.16 K, with similar symbols and contours to those in Figure 4(b).

high-velocity component has been detected in either SiO or CO. We measured the average inclination angle to be $\sim i \sim 20^{+10}_{-5}$ deg.

D.4. G208.68-19.20S (HOPS 84)

G208.68-19.20S (HOPS 84; Figure D4) is a close binary system with $T_{bol} \sim 96 \pm 25$ K, $L_{bol} \sim 49 \pm 18$ $L_\odot$, and an envelope mass of $M_{env} \sim 1.55 \pm 0.3$ $M_\odot$. The outflow is likely being driven by source "A." The CO PV diagram suggests that the object is nearly edge-on with an inclination angle of $i \sim 10^{+10}_{-5}$ deg. No SiO emission was detected in this target field.

D.5. G211.01-19.54N (HOPS 153)

Figure D5 shows the observed components of G211.01-19.54N (also known as HOPS 153) in the same sequence as Figure D1. It is catagorized as a Class 0 system with $T_{bol} \sim 39 \pm 12$ K and $L_{bol} \sim 4.5 \pm 1.8$ $L_\odot$. The envelope mass is $M_{env} \sim 0.81 \pm 0.16$ $M_\odot$. Continuum emission extends along the same direction as the blueshifted CO outflow, suggesting that this could represent envelope material being entrained by the outflow.

No SiO emission was detected in this target field. The blueshifted outflow shell in the PV diagram is difficult to distinguish from the ambient cloud. We assumed the likely shell structure from near-source emission and fitted it with a parabolic equation, which provides an inclination angle of $\sim i \sim 50^{+10}_{-20}$ deg.

D.6. G211.01-19.54S (HOPS 152)

Figure D6 depicts G211.01-19.54S (also known as HOPS 152), a Class 0 system with $T_{bol} \sim 52 \pm 8$ K and $L_{bol} \sim 0.9 \pm 0.4$ $L_\odot$. This is one of the VeLLOs. It possesses an envelope with a mass of $M_{env} \sim 0.21 \pm 0.04$ $M_\odot$. Only a redshifted (southern) outflow shell is detected with CO integrated emission. This could be a monopolar outflow source unless the northern outflow is blended with the ambient cloud. In the PV diagram, the emission in the blueshifted (northern) part is likely tracing ambient material. The outflow shell, even in the redshifted section, could not be distinguished in the PV diagram. Consequently, the inclination angle measurement for

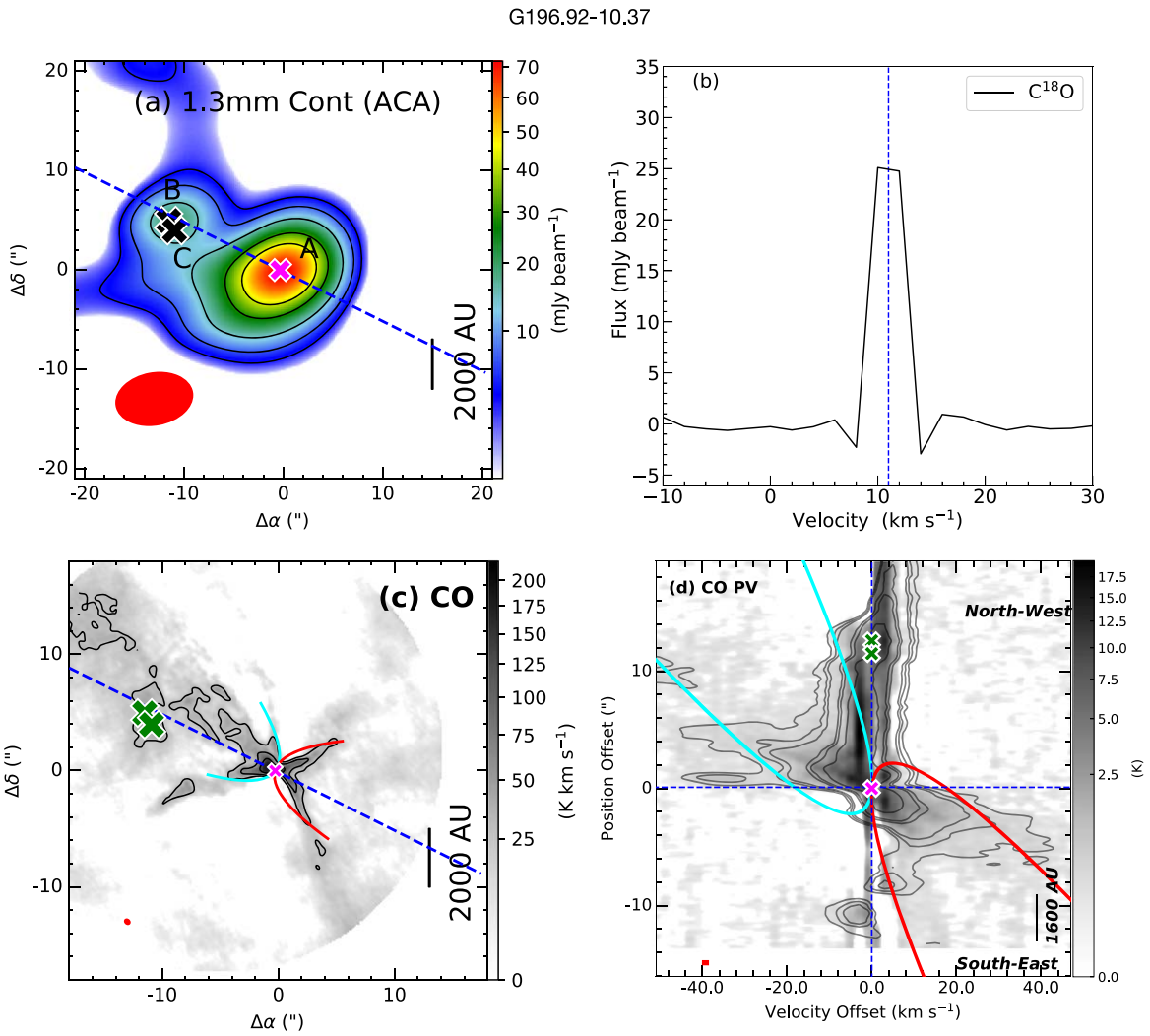

Figure D2. G196.92-10.37. (a) 1.3 mm continuum map at ACA resolution with sensitivity ∼1.2 mJy beam^{-1}. The symbols and contour levels are the same as in Figure 1. (b) The C^{18}O spectra are extracted from high-resolution maps, and $V_{sys} = 11$ km s^{-1}. All symbols are the same as in Figure 3. (c) Integrated CO emission with sensitivity 9.6 K km s^{-1}, with similar symbols and contours to those in Figure 4(a). (d) CO PV diagram with sensitivity 0.1 K, with similar symbols and contours to those in Figure 4(b).

this source is highly biased owing to the unreliable outflow shell consideration. No SiO emission is detected in this observed field.

D.7. G212.84-19.45N (HOPS 224)

G212.84-19.45N (HOPS 224; Figure D7) is a Class 0 system with $T_{bol} \sim 50 \pm 13$ K, $L_{bol} \sim 3.0 \pm 1.2\ L_{\odot}$, and an envelope mass of $M_{env} \sim 0.52 \pm 0.09\ M_{\odot}$. In the CO integrated emission of this system, the redshifted outflow appears wider than the blueshifted lobe. We have estimated an average inclination angle $\sim i \sim 25^{+15}_{-10}$ deg. Interestingly, a high-velocity CO component can be observed in the redshifted lobe, which may be indicative of a jet. However, no SiO emission has been detected in this field.

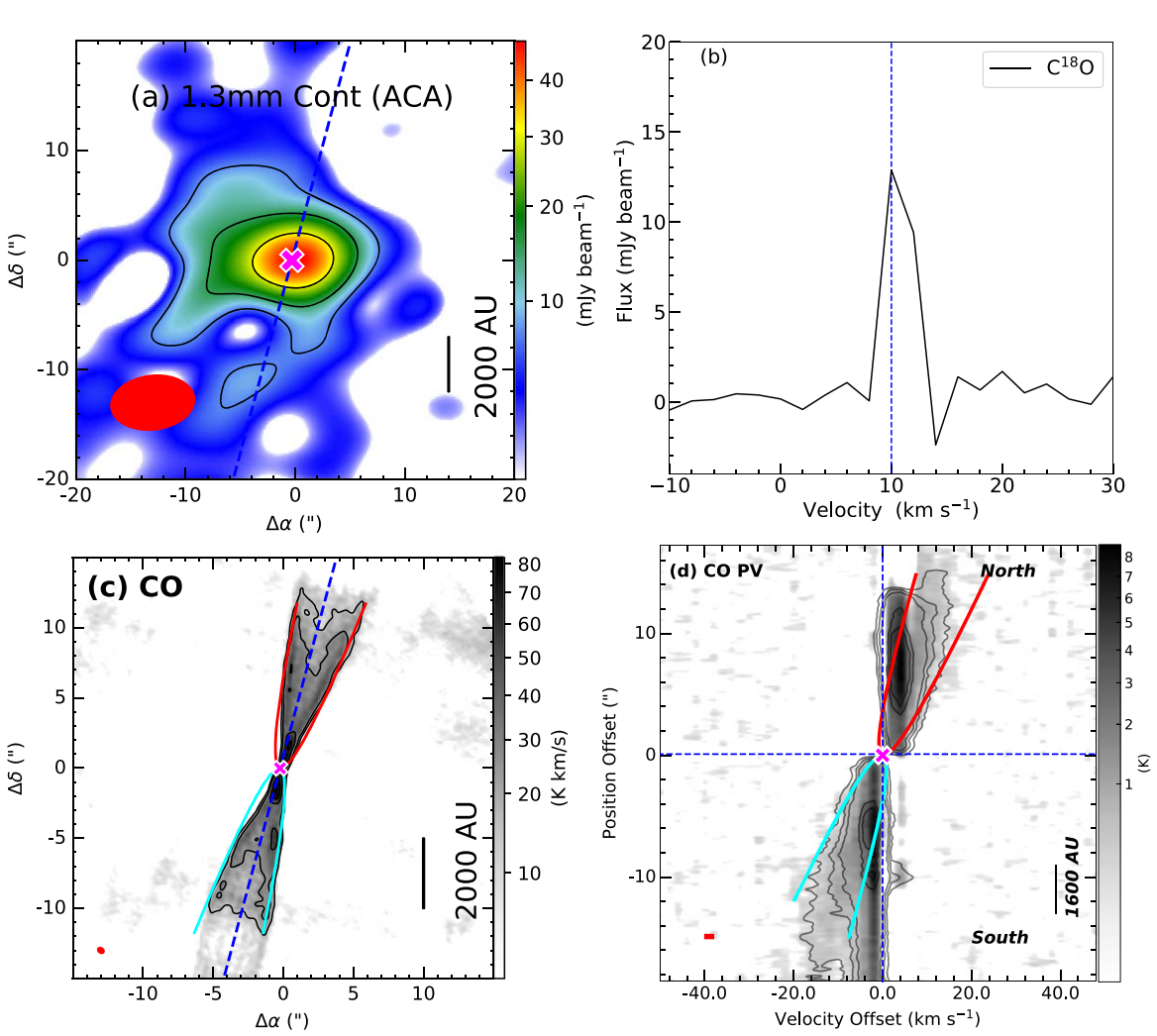

Figure D3. G203.21-11.20W1. (a) 1.3 mm continuum map at ACA resolution with sensitivity ∼3.36 mJy beam^{-1}. The symbols and contour levels are the same as in Figure 1. (b) The C^{18}O spectra are extracted from high-resolution maps, and $V_{sys} = 10$ km s^{-1}. All symbols are the same as in Figure 3. (c) Integrated CO emission with sensitivity 5.14 K km s^{-1}, with similar symbols and contours to those in Figure 4(a). (d) CO PV diagram with sensitivity 0.11 K, with similar symbols and contours to those in Figure 4(b).

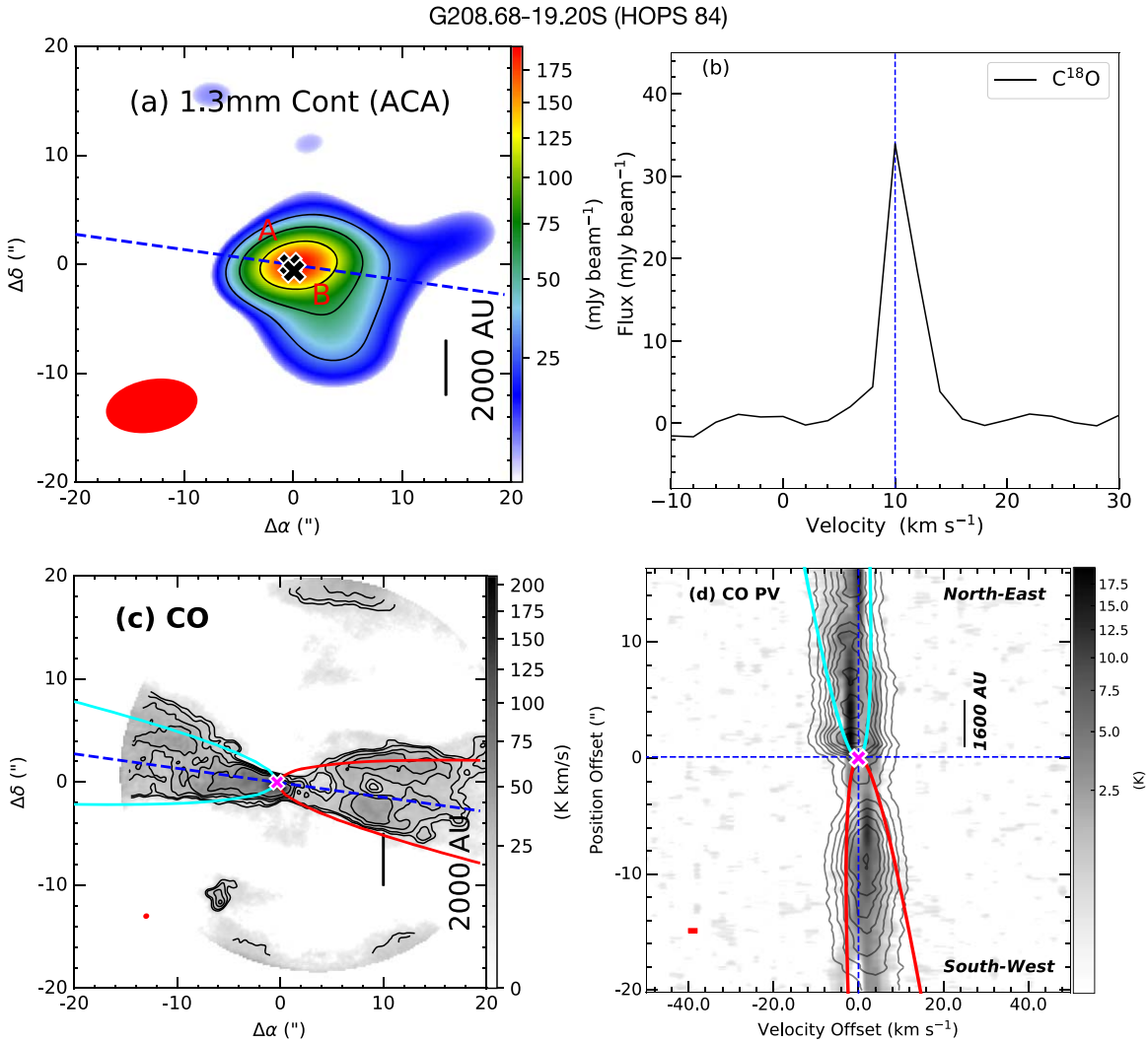

Figure D4. G208.68-19.20S. (a) 1.3 mm continuum map at ACA resolution with sensitivity ∼10 mJy beam^{-1}. The symbols and contour levels are the same as in Figure 1. (b) The C^{18}O spectra are extracted from high-resolution maps, and $V_{sys} = 10$ km s^{-1}. All symbols are the same as in Figure 3. (c) Integrated CO emission with sensitivity 1.5 K km s^{-1}, with similar symbols and contours to those in Figure 4(a). (d) CO PV diagram with sensitivity 0.16 K, with similar symbols and contours to those in Figure 4(b).

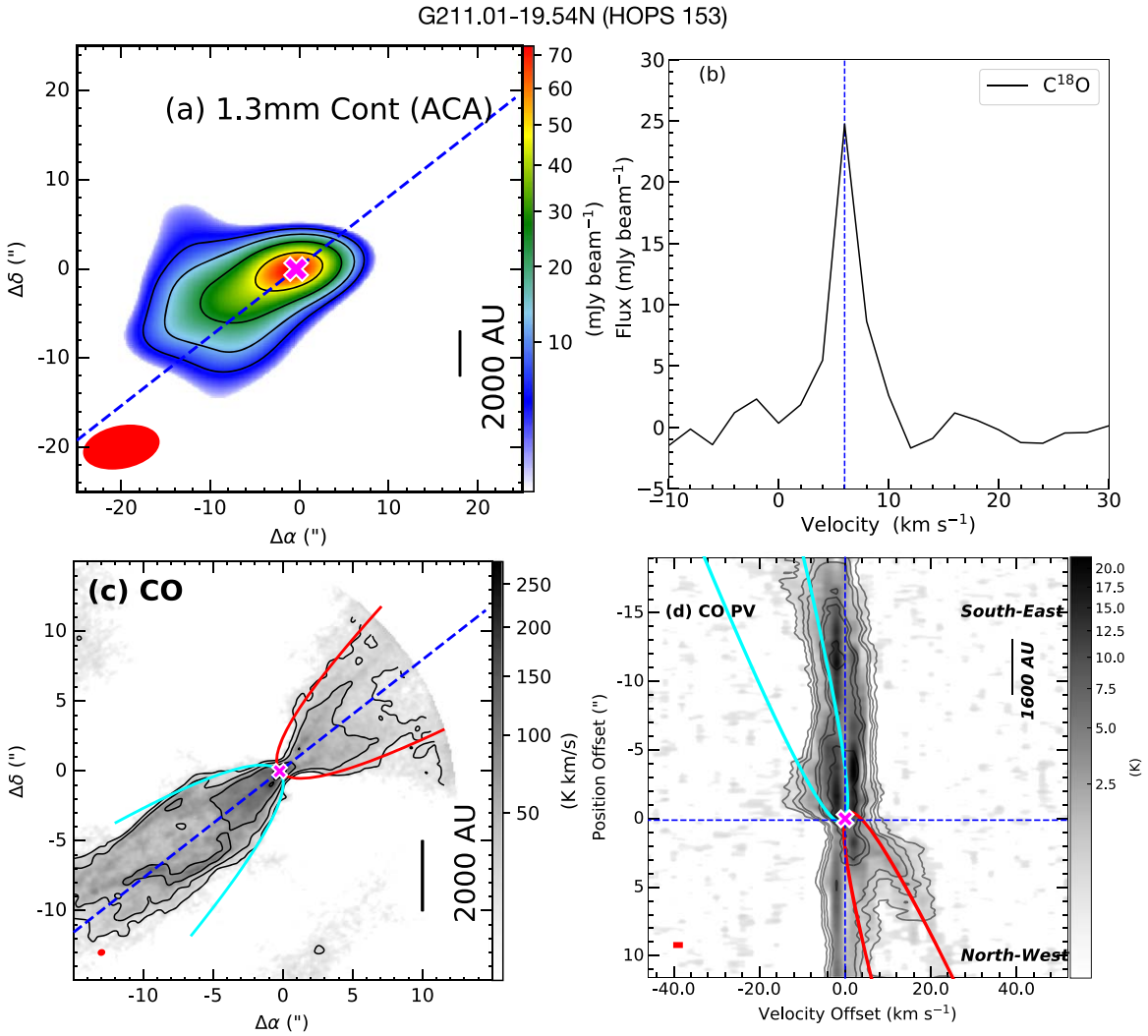

Figure D5. G211.01-19.54N. (a) 1.3 mm continuum map at ACA resolution with sensitivity ∼2 mJy beam^{-1}. The symbols and contour levels are the same as in Figure 1. (b) The C^{18}O spectra are extracted from high-resolution maps, and $V_{sys} = 6$ km s^{-1}. All symbols are the same as in Figure 3. (c) Integrated CO emission with sensitivity 6.3 K km s^{-1}, with similar symbols and contours to those in Figure 4(a). (d) CO PV diagram with sensitivity 0.16 K, with similar symbols and contours to those in Figure 4(b).

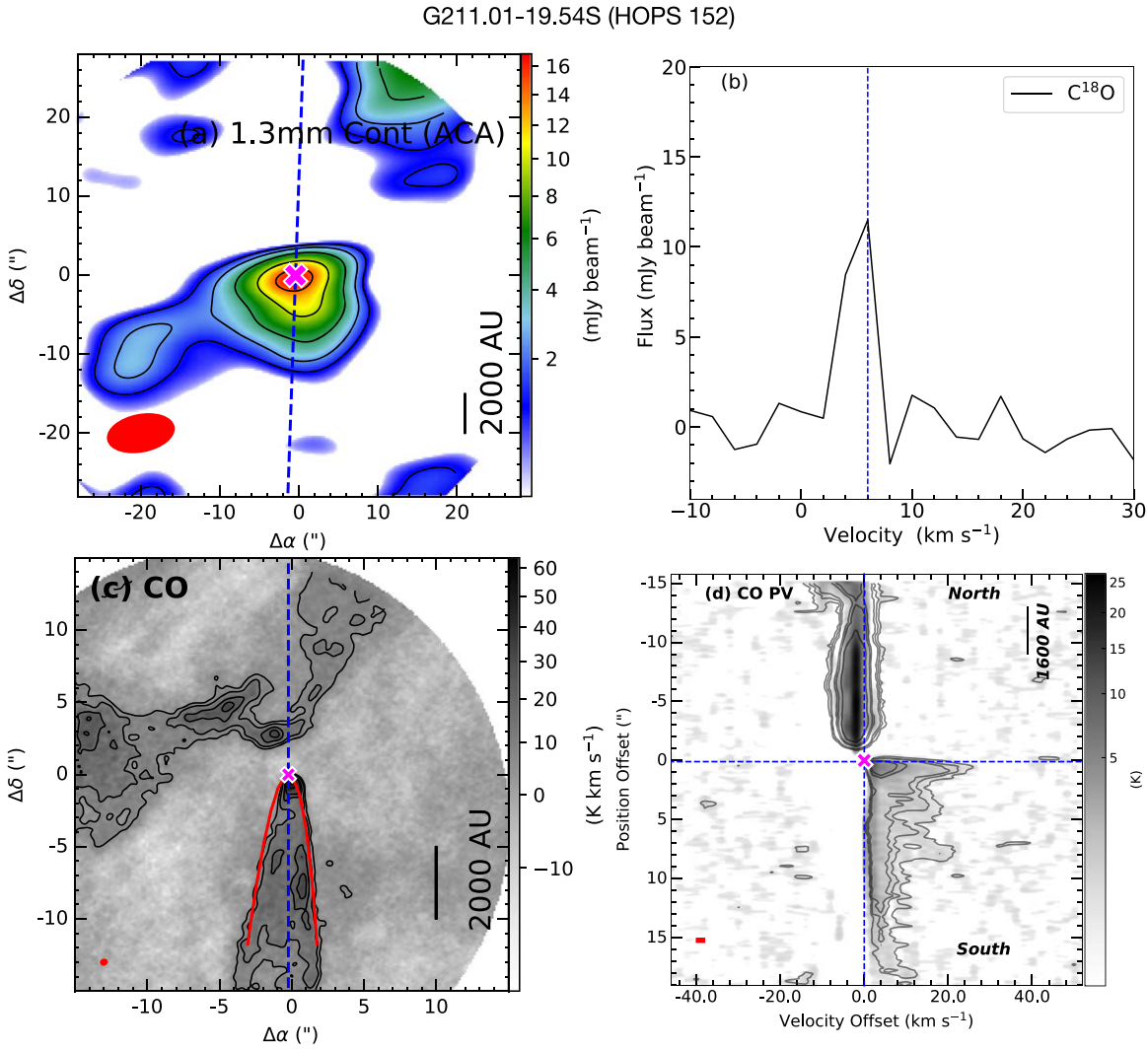

Figure D6. G211.01-19.54S. (a) 1.3 mm continuum map at ACA resolution with sensitivity ∼0.4 mJy beam^{-1}. The symbols and contour levels are the same as in Figure 1. (b) The C^{18}O spectra are extracted from high-resolution maps, and V_{sys} = 6 km s^{-1}. All symbols are the same as in Figure 3. (c) Integrated CO emission with sensitivity 2.21 K km s^{-1}, with similar symbols and contours to those in Figure 4(a). (d) CO PV diagram with sensitivity 0.13 K, with similar symbols and contours to those in Figure 4(b).

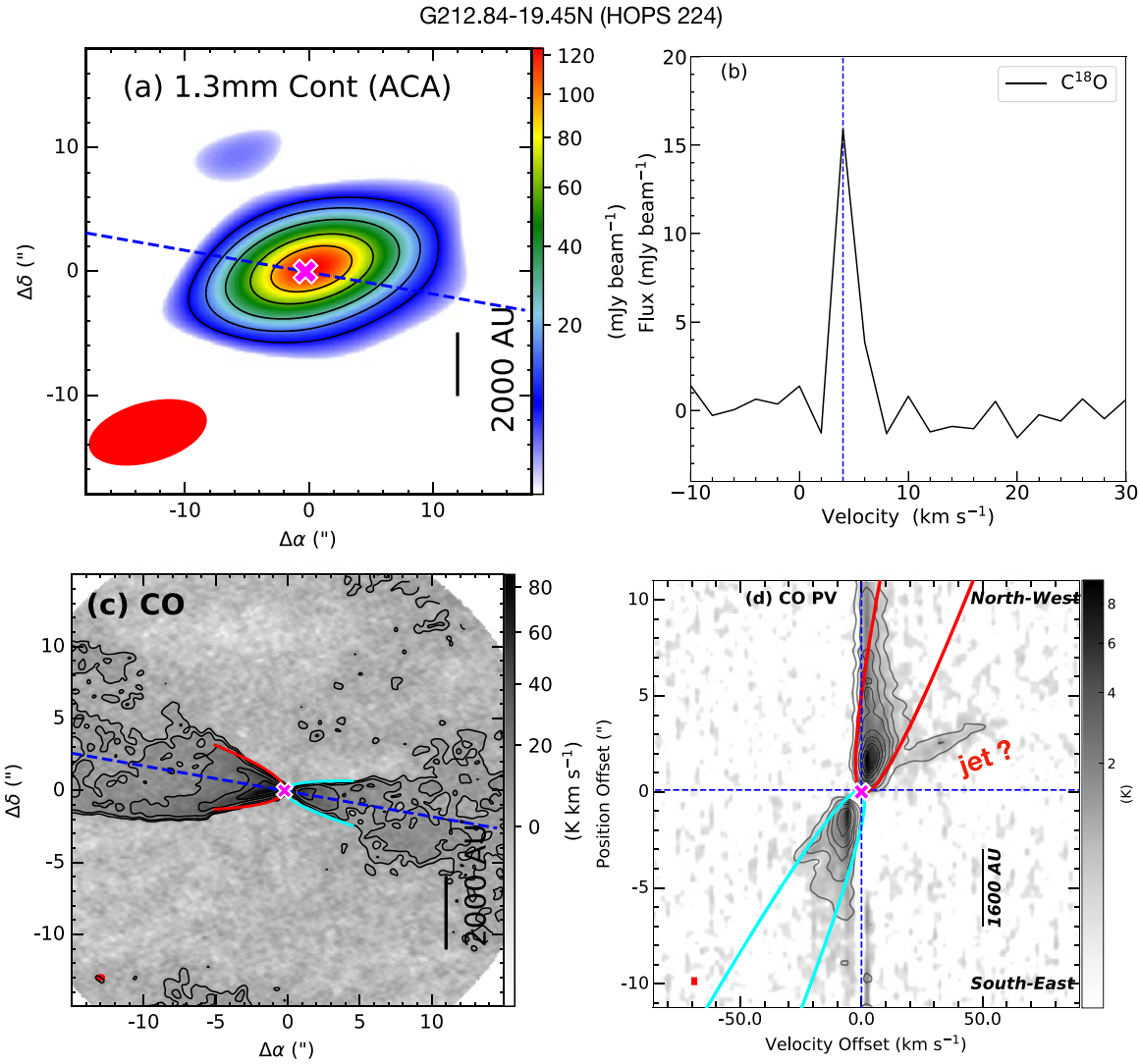

Figure D7. G212.84-19.45N. (a) 1.3 mm continuum map at ACA resolution with sensitivity ∼2.5 mJy beam^{-1}. The symbols and contour levels are the same as in Figure 1. (b) The C^{18}O spectra are extracted from high-resolution maps, and V_{sys} = 4 km s^{-1}. All symbols are the same as in Figure 3. (c) Integrated CO emission with sensitivity 1.24 K km s^{-1}, with similar symbols and contours to those in Figure 4(a). (d) CO PV diagram with sensitivity 0.12 K, with similar symbols and contours to those in Figure 4(b). The "?" mark indicates that the present observations could not confirm the scenario.

Appendix E
Objects with No SiO Emission and No Well-defined CO Outflow

In some identified sources, CO outflows were detected; however, due to poor signal-to-noise ratio, deriving the PV diagram along the outflow axis was not possible (Figures E1–E13). These sources include G201.52-11.08 (a Class I source; Figure E2), G205.46-14.56S2 (a class source HOPS 385; Figure E4), G210.82-19.47S (a class source HOPS 156, Figure E7; outflow driven by G210.82-19.47S, not by secondary source G210.82-19.47S_02), G211.16-19.33N2 (a transition Class 0 to Class I source HOPS 133; Figure E9), G211.47-19.27N (a Class 0 close binary source HOPS 290; Figure E10), and G212.10-19.15S (a class 0 source; HOPS 247; Figure E12).

CO emission is observed in the field of a few other sources; however, in these cases the flow direction cannot be resolved owing to poor sensitivity. These sources are G192.32-11.88S (a Class I source; Figure E1; and source ♯02 is the same as that of G192.32-11.88N), G205.46-14.56N1 (a Class 0 protostar HOPS 402; Figure E3), G206.93-16.61E2 (a Class I multiple system HOPS 298; Figure E5), G207.36-19.82N1 (a binary system, outflow driven by source "A"; Figure E6), G210.97-19.33S2 (a wide binary system source "A" or HOPS 377 and "B" or HOPS 144; Figure E8), G212.10-19.15N2 (a close binary system source "A" or HOPS 263 and "B" or HOPS 262; Figure E11), and G215.87-17.62N (a Class II system; Figure E13).

High-sensitivity observations with other molecular transitions and higher transitions of CO and SiO could be beneficial for studying the outflow/jet morphology of these objects. For instance, G208.68-19.20N1 (HOPS 87) exhibits a compact outflow in HCN (4–3) and CO (3–2), reported in Takahashi & Ho (2012).

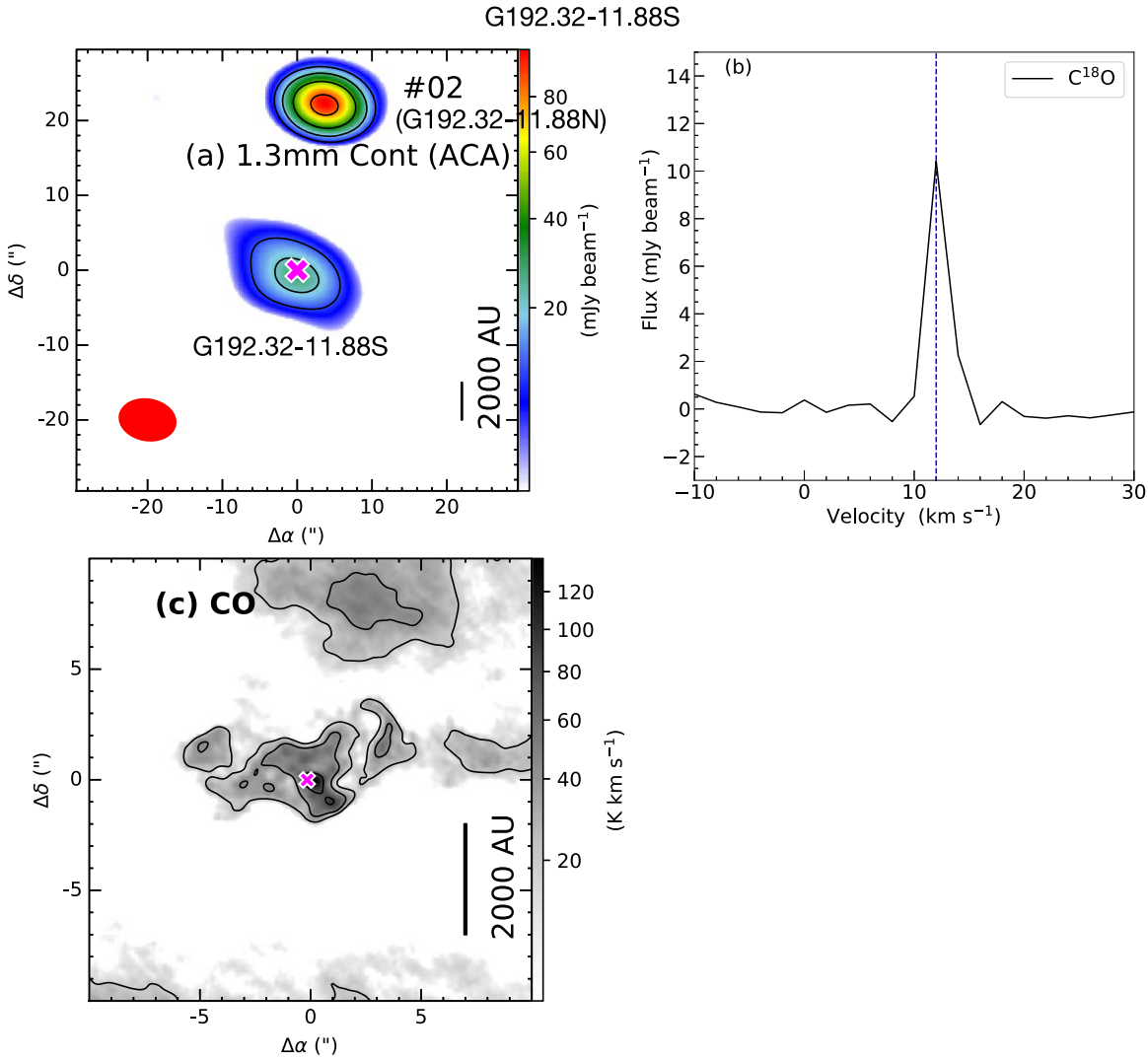

Figure E1. G192.32-11.88S. (a) 1.3 mm continuum map at ACA resolution with sensitivity ∼3.5 mJy beam^{-1}. The symbols and contour levels are the same as in Figure 1. (b) The C^{18}O spectra are extracted from high-resolution maps, and $V_{sys} = 10$ km s^{-1}. All symbols are the same as in Figure 3. (c) Integrated CO emission with sensitivity 6.6 K km s^{-1}, with similar symbols and contours to those in Figure 4(a).

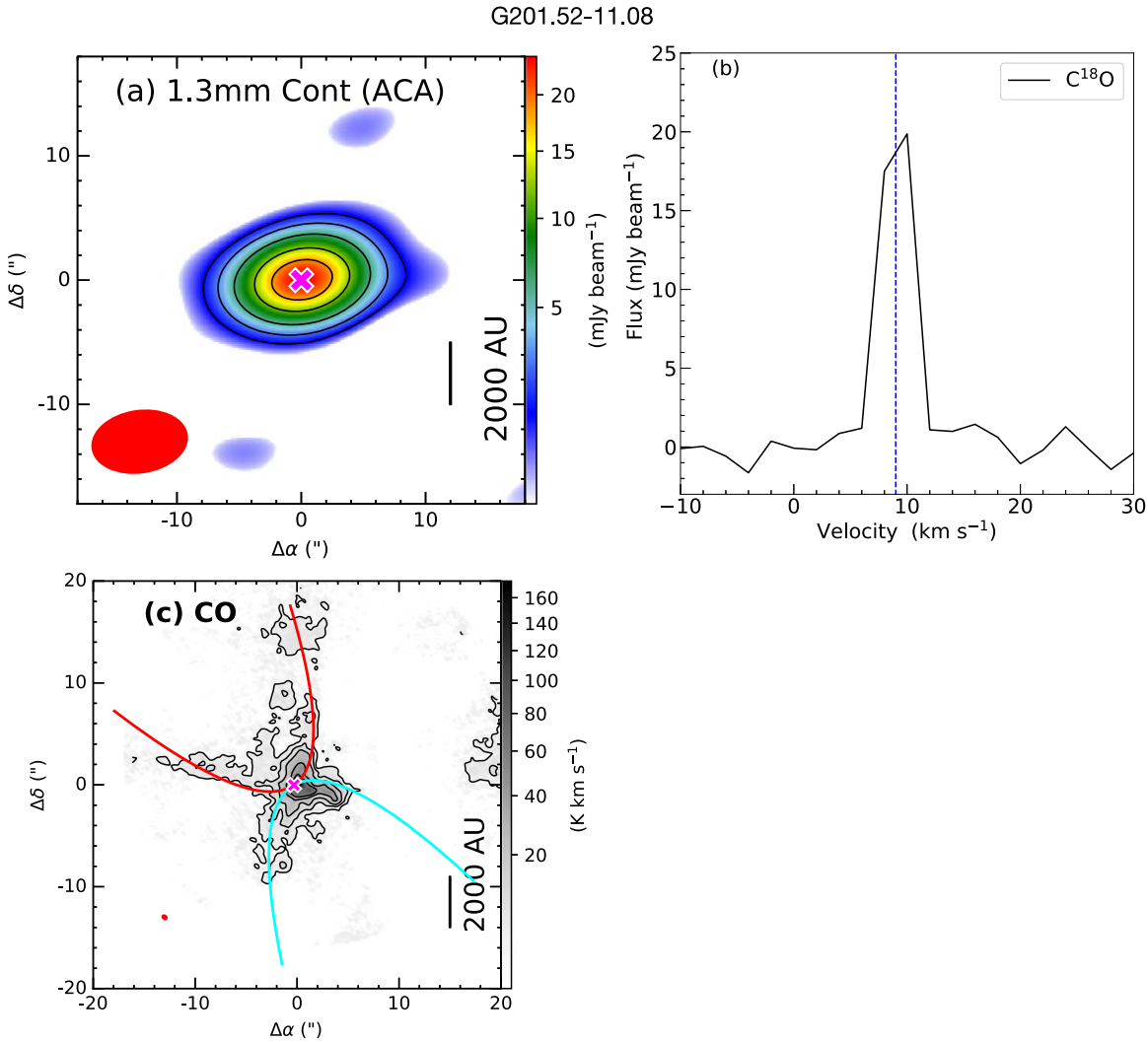

Figure E2. G201.52-11.08. (a) 1.3 mm continuum map at ACA resolution with sensitivity ∼0.5 mJy beam^{-1}. The symbols and contour levels are the same as in Figure 1. (b) The C^{18}O spectra are extracted from high-resolution maps, and $V_{sys} = 9$ km s^{-1}. All symbols are the same as in Figure 3. (c) Integrated CO emission with sensitivity 1.4 K km s^{-1}, with similar symbols and contours to those in Figure 4(a).

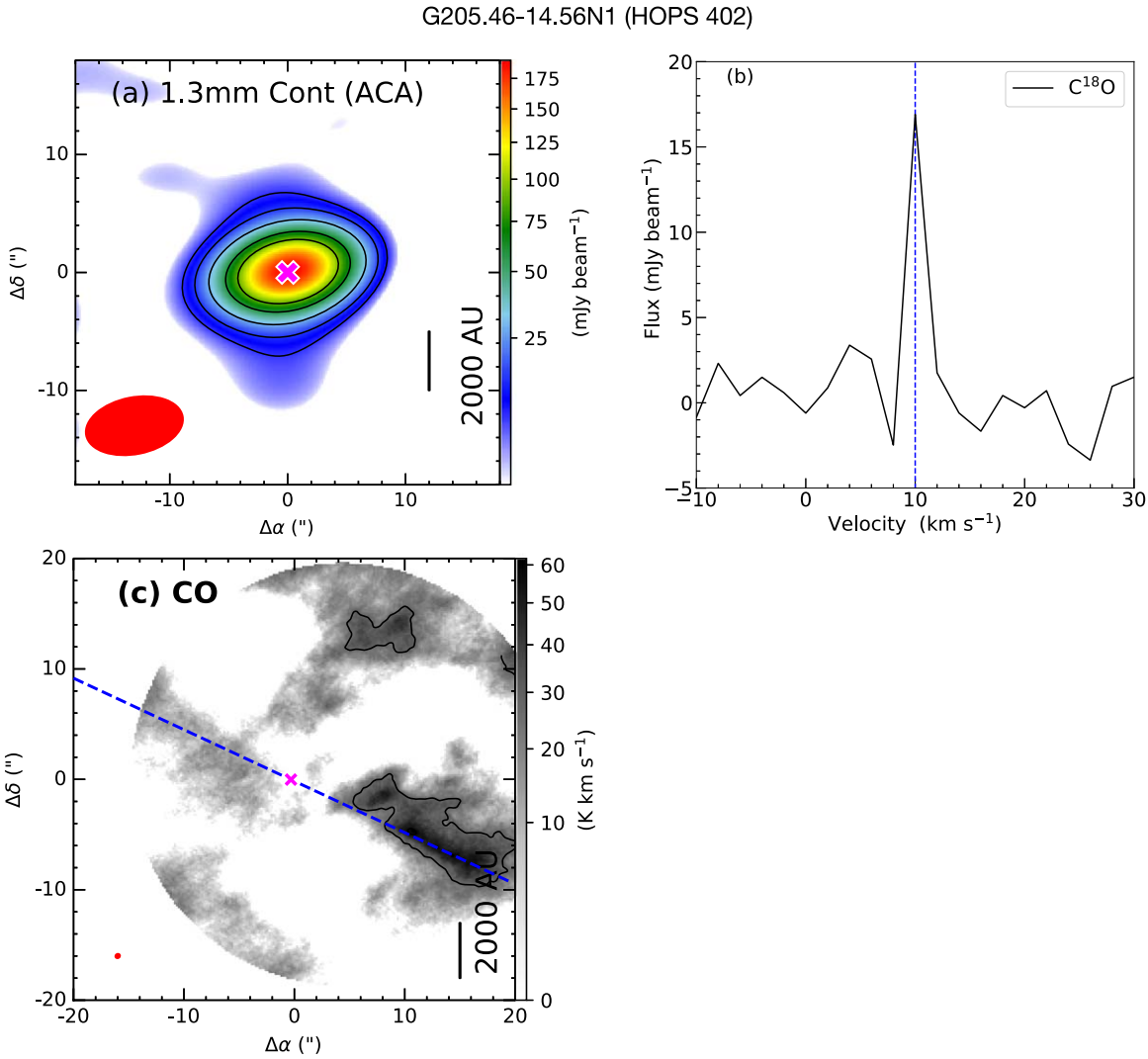

Figure E3. G205.46-14.56N1. (a) 1.3 mm continuum map at ACA resolution with sensitivity ∼2.5 mJy beam^{-1}. The symbols and contour levels are the same as in Figure 1. (b) The C^{18}O spectra are extracted from high-resolution maps, and $V_{sys} = 10$ km s^{-1}. All symbols are the same as in Figure 3. (c) Integrated CO emission with sensitivity 9.2 K km s^{-1}, with similar symbols and contours to those in Figure 4(a).

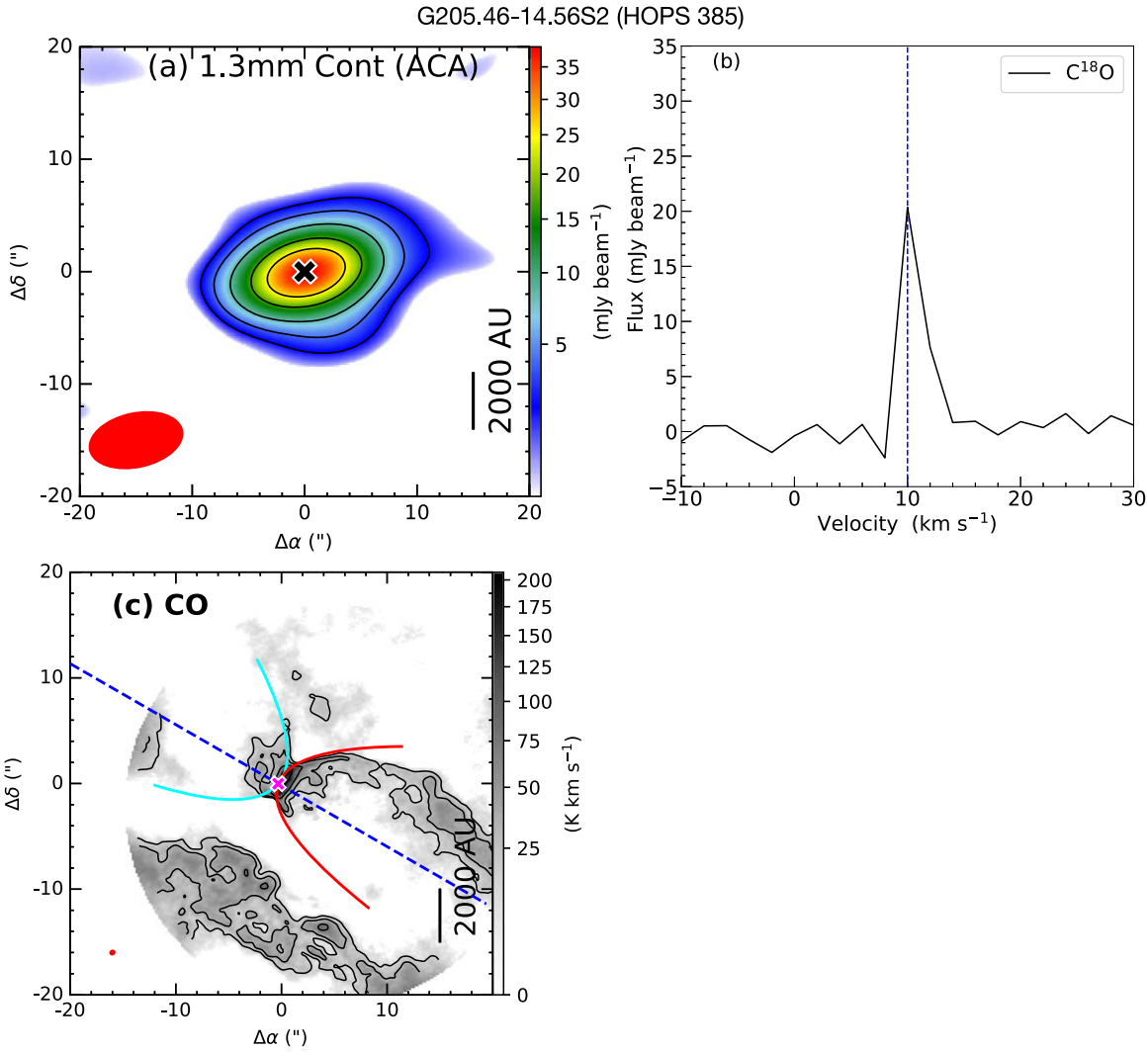

Figure E4. G205.46-14.56S2. (a) 1.3 mm continuum map at ACA resolution with sensitivity ∼0.7 mJy beam^{-1}. The symbols and contour levels are the same as in Figure 1. (b) The $C^{18}O$ spectra are extracted from high-resolution maps, and $V_{sys} = 10$ km s^{-1}. All symbols are the same as in Figure 3. (c) Integrated CO emission with sensitivity 6.0 K km s^{-1}, with similar symbols and contours to those in Figure 4(a).

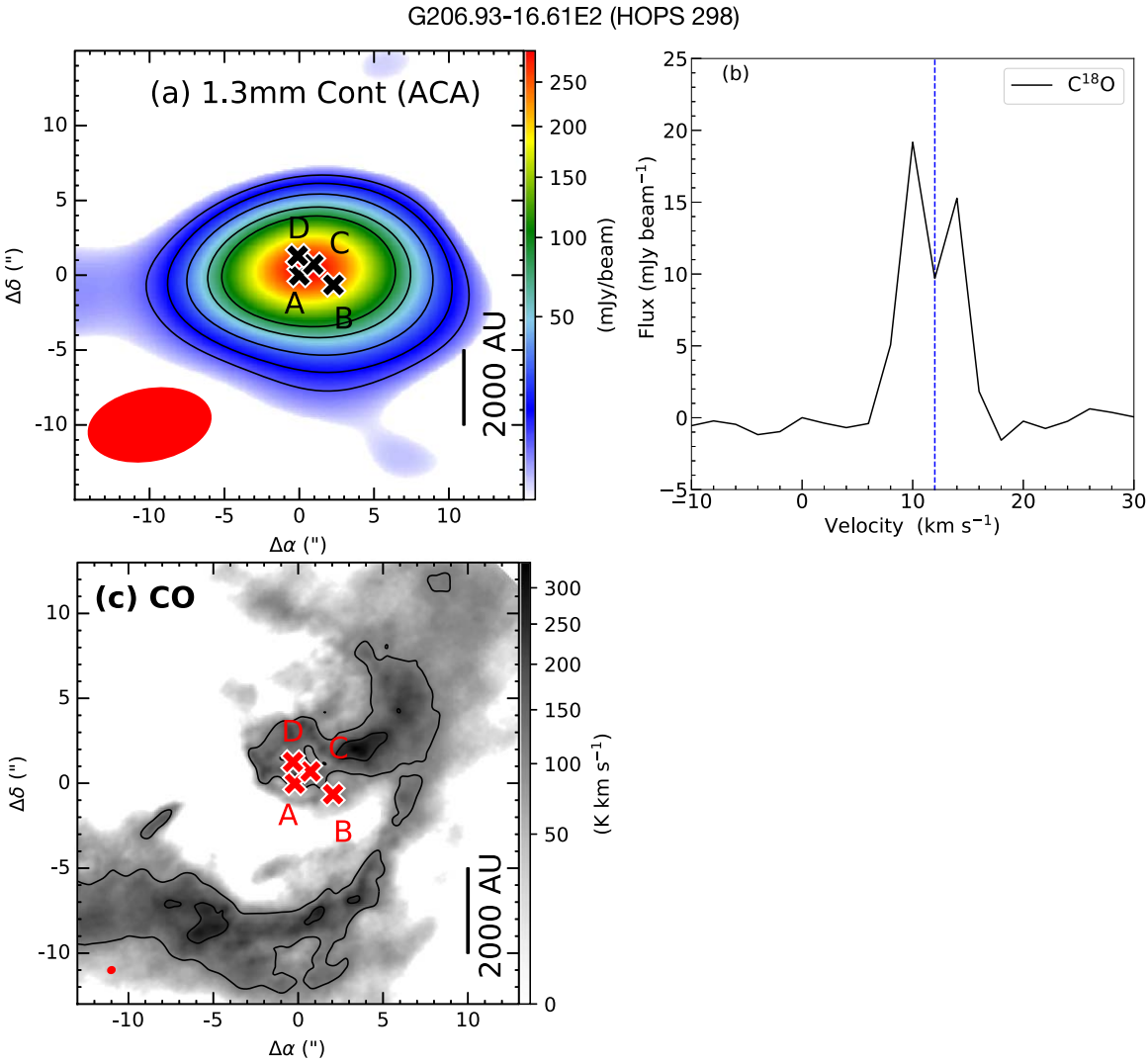

Figure E5. G206.93-16.61E2. (a) 1.3 mm continuum map at ACA resolution with sensitivity ∼2.5 mJy beam^{-1}. The symbols and contour levels are the same as in Figure 1. (b) The $C^{18}O$ spectra are extracted from high-resolution maps, and $V_{sys} = 12$ km s^{-1}. All symbols are the same as in Figure 3. (c) Integrated CO emission with sensitivity 37.5 K km s^{-1}, with similar symbols and contours to those in Figure 4(a).

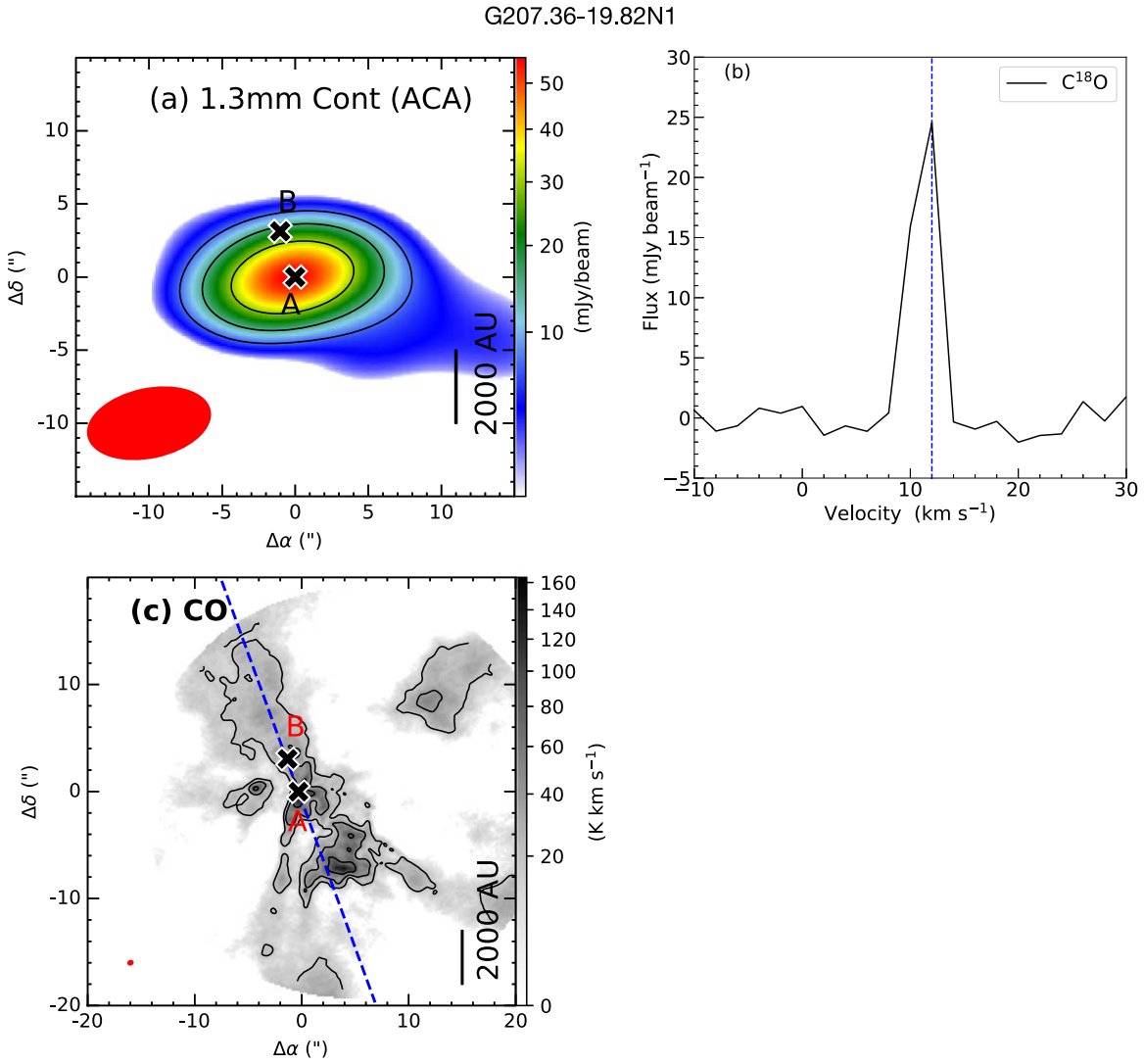

Figure E6. G207.36-19.82N1. (a) 1.3 mm continuum map at ACA resolution with sensitivity ∼2.5 mJy beam^{-1}. The symbols and contour levels are the same as in Figure 1. (b) The $C^{18}O$ spectra are extracted from high-resolution maps, and $V_{sys} = 12$ km s^{-1}. All symbols are the same as in Figure 3. (c) Integrated CO emission with sensitivity 6.13 K km s^{-1}, with similar symbols and contours to those in Figure 4(a).

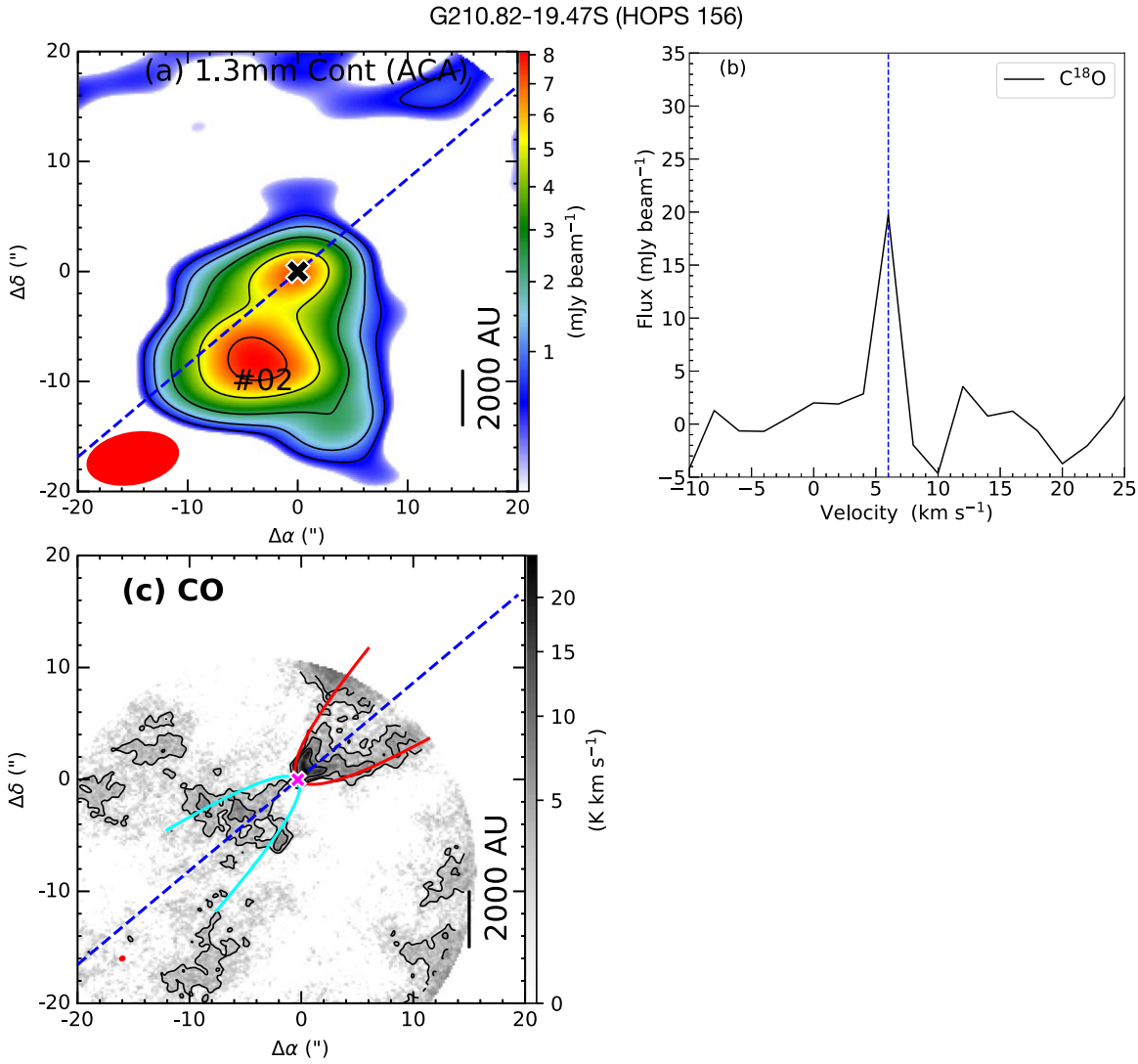

Figure E7. G210.82-19.47S. (a) 1.3 mm continuum map at ACA resolution with sensitivity ∼0.2 mJy beam^{-1}. The symbols and contour levels are the same as in Figure 1. (b) The C^{18}O spectra are extracted from high-resolution maps, and V_{sys} = 6 km s^{-1}. All symbols are the same as in Figure 3. (c) Integrated CO emission with sensitivity 0.8 K km s^{-1}, with similar symbols to those in Figure 4(a).

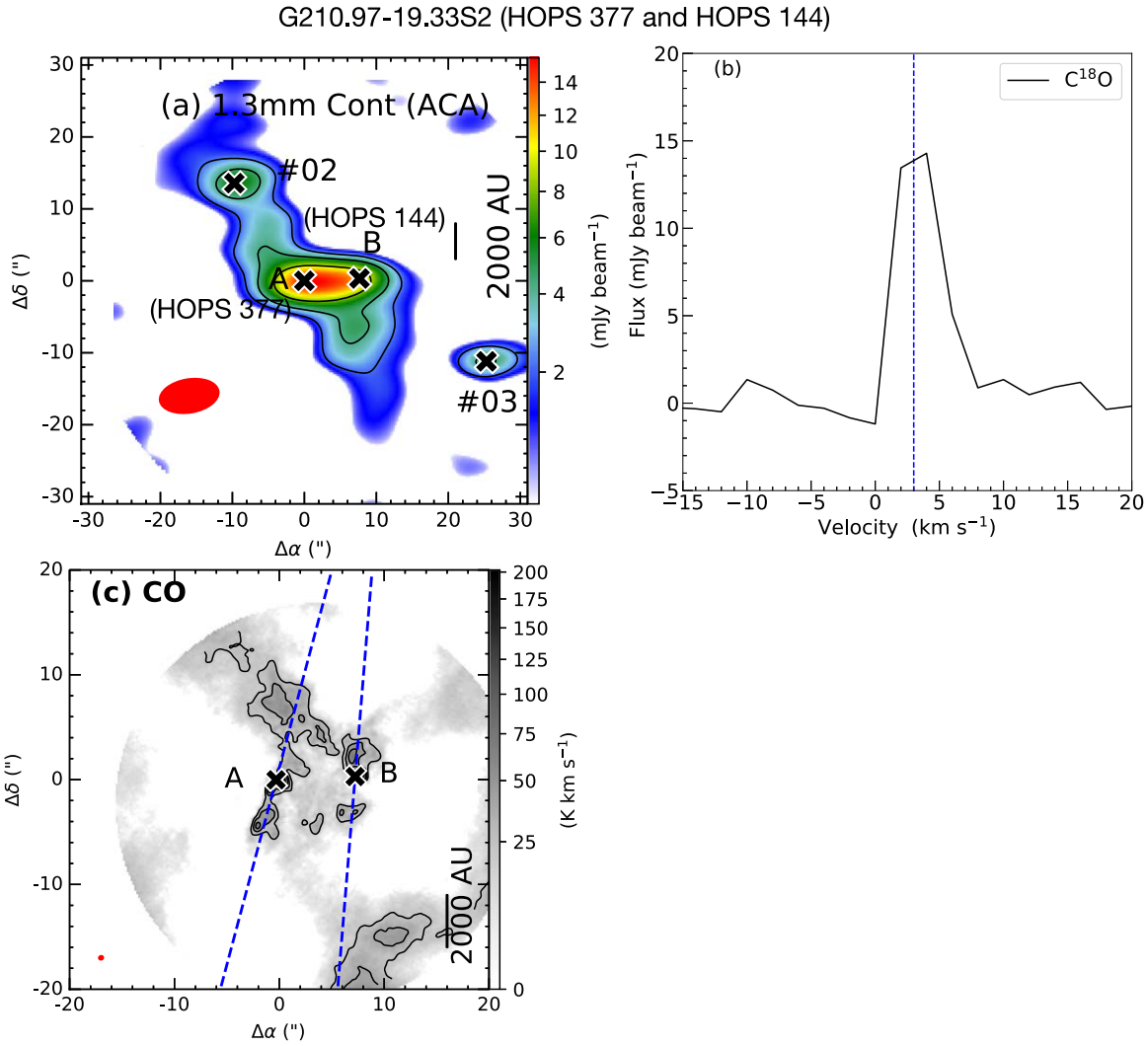

Figure E8. G210.97-19.33S2. (a) 1.3 mm continuum map at ACA resolution with sensitivity ∼0.7 mJy beam^{-1}. The symbols and contour levels are the same as in Figure 1. (b) The C^{18}O spectra are extracted from high-resolution maps, and $V_{sys} = 3.0$ km s^{-1}. All symbols are the same as in Figure 3. (c) Integrated CO emission with sensitivity 8.0 K km s^{-1}, with similar symbols to those in Figure 4(a).

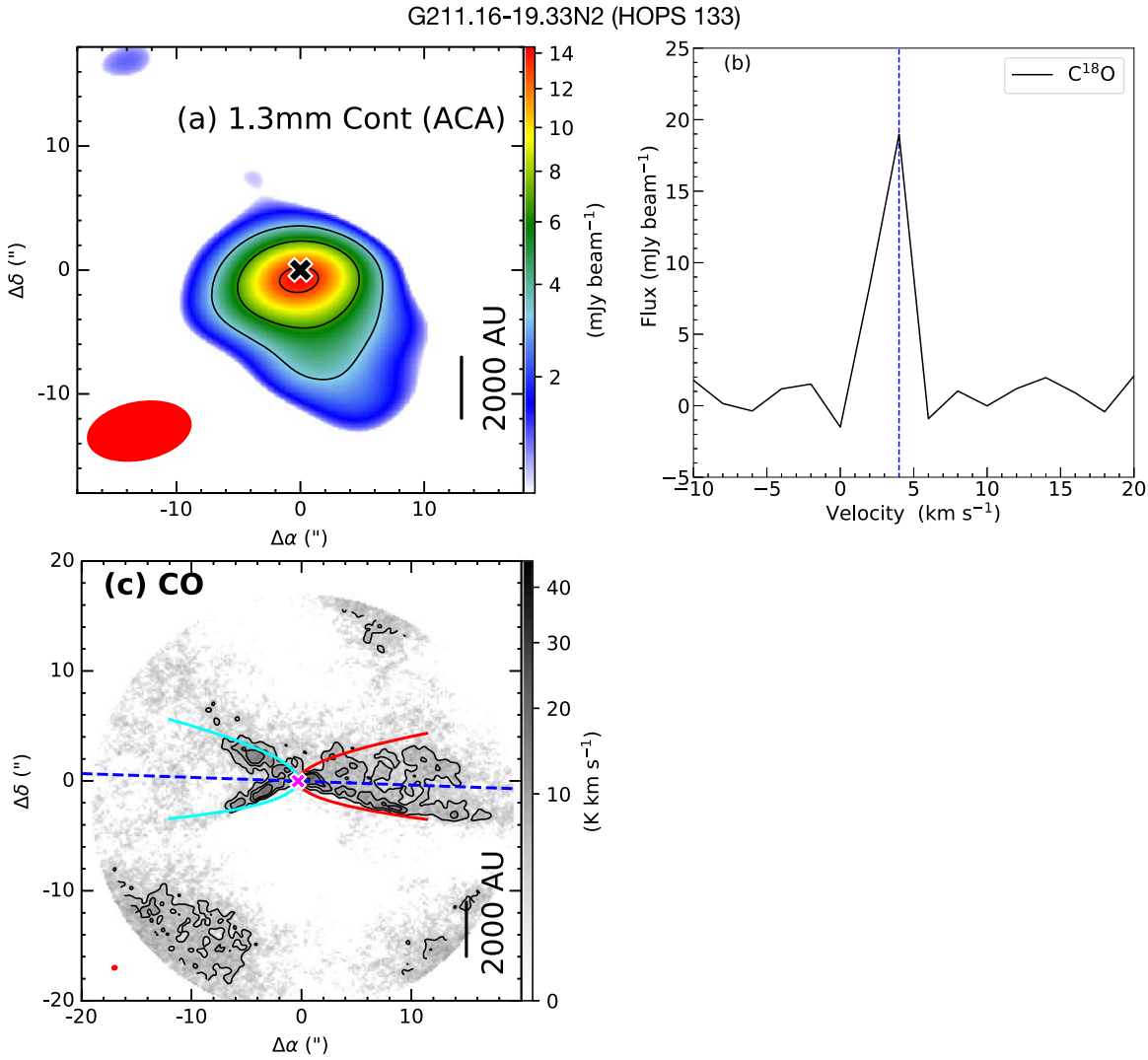

Figure E9. G211.16-19.33N2. (a) 1.3 mm continuum map at ACA resolution with sensitivity ∼1.1 mJy beam^{-1}. The symbols and contour levels are the same as in Figure 1. (b) The C^{18}O spectra are extracted from high-resolution maps, and $V_{sys} = 4.0$ km s^{-1}. All symbols are the same as in Figure 3. (c) Integrated CO emission with sensitivity 1.6 K km s^{-1}, with similar symbols to those in Figure 4(a).

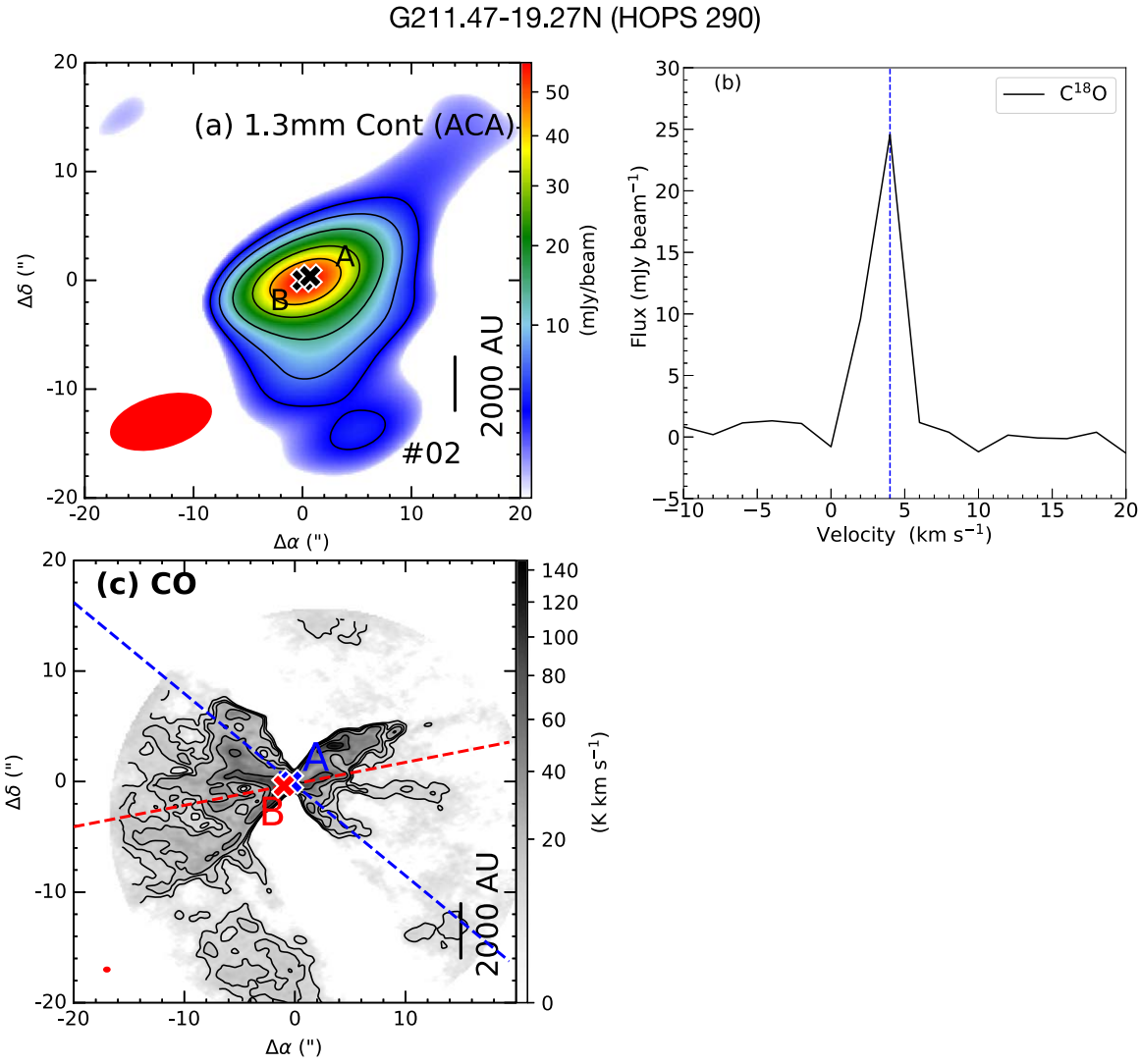

Figure E10. G211.47-19.27N. (a) 1.3 mm continuum map at ACA resolution with sensitivity ∼1.15 mJy beam^{-1}. The symbols and contour levels are the same as in Figure 1. (b) The C^{18}O spectra are extracted from high-resolution maps, and $V_{sys} = 4.0$ km s^{-1}. All symbols are the same as in Figure 3. (c) Integrated CO emission with sensitivity 2.5 K km s^{-1}, with similar symbols to those in Figure 4(a).

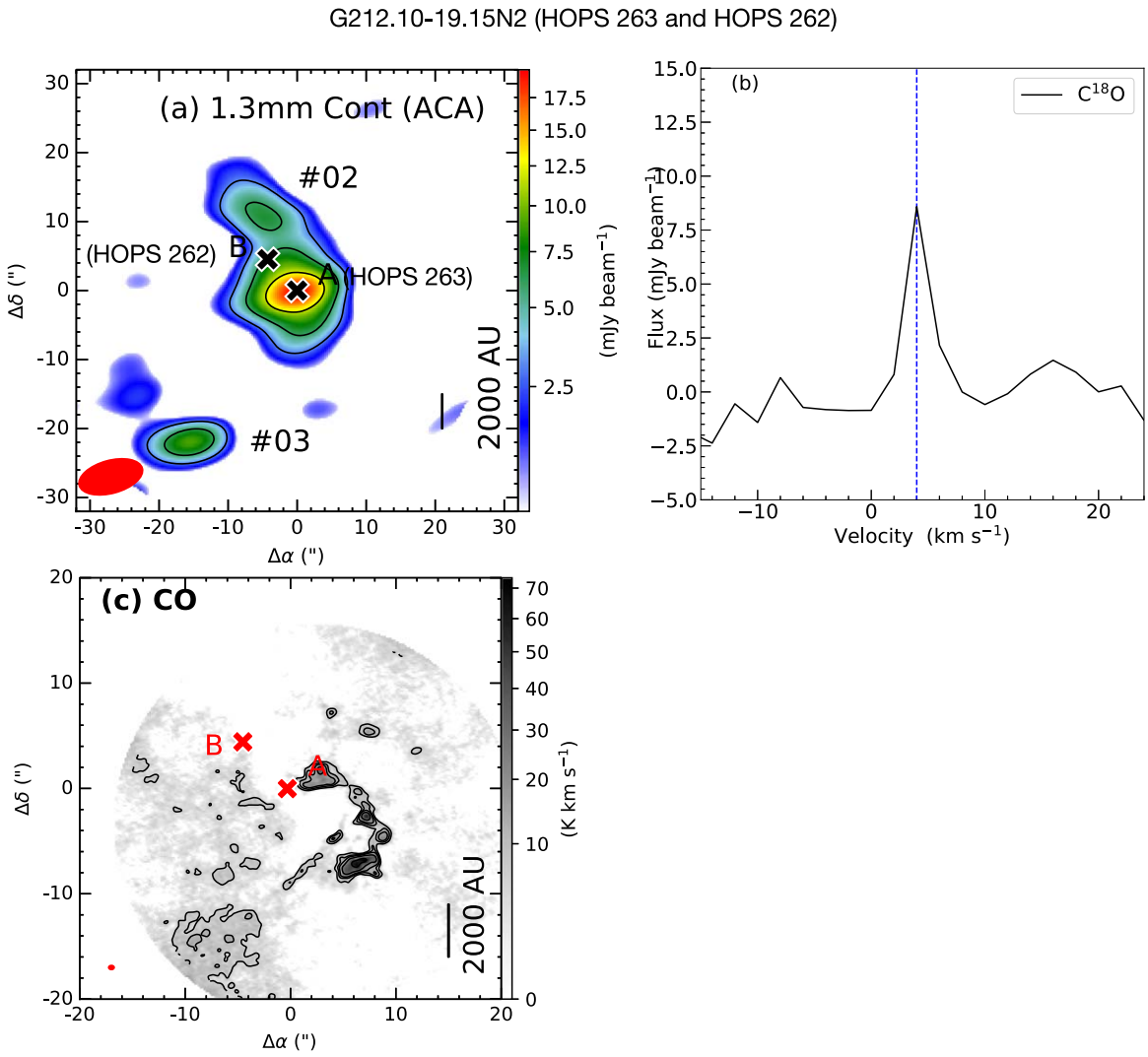

Figure E11. G212.10-19.15N2. (a) 1.3 mm continuum map at ACA resolution with sensitivity ∼1.0 mJy beam^{-1}. The symbols and contour levels are the same as in Figure 1. (b) The C^{18}O spectra are extracted from high-resolution maps, and $V_{sys} = 4.0$ km s^{-1}. All symbols are the same as in Figure 3. (c) Integrated CO emission with sensitivity 2.14 K km s^{-1}, with similar symbols to those in Figure 4(a).

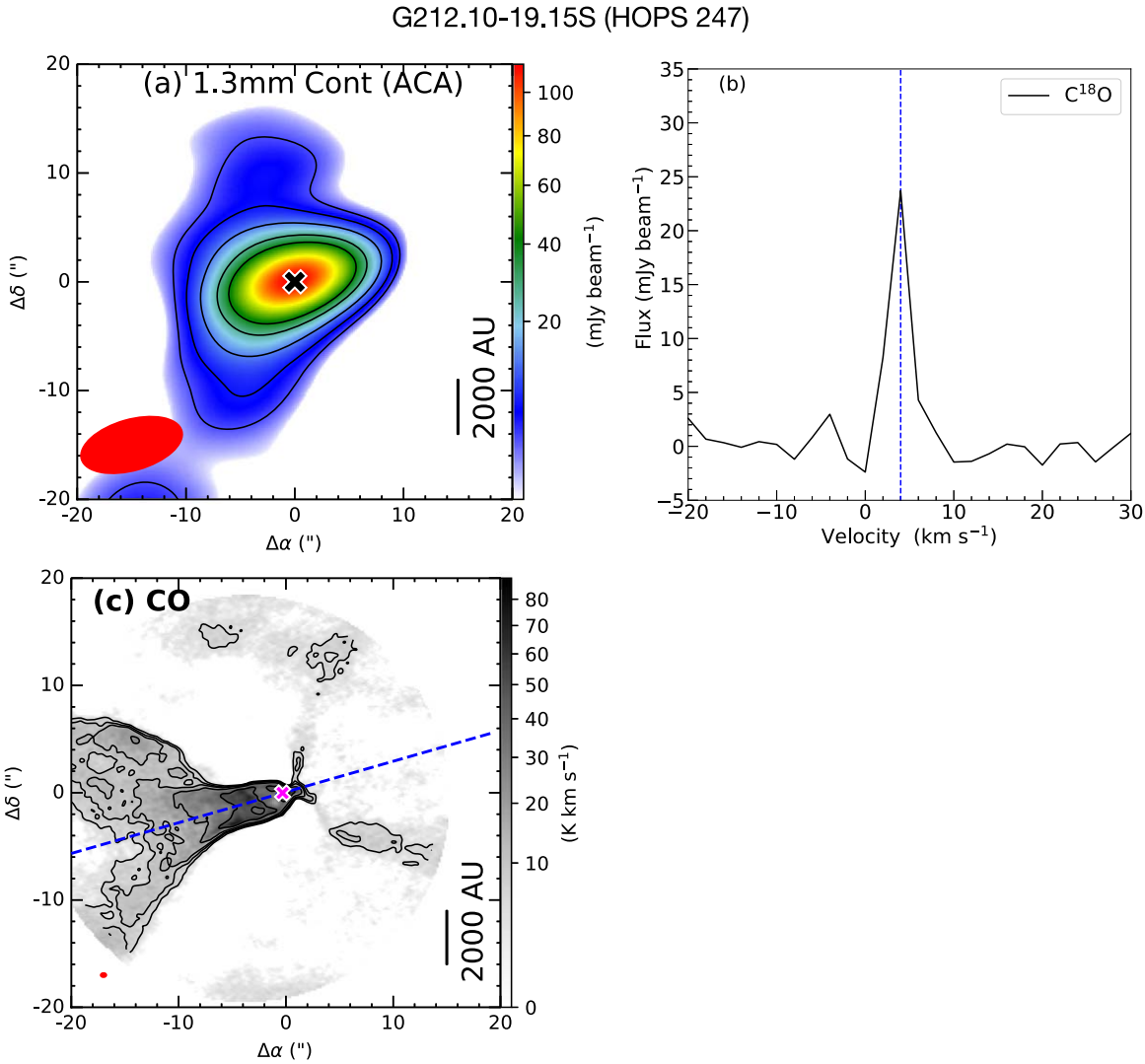

Figure E12. G212.10-19.15S. (a) 1.3 mm continuum map at ACA resolution with sensitivity ∼1.1 mJy beam^{-1}. The symbols and contour levels are the same as in Figure 1. (b) The C^{18}O spectra are extracted from high-resolution maps, and $V_{sys} = 4.0$ km s^{-1}. All symbols are the same as in Figure 3. (c) Integrated CO emission with sensitivity 1.85 K km s^{-1}, with similar symbols to those in Figure 4(a).

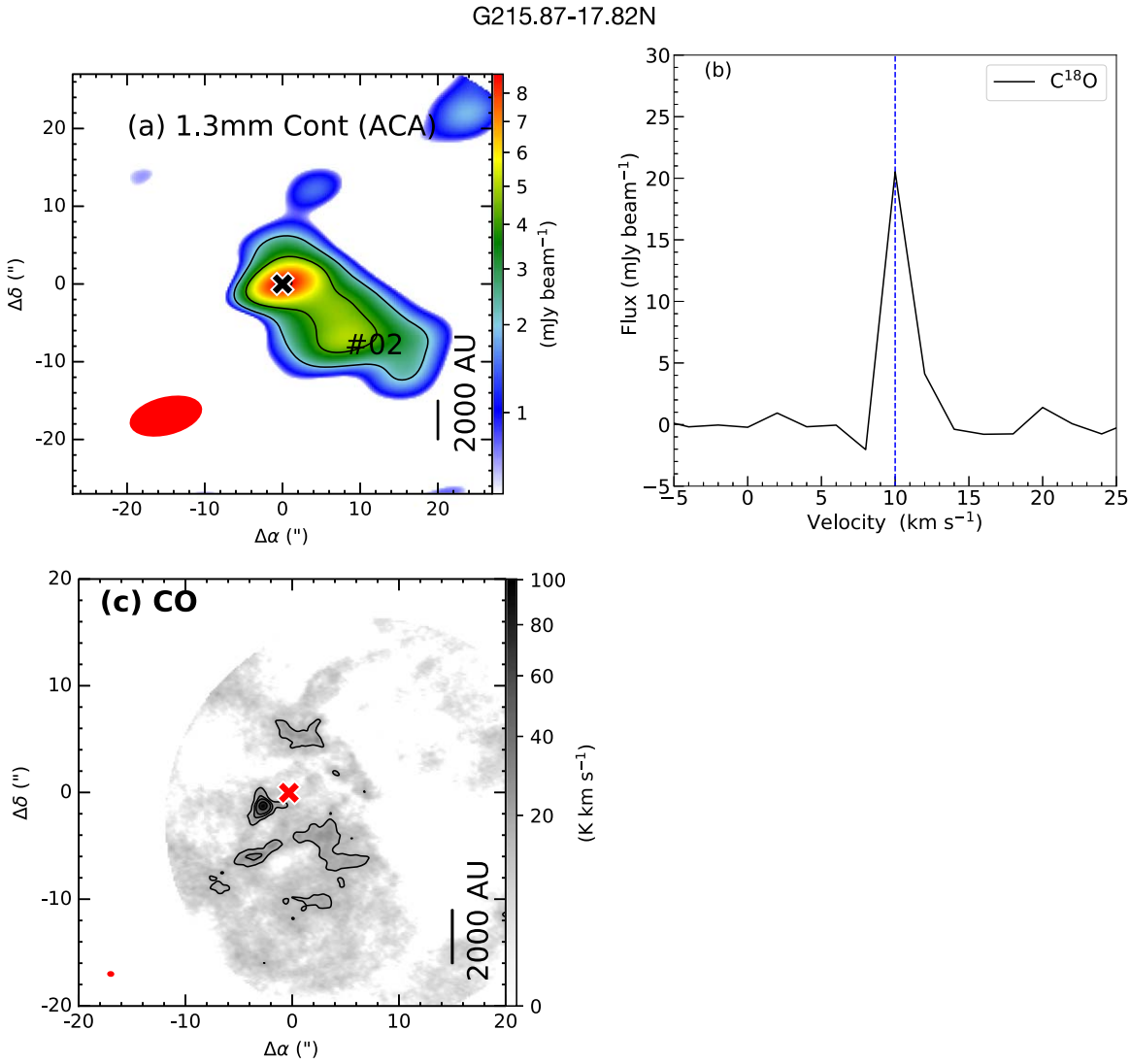

Figure E13. G215.87-17.62N. (a) 1.3 mm continuum map at ACA resolution with sensitivity ∼0.7 mJy beam^{-1}. The symbols and contour levels are the same as in Figure 1. (b) The C^{18}O spectra are extracted from high-resolution maps, and V_{sys} = 10.0 km s^{-1}. All symbols are the same as in Figure 3. (c) Integrated CO emission with sensitivity 5.21 K km s^{-1}, with similar symbols to those in Figure 4(a).

ORCID iDs

Somnath Dutta https://orcid.org/0000-0002-2338-4583
Chin-Fei Lee https://orcid.org/0000-0002-3024-5864
Doug Johnstone https://orcid.org/0000-0002-6773-459X
Jeong-Eun Lee https://orcid.org/0000-0003-3119-2087
Naomi Hirano https://orcid.org/0000-0001-9304-7884
James Di Francesco https://orcid.org/0000-0002-9289-2450
Tie Liu https://orcid.org/0000-0002-5286-2564
Dipen Sahu https://orcid.org/0000-0002-4393-3463
Sheng-Yuan Liu https://orcid.org/0000-0003-4603-7119
Ken'ichi Tatematsu https://orcid.org/0000-0002-8149-8546
Paul F. Goldsmith https://orcid.org/0000-0002-6622-8396
Chang Won Lee https://orcid.org/0000-0002-3179-6334
Shanghuo Li https://orcid.org/0000-0003-1275-5251
David Eden https://orcid.org/0000-0002-5881-3229
Mika Juvela https://orcid.org/0000-0002-5809-4834
Leonardo Bronfman https://orcid.org/0000-0002-9574-8454
Shih-Ying Hsu https://orcid.org/0000-0002-1369-1563
Kee-Tae Kim https://orcid.org/0000-0003-2412-7092
Woojin Kwon https://orcid.org/0000-0003-4022-4132
Patricio Sanhueza https://orcid.org/0000-0002-7125-7685
Xunchuan Liu https://orcid.org/0000-0001-8315-4248
Jesús Alejandro López-Vázquez https://orcid.org/0000-0002-5845-8722
Qiuyi Luo https://orcid.org/0000-0003-4506-3171
Hee-Weon Yi https://orcid.org/0000-0003-0537-5461

References

Arce, H. G., Shepherd, D., Gueth, F., et al. 2007, in Protostars and Planets, ed. B. Reipurth, D. Jewitt, & K. Keil (Tucson, AZ: Univ. Arizona Press), 245
Astropy collaboration, Robitaille, T. P., Tollerud, E. J., et al. 2013, A&A, 558, A33
Audard, M., Ábrahám, P., Dunham, M. M., et al. 2014, in Protostars and Planets VI, ed. H. Beuther et al. (Tucson, AZ: Univ. Arizona Press), 387
Bachiller, R., Gueth, F., Guilloteau, S., Tafalla, M., & Dutrey, A. 2000, A&A, 362, L33
Balança, C., Dayou, F., Faure, A., Wiesenfeld, L., & Feautrier, N. 2018, MNRAS, 479, 2692
Bisschop, S. E., Jørgensen, J. K., van Dishoeck, E. F., & de Wachter, E. B. M. 2007, A&A, 465, 913
Bjerkeli, P., Ramsey, J. P., Harsono, D., et al. 2019, A&A, 631, A64

Blondin, J. M., Fryxell, B. A., & Konigl, A. 1990, ApJ, 360, 370
Bontemps, S., Andre, P., Terebey, S., & Cabrit, S. 1996, A&A, 311, 858
Cabrit, S., & Bertout, C. 1992, A&A, 261, 274
Charnley, S. B., Rodgers, S. D., & Ehrenfreund, P. 2001, A&A, 378, 1024
Cieza, L. A., Casassus, S., Tobin, J., et al. 2016, Natur, 535, 258
Codella, C., Maury, A. J., Gueth, F., et al. 2014, A&A, 563, L3
Draine, B. T. 2006, ApJ, 636, 1114
Draine, B. T., & Salpeter, E. E. 1979, ApJ, 231, 77
Dunham, M. M., Arce, H. G., Mardones, D., et al. 2014a, ApJ, 783, 29
Dunham, M. M., Stutz, A. M., Allen, L. E., et al. 2014b, in Protostars and Planets VI, ed. H. Beuther et al. (Tucson, AZ: Univ. Arizona Press), 195
Dutta, S., Lee, C.-F., Hirano, N., et al. 2022a, ApJ, 931, 130
Dutta, S., Lee, C.-F., Johnstone, D., et al. 2022b, ApJ, 925, 11
Dutta, S., Lee, C.-F., Liu, T., et al. 2020, ApJS, 251, 20
Ellerbroek, L. E., Podio, L., Kaper, L., et al. 2013, A&A, 551, A5
Fischer, W. J., Hillenbrand, L. A., Herczeg, G. J., et al. 2023, in ASP Conf. Ser. 534, Protostars and Planets VII, ed. S. Inutsuka et al. (San Francisco, CA: ASP), 355
Frank, A., Ray, T. P., Cabrit, S., et al. 2014, in Protostars and Planets VI, ed. H. Beuther et al. (Tucson, AZ: Univ. Arizona Press), 451
Furlan, E., Fischer, W. J., Ali, B., et al. 2016, ApJS, 224, 5
Glassgold, A. E., Mamon, G. A., & Huggins, P. J. 1991, ApJ, 373, 254
Harsono, D., Bjerkeli, P., van der Wiel, M. H. D., et al. 2018, NatAs, 2, 646
Herczeg, G. J., Johnstone, D., Mairs, S., et al. 2017, ApJ, 849, 43
Hirano, N., Ho, P. P. T., Liu, S.-Y., et al. 2010, ApJ, 717, 58
Hirano, S., & Machida, M. N. 2019, MNRAS, 485, 4667
Hsieh, T.-H., Lai, S.-P., Belloche, A., & Wyrowski, F. 2016, ApJ, 826, 68
Hsieh, T.-H., Murillo, N. M., Belloche, A., et al. 2019, ApJ, 884, 149
Hsu, S.-Y., Liu, S.-Y., & Liu, T. 2022, ApJ, 927, 218
Hsu, S.-Y., Liu, S.-Y., Liu, T., et al. 2020, ApJ, 898, 107
Hu, C.-Y., Zhukovska, S., Somerville, R. S., & Naab, T. 2019, MNRAS, 487, 3252
Hunter, J. D. 2007, CSE, 9, 90
Imai, M., Oya, Y., Sakai, N., et al. 2019, ApJL, 873, L21
Jhan, K.-S., & Lee, C.-F. 2016, ApJ, 816, 32
Jhan, K.-S., & Lee, C.-F. 2021, ApJ, 909, 11
Jhan, K.-S., Lee, C.-F., Johnstone, D., et al. 2022, ApJL, 931, L5
Jørgensen, J. K., Kuruwita, R. L., Harsono, D., et al. 2022, Natur, 606, 272
Jørgensen, J. K., Visser, R., Williams, J. P., & Bergin, E. A. 2015, A&A, 579, A23
Karnath, N., Megeath, S. T., Tobin, J. J., et al. 2020, ApJ, 890, 129
Kim, G., Lee, C. W., Maheswar, G., et al. 2019, ApJS, 240, 18
Krumholz, M. R., Bate, M. R., Arce, H. G., et al. 2014, in Protostars and Planets VI, ed. H. Beuther et al. (Tucson, AZ: Univ. Arizona Press), 243
Larson, R. B. 1969, MNRAS, 145, 271
Lee, C.-F. 2020, A&ARv, 28, 1
Lee, C.-F., Hasegawa, T. I., Hirano, N., et al. 2010, ApJ, 713, 731
Lee, C.-F., Ho, P. T. P., Beuther, H., et al. 2006, ApJ, 639, 292
Lee, C.-F., Ho, P. T. P., Hirano, N., et al. 2007a, ApJ, 659, 499
Lee, C.-F., Ho, P. T. P., Li, Z.-Y., et al. 2017a, NatAs, 1, 0152
Lee, C.-F., Ho, P. T. P., Palau, A., et al. 2007b, ApJ, 670, 1188
Lee, C.-F., Kwon, W., Jhan, K.-S., et al. 2019a, ApJ, 879, 101
Lee, C.-F., Li, Z.-Y., Hirano, N., et al. 2018, ApJ, 863, 94
Lee, C.-F., Li, Z.-Y., Ho, P. T. P., et al. 2017b, SciA, 3, e1602935
Lee, C.-F., Li, Z.-Y., Shang, H., & Hirano, N. 2022, ApJL, 927, L27
Lee, C.-F., Mundy, L. G., Reipurth, B., Ostriker, E. C., & Stone, J. M. 2000, ApJ, 542, 925
Lee, C.-F., Rao, R., Ching, T.-C., et al. 2014, ApJL, 797, L9
Lee, C.-F., Stone, J. M., Ostriker, E. C., & Mundy, L. G. 2001, ApJ, 557, 429
Lee, C. W., Kim, M.-R., Kim, G., et al. 2013, ApJ, 777, 50
Lee, J.-E., Lee, S., Baek, G., et al. 2019b, NatAs, 3, 314
Lee, Y.-H., Johnstone, D., Lee, J.-E., et al. 2021, ApJ, 920, 119
Lefèvre, C., Cabrit, S., Maury, A. J., et al. 2017, A&A, 604, L1
Luo, Q.-y., Liu, T., Tatematsu, K., et al. 2022, ApJ, 931, 158
Machida, M. N., & Basu, S. 2019, ApJ, 876, 149
Machida, M. N., & Hosokawa, T. 2013, MNRAS, 431, 1719
McMullin, J. P., Waters, B., Schiebel, D., Young, W., & Golap, K. 2007, in ASP Conf. Ser. 376, CASA Architecture and Applications, ed. R. A. Shaw, F. Hill, & D. J. Bell (San Francisco, CA: ASP), 127
Mercer, A., & Stamatellos, D. 2017, MNRAS, 465, 2
Moraghan, A., Lee, C.-F., Huang, P.-S., & Vaidya, B. 2016, MNRAS, 460, 1829
Nisini, B., Santangelo, G., Giannini, T., et al. 2015, ApJ, 801, 121
Nony, T., Motte, F., Louvet, F., et al. 2020, A&A, 636, A38
Nozawa, T., Kozasa, T., & Habe, A. 2006, ApJ, 648, 435
Offner, S. S. R., Klein, R. I., McKee, C. F., & Krumholz, M. R. 2009, ApJ, 703, 131
Ohashi, N., Tobin, J. J., Jørgensen, J. K., et al. 2023, ApJ, 951, 8
Ossenkopf, V., & Henning, T. 1994, A&A, 291, 943
Palau, A., Zapata, L. A., Rodríguez, L. F., et al. 2014, MNRAS, 444, 833
Panoglou, D., Cabrit, S., Pineau Des Forêts, G., et al. 2012, A&A, 538, A2
Park, W., Lee, J.-E., Contreras Peña, C., et al. 2021, ApJ, 920, 132
Plunkett, A. L., Arce, H. G., Mardones, D., et al. 2015, Natur, 527, 70
Podio, L., Codella, C., Gueth, F., et al. 2015, A&A, 581, A85
Podio, L., Codella, C., Gueth, F., et al. 2016, A&A, 593, L4
Podio, L., Tabone, B., Codella, C., et al. 2021, A&A, 648, A45
Raga, A. C., Velázquez, P. F., Cantó, J., & Masciadri, E. 2002, A&A, 395, 647
Riaz, R., Vanaverbeke, S., & Schleicher, D. R. G. 2018, A&A, 614, A53
Robitaille, T., & Bressert, E., 2012 APLpy: Astronomical Plotting Library in Python, Astrophysics Source Code Library, ascl:1208.017
Rodgers, S. D., & Charnley, S. B. 2003, ApJ, 585, 355
Sahu, D., Liu, S.-Y., Liu, T., et al. 2021, ApJL, 907, L15
Santiago-García, J., Tafalla, M., Johnstone, D., & Bachiller, R. 2009, A&A, 495, 169
Schilke, P., Walmsley, C. M., Pineau des Forets, G., & Flower, D. R. 1997, A&A, 321, 293
Shang, H., Liu, C.-F., Krasnopolsky, R., & Wang, L.-Y. 2023, ApJ, 944, 230
Shu, F. H., Najita, J., Ostriker, E. C., & Shang, H. 1995, ApJL, 455, L155
Simon, M., Dutrey, A., & Guilloteau, S. 2000, ApJ, 545, 1034
Skretas, I. M., & Kristensen, L. E. 2022, A&A, 660, A39
Snell, R. L., Loren, R. B., & Plambeck, R. L. 1980, ApJL, 239, L17
Stahler, S. W. 1988, ApJ, 332, 804
Stamatellos, D., Whitworth, A. P., & Hubber, D. A. 2011, ApJ, 730, 32
Stamatellos, D., Whitworth, A. P., & Hubber, D. A. 2012, MNRAS, 427, 1182
Tabone, B., Godard, B., Pineau des Forêts, G., Cabrit, S., & van Dishoeck, E. F. 2020, A&A, 636, A60
Tafalla, M., Bachiller, R., Lefloch, B., et al. 2015, A&A, 573, L2
Tafalla, M., Su, Y. N., Shang, H., et al. 2017, A&A, 597, A119
Takahashi, S., & Ho, P. T. P. 2012, ApJL, 745, L10
Taquet, V., Wirström, E. S., & Charnley, S. B. 2016, ApJ, 821, 46
Tobin, J. J., Sheehan, P. D., Megeath, S. T., et al. 2020, ApJ, 890, 130
Vorobyov, E. I., Elbakyan, V. G., Plunkett, A. L., et al. 2018, A&A, 613, A18
Wakelam, V., Coutens, A., Gratier, P., Vidal, T. H. G., & Vaytet, N. 2022, A&A, 666, A191
Wiebe, D. S., Molyarova, T. S., Akimkin, V. V., Vorobyov, E. I., & Semenov, D. A. 2019, MNRAS, 485, 1843
Yang, B., Stancil, P. C., Balakrishnan, N., & Forrey, R. C. 2010, ApJ, 718, 1062
Yang, Y.-L., Sakai, N., Zhang, Y., et al. 2021, ApJ, 910, 20
Yen, H.-W., Koch, P. M., Takakuwa, S., et al. 2017, ApJ, 834, 178
Yıldız, U. A., Kristensen, L. E., van Dishoeck, E. F., et al. 2015, A&A, 576, A109
Yvart, W., Cabrit, S., Pineau des Forêts, G., & Ferreira, J. 2016, A&A, 585, A74
Zapata, L. A., Fernández-López, M., Rodríguez, L. F., et al. 2018, AJ, 156, 239
Zhang, Y., Arce, H. G., Mardones, D., et al. 2019, ApJ, 883, 1
Zinnecker, H., McCaughrean, M. J., & Rayner, J. T. 1998, Natur, 394, 862